

Microparticle charging in spatial plasma afterglows

Citation for published version (APA):

van Minderhout, B. (2021). *Microparticle charging in spatial plasma afterglows*. [Phd Thesis 1 (Research TU/e / Graduation TU/e), Applied Physics and Science Education]. Technische Universiteit Eindhoven.

Document status and date:

Published: 03/02/2021

Document Version:

Publisher's PDF, also known as Version of Record (includes final page, issue and volume numbers)

Please check the document version of this publication:

- A submitted manuscript is the version of the article upon submission and before peer-review. There can be important differences between the submitted version and the official published version of record. People interested in the research are advised to contact the author for the final version of the publication, or visit the DOI to the publisher's website.
- The final author version and the galley proof are versions of the publication after peer review.
- The final published version features the final layout of the paper including the volume, issue and page numbers.

[Link to publication](#)

General rights

Copyright and moral rights for the publications made accessible in the public portal are retained by the authors and/or other copyright owners and it is a condition of accessing publications that users recognise and abide by the legal requirements associated with these rights.

- Users may download and print one copy of any publication from the public portal for the purpose of private study or research.
- You may not further distribute the material or use it for any profit-making activity or commercial gain
- You may freely distribute the URL identifying the publication in the public portal.

If the publication is distributed under the terms of Article 25fa of the Dutch Copyright Act, indicated by the "Taverne" license above, please follow below link for the End User Agreement:

www.tue.nl/taverne

Take down policy

If you believe that this document breaches copyright please contact us at:

openaccess@tue.nl

providing details and we will investigate your claim.

Microparticle charging in spatial plasma afterglows

PROEFSCHRIFT

ter verkrijging van de graad van doctor aan de Technische Universiteit Eindhoven,
op gezag van de rector magnificus, prof.dr.ir. F. P. T. Baaijens,
voor een commissie aangewezen door het College voor Promoties,
in het openbaar te verdedigen op woensdag 3 februari 2021 om 13:30

door

Boy van Minderhout

geboren te Roosendaal

Dit proefschrift is goedgekeurd door de promotoren en de samenstelling van de promotiecommissie is als volgt:

voorzitter: prof.dr.ir. E. J. E. Cottaar
promotoren: dr.ir. J. Beckers
 prof.dr.ir. G. M. W. Kroesen
leden: prof.dr. L. S. Matthews (Baylor University)
 prof.dr. A. A. Bol
 prof.dr.rer.nat. H. Kersten (Christian-Alrechts-Universität zu Kiel)
adviseur: ir. A. T. A. Peijnenburg (VDL Enabling Technologies Group)

Het onderzoek dat in dit proefschrift wordt beschreven is uitgevoerd in overeenstemming met de TU/e Gedragscode Wetenschapsbeoefening.

Microparticle charging in spatial plasma afterglows

Boy van Minderhout

Cover design

Kim van Mourik

Cover photos

Bart van Overbeeke Fotografie (front)

Tijn van de Ven (back)

Printed by

Print Service Ede on FSC certified paper

This study received financial support from VDL Enabling Technologies Group.



A catalogue record is available from the Eindhoven University of Technology Library.

ISBN: 978-90-386-5201-6

© Boy van Minderhout, 2021

*J'ai décidé d'être heureux
parce que c'est bon pour la santé.*

Voltaire

Summary

Dust particle contamination is a crucial problem in today's society. This is not only due to the worldwide rise in air pollution which reduces people's life expectancy in industrial areas, but also because dust particles strongly impact the production process of one of the smallest and most complicated elements: electronic chips for computers and smartphones. In both examples, control and mitigation of the contaminating particles are of the utmost importance. This thesis will explore the first and most fundamental steps to open up opportunities for plasma-based particle removal.

A plasma is an ionised gas consisting, apart from atoms or molecules, of electrons and ions. Plasmas can, therefore, charge embedded nano- to micrometre-sized particles electrically. Moreover, high electric fields are self-induced by the plasma at its boundaries. These two properties combined form the very basis for future plasma-assisted contamination control techniques. In order to remove airborne particles out of a gas flow, knowledge is required about the charging mechanisms taking place not only in the active plasma region, but also in the Spatial Plasma Afterglow (SPA) of the discharge. Previous studies have been limited to particle charging in temporal plasma afterglows, which differ significantly concerning the evolution of plasma parameters. To bridge this knowledge gap, this research presents fundamental insights into the plasma-particle charging dynamics in the largely unexplored spatial plasma afterglow.

The presented knowledge is obtained by experiments and by simplified modelling of the local plasma-particle interaction. Experiments were carried out using the designed and developed Plasma Particle Charging Investigation (PPCI) setup. Microparticles were injected in a vacuum environment before being electrically charged by an inductively coupled plasma. The residual charge of these particles and their interaction with the afterglow were subsequently investigated through monitoring their behaviour in an externally applied electric field under varying experimental conditions. The electric field-influenced particle trajectories were studied using laser light scattering and high-speed camera imaging, combined with in-house developed particle tracking software.

For the purposes of this study, the following two research lines were defined.

- Research line one focusses on the charge and (de)charging of spherical microparticles in different types of spatial plasma afterglows by means of analysing the complex interplay of the processes governing the particle charging.
- Research line two experimentally reveals how clustered microparticles in a spatial plasma afterglow region are charged. To date, several competing models have been used in the literature to describe the charge of non-spherical particles, none of which have been either verified or refuted. This research line therefore conveys experimental proof to answer this outstanding question.

In research line one, the particle charge and (de)charging were investigated in three different SPA-types. In the free SPA, void of any physical obstruction between the active plasma region and its SPA, the microparticle charge was accurately measured. The experiments showed a particle charge of $-30 \pm 7 e$, which is three orders of magnitude lower than the typical particle charge of $-10^4 e$ expected in the plasma bulk for the used silver-coated melamine-formaldehyde particles with a diameter of $4.9 \pm 0.2 \mu\text{m}$.

A relatively simple analytical timescale model analysed this difference in particle charge between the bulk and the SPA. From this, it was derived that the difference in the electron temperature between the bulk and the afterglow region mainly explains the difference in the particle charge.

As for the shielded SPA, it was shown that the particle charge can be precisely controlled, ranging from small negative ($-40 e$) to even small positive charges ($+10 e$) by changing the magnitude of the externally applied electric field only. The shielded SPA was created by the application of a mesh grid in the cross-section of the setup, separating the plasma bulk from its afterglow. The presence of the mesh grid induced an additional electric field component between the grid and the electrodes that were used to create an externally applied electric field. This additional electric field, in turn, influenced the positive ion space charge distribution and, thereby, enabled the particle charge control. In the free SPA, however, this additional electric field component was much smaller due to the absence of the mesh grid. Regarding the shielded SPA geometry, it was shown that the charge of the microparticles was controlled by variation and asymmetry of the local ion density distribution. The latter occurred through measurements and analyses of the currents received by the electrodes as a function of the electric field strength between them.

In the pulsed and shielded SPA, all microparticles were effectively neutralised independently of the applied electric field strength. In the relevant experiments, the plasma discharge was switched off after all particles were spatially situated below the mesh grid (which shielded the plasma afterglow from the bulk). Full particle neutralisation was then experimentally demonstrated by spatially resolved particle charge measurements. Since the plasma discharge was pulsed, hardly any space charge was present at the moment of measuring the particle. In contrast, in the continuous shielded SPA (as discussed above), the ion space charge had a dominant role in the achieved charge control of the particles. In an ascending order of certainty, the

neutralisation of the particles could be caused by photo-detachment, neutralisation by (trapped) ions, and resonant charge exchange reactions.

Research line two experimentally revealed the charging of clustered microparticles in the free SPA, which literature has described by means of contradicting models. By direct measurements of the charge ratio $R_e = 2.1 \pm 0.2$ between two-particle clusters (doublets) ($9.8 \pm 0.9 e$) and single microparticles (singlets) ($4.6 \pm 0.1 e$), first experimental proof has shown that the charge on doublets is correctly described through the charge on the smallest enclosing sphere predicting $R = 2$ rather than by its capacitance predicting $R = 1.39$.

In the experiments, the particle size, mass and cluster configurations were determined based on the measured vertical velocity and on a flow model supported by empirical findings in the field of aerosol science. Compared to the negative particle charge measured in the free SPA in research line one, these experiments were performed with a five times lower plasma power. The latter is expected to be the dominant reason for the observed difference in particle charge and sign. The obtained insights into the plasma-charging of clusters contribute to the general understanding of plasma-charging of irregularly-shaped particles.

In the research described in this thesis, the microparticles charge of microparticles has been precisely controlled, ranging from small negative to even small positive charges. The achieved control provides insights into the complex interplay of plasma-induced particle charging processes. Not only is the particle charge determined by the plasma bulk, it also proves predominantly determined by the dynamics in its afterglow. These results regarding the charging of particles as well as the electric fields' influence bring the development and application of plasma-assisted particle filtering in various applications an important step closer.

Samenvatting

Vervuiling door stofdeeltjes is een enorm probleem in de huidige samenleving. Niet alleen omdat de wereldwijde toename van luchtverontreiniging de levensverwachting verkort van mensen in industriële gebieden, maar ook omdat stofdeeltjes een grote invloed hebben op het productieproces van zeer kleine en ingewikkelde onderdelen zoals elektronische chips voor computers en smartphones. In beide voorbeelden is het van cruciaal belang dat de verontreinigende deeltjes kunnen worden gecontroleerd en beperkt. In dit proefschrift worden de eerste en meest fundamentele stappen onderzocht in de richting van het verwijderen van stofdeeltjes uit een gasstroom met behulp van plasma.

Een plasma is een geïoniseerd gas, dat naast atomen of moleculen bestaat uit elektronen en ionen, waardoor plasma's de nano- tot microdeeltjes die erin zitten elektrisch kunnen opladen. Het plasma wekt bovendien zelf aan zijn grenzen hoge elektrische velden op. De combinatie van deze twee eigenschappen vormt de basis voor toekomstige plasma-ondersteunde technieken om luchtverontreiniging te kunnen verwijderen. Om de in de gasstroom zwevende deeltjes te kunnen afvoeren, hebben we kennis nodig over de oplaadmechanismen, niet alleen in het actieve plasmagebied, maar juist ook in de Ruimtelijke Plasma-Nagloed (RPN). Tot nu toe was wetenschappelijk onderzoek beperkt tot het opladen van deeltjes in temporele plasma-nagloeden, die aanzienlijk anders zijn wat betreft de evolutie van de plasmaparameters. Daarom levert dit onderzoek fundamentele inzichten in de grotendeels onbekende dynamiek van plasma-deeltjesoplading in de ruimtelijke plasma-nagloed.

De gepresenteerde kennis is verkregen uit experimenten en vereenvoudigde modellering van de lokale interactie tussen plasma en deeltjes. De experimenten werden uitgevoerd met behulp van een zelf ontworpen en ontwikkelde experimentele opstelling. In deze opstelling werden microdeeltjes geïnjecteerd in een vacuümomgeving. Daarna werden de deeltjes elektrisch opgeladen door een inductief gekoppeld plasma. De restlading van deze deeltjes en hun interactie met de nagloed van het plasma werden onderzocht door hun gedrag te volgen in een extern aangelegd elektrisch veld onder wisselende experimentele omstandigheden. De banen van de door het elektrische

veld beïnvloede deeltjes werden bestudeerd met behulp van laserlichtverstrooiing en hogesnelheidscamera's, gecombineerd met eigen software voor deeltjestracking.

Voor dit onderzoek werden de volgende twee onderzoekslijnen gedefinieerd.

- Onderzoekslijn één richt zich op de lading en het (ont)laden van bolvormige microdeeltjes in verschillende types ruimtelijke plasma-nagloeden door het bestuderen van het complexe samenspel van de oplaadprocessen die de deeltjes beïnvloeden.
- Onderzoekslijn twee toont experimenteel aan hoe geclusterde microdeeltjes worden opgeladen in de ruimtelijke plasma-nagloed. Tot nu toe werden in de literatuur verschillende tegengestelde modellen gebruikt om de lading van niet-sferische deeltjes te beschrijven. Geen enkele daarvan werd geverifieerd of weerlegd. Deze onderzoekslijn levert experimenteel bewijs om deze openstaande vraag te beantwoorden.

In onderzoekslijn één werd de deeltjeslading en het (ont)laden onderzocht in drie verschillende types RPN. In de vrije RPN (zonder fysieke obstructie tussen het actieve plasmagebied en de RPN) werd de lading van microdeeltjes nauwkeurig gemeten. Het experiment toonde een deeltjeslading aan van $-30 \pm 7 e$. Dit is drie ordes van grootte lager dan de typische deeltjeslading van $-10^4 e$ die in de kern van het plasma werd verwacht voor de gebruikte verzilverde melamineformaldehyde deeltjes met een diameter van $4.9 \pm 0.2 \mu\text{m}$.

Een relatief eenvoudig analytisch tijdschaalmodel onderzocht dit verschil in deeltjeslading tussen de kern en de RPN. Hieruit werd geconcludeerd dat het verschil in elektronentemperatuur tussen de kern van het plasma en het nagloedgebied voornamelijk het verschil in deeltjeslading verklaart.

In de afgeschermdede RPN is aangetoond dat de deeltjeslading nauwkeurig kan worden beïnvloed, variërend van kleine negatieve ($-40e$) tot zelfs kleine positieve ladingen ($+10e$) door alleen de grootte van het extern aangelegde elektrische veld te veranderen. De afgeschermdede RPN werd gecreëerd met behulp van een fijnmazig gaas in de dwarsdoorsnede van de opstelling, dat de kern van het plasma scheidde van zijn nagloed. De aanwezigheid van het gaas wekte een extra elektrische veld-component op tussen het gaas en de elektroden die gebruikt werden om een extern aangelegd elektrisch veld te creëren. Deze extra elektrische veld-component beïnvloedde de ruimtelijke ladingsverdeling van de positieve ionen en maakte zo de controle van de deeltjeslading mogelijk. In de vrije RPN was deze elektrische veld-component daarentegen veel kleiner door de afwezigheid van dit gaas. In de geometrie van de afgeschermdede RPN werd aangetoond dat de lading van de microdeeltjes was beïnvloed door variatie en asymmetrie van de lokale ionendichtheidsverdeling. Dit werd onderbouwd door middel van metingen en analyse van de stromen die door de elektroden werden opgevangen als een functie van de elektrische veldsterkte daartussen.

In de gepulseerde en afgeschermdede RPN werden alle microdeeltjes effectief geneutraliseerd, onafhankelijk van de aangelegde elektrische veldsterkte. In de experimenten werd het plasma uitgeschakeld nadat alle deeltjes zich ruimtelijk onder het gaas bevonden (dat de plasma-nagloed afschermdede van de kern). Daarna werd de volledige

neutralisatie van de deeltjes experimenteel aangetoond door metingen van de ruimtelijk opgeloste deeltjeslading. Aangezien het plasma gepulseerd was, was er op het moment dat de deeltjeslading werd gemeten nauwelijks ruimtelading aanwezig. In de continu afgeschermd RPN (zoals hierboven besproken) speelde de ionenruimtelading daarentegen een dominante rol bij de bereikte ladingscontrole van de deeltjes. In oplopende volgorde van zekerheid zou de neutralisatie van de deeltjes veroorzaakt kunnen zijn door photodetachment, neutralisatie door (opgesloten) ionen en resonante ladingsuitwisselingsreacties.

Onderzoekslijn twee onthult experimenteel hoe geclusterde microdeeltjes opladen in de vrije RPN, wat in de literatuur door tegenstrijdige modellen werd beschreven. Door directe metingen van de ladingsverhouding $R_e = 2.1 \pm 0.2$ tussen clusters van twee deeltjes ($9.8 \pm 0.9 e$) en enkele microdeeltjes ($4.6 \pm 0.1 e$), werd het eerste experimentele bewijs geleverd dat de lading op twee-deeltjes-clusters correct wordt beschreven door de lading van de equivalent kleinste omsluitende bol met als voorspelling $R = 2$ en niet door de capaciteit ervan met als voorspelling $R = 1.39$.

In de experimenten werd de grootte, massa en cluster configuratie van de deeltjes bepaald op basis van de gemeten verticale snelheid en met een stromingsmodel dat werd ondersteund door empirische bevindingen op het gebied van de aerosolwetenschap. Vergeleken met de negatieve deeltjeslading in de vrije RPN in onderzoekslijn één, werden deze experimenten uitgevoerd met een vijfmaal lager plasmavermogen. Dit lager plasmavermogen is waarschijnlijk de hoofdoorzaak van het waargenomen verschil in deeltjeslading en polariteit. De verkregen inzichten in de plasmalading van clusters dragen actief bij tot het algemeen begrip van de plasmalading van onregelmatig gevormde deeltjes.

In het onderzoek beschreven in dit proefschrift is de lading van microdeeltjes nauwkeurig beïnvloed, variërend van kleine negatieve tot zelfs kleine positieve ladingen. De bereikte controle geeft inzicht in het complexe samenspel van de deeltjesladingsprocessen die worden opgewekt door het plasma. De lading van de deeltjes wordt niet alleen bepaald door de kern van het plasma, maar voornamelijk door de dynamiek in de nagloed ervan. Deze inzichten over het opladen van deeltjes en de invloed van de elektrische velden daarop, brengen de ontwikkeling en het gebruik van het filteren van deeltjes met behulp van plasma in verschillende toepassingen een aanzienlijke stap dichterbij.

Contents

Summary	vii
Samenvatting	xi
1 Introduction	1
1.1 Introduction	2
1.2 (Complex) plasmas	2
1.3 The charge of particles: a key parameter	4
1.4 Plasma-assisted particle contamination control	5
1.5 Thesis focus	5
1.6 Thesis structure	7
2 The physics of complex plasmas and the applied flow	9
2.1 Introduction	10
2.2 Plasma	10
2.2.1 Basic properties of plasma	10
2.2.2 Inductively coupled plasmas	12
2.2.3 Plasma afterglow	13
2.2.4 Complex plasma	14
2.3 Charge and charging of dust particles	14
2.3.1 Charging processes	14
2.4 Forces on particles	17
2.4.1 Gravity	17
2.4.2 Buoyancy	17
2.4.3 Electrostatic force	18
2.4.4 Neutral drag force	18
2.4.5 Ion drag force	19
2.4.6 Thermophoretic force	20

2.4.7	Radiation pressure force	21
2.4.8	Comparison of magnitude of forces	21
2.5	Flow	22
2.5.1	Entrance effects	22
2.5.2	Flow profile	23
3	From experiments to charge	25
3.1	Introduction	26
3.2	The setup and its main diagnostic	26
3.2.1	Microparticles	28
3.2.2	Particle dispenser	28
3.2.3	Laser light scattering	29
3.2.4	Showerhead	30
3.2.5	Plasma source	31
3.2.6	Rogowski electrodes	31
3.2.7	High-speed camera	32
3.2.8	Charge measurement	33
3.3	Particle tracking	34
3.3.1	Particle detection	34
3.3.2	Particle linking	35
3.3.3	Trajectory analysis	35
3.4	Proof of principle	36
3.4.1	Experimental parameters and reheating of electrons	36
3.4.2	Accuracy of charge measurements	36
3.4.3	Charge distribution	37
3.4.4	Decharging model	38
3.4.5	Comparison of model and results	40
3.5	Conclusion	42
4	Charge control of microparticles in a shielded plasma afterglow	43
4.1	Introduction	44
4.2	Particle charging theory	45
4.3	Experimental setup	46
4.3.1	Particle and gas injection	48
4.3.2	Active plasma region	49
4.3.3	Rogowski electrodes	49
4.3.4	Particle trajectory imaging	51
4.3.5	In-house developed particle tracking software	52
4.3.6	Charge measurement	53
4.4	Results of charge control	54
4.5	Physical interpretation	56
4.5.1	Active plasma region	56
4.5.2	Sheath above mesh grid	57
4.5.3	Shielded spatial plasma afterglow	59
4.6	Conclusion	63

5	Charge neutralisation of microparticles by pulsing a shielded spatial plasma afterglow	65
5.1	Introduction	66
5.2	Theory	67
	5.2.1 Plasma decay	67
	5.2.2 Particle charging	68
5.3	Experiment	69
	5.3.1 Setup	69
	5.3.2 Procedure	72
5.4	Results	74
5.5	Physical interpretation	77
	5.5.1 Neutralisation by (trapped) ions	78
	5.5.2 Neutralisation by photodetachment	78
	5.5.3 Neutralisation by charge exchange	78
5.6	Conclusion	79
5.7	Appendix	79
	5.7.1 Positive acceleration after neutralisation	79
	5.7.2 Constant spread in acceleration	81
	5.7.3 Measured acceleration at the end of FoV 2	82
6	Revealing the charge of clustered microparticles	85
6.1	Introduction	86
6.2	Results	87
	6.2.1 Cluster sizes	87
	6.2.2 Charge distributions	90
6.3	Discussion	90
6.4	Conclusion	91
6.5	Methods	91
	6.5.1 Experimental setup	91
	6.5.2 Cluster detection	94
7	Overall conclusions	97
8	Conclusions for applications	101
	Bibliography	105
	List of publications	121
	Acknowledgements	125
	Curriculum vitae	129

Chapter 1

Introduction

Abstract

In today's society, plasma-based applications can be of crucial importance to solve dust particle contamination problems, such as air pollution and particle contamination in the fabrication of ultra-clean high-tech systems. This first chapter places the research presented in this thesis into perspective and highlights its value for related research fields and applications. To that end, an introduction to plasmas and the charging of particles in plasmas has been included, as well as a description of the thesis' research aims and structure.

1.1 Introduction

Dust is everywhere. In our homes, getting rid of dust can be cumbersome. Yet, in other situations, it can even prove to be problematic. Figure 1.1 shows three important cases which were or still are crucial for (the creation of) today's society and are strongly affected by the presence of dust.

Figure 1a shows a wafer handler which is developed, designed and produced by VDL Enabling Technologies Group (ETG) for application in state-of-the-art photolithography systems in which particle contamination control is of the utmost importance to protect the wafers. These wafers are, in essence, the starting point of all produced electronic chips. Since the current typical size of the features in small electronics are as small as 13 nm [1], one can imagine the destructive effect nano- to micrometre-sized dust particles can have during the production process.

Figure 1b illustrates the vast effect of smog, i.e. air pollution in industrial and urban centres, posing a danger to people living in those areas. It is proven that, with daily exposures to (ultra-fine) dust particles at work, life expectancy will be reduced by about 38 months [2]. Figure 1c shows an artist's impression of a young star surrounded by a dusty protoplanetary disk. In such environments, dust particles aggregate and form bigger particles in order to create the initial seeds for planetesimal formation, eventually leading to the formation of planets.

The respective figures share the understanding that the charging of particles embedded in partly ionised media is of the utmost importance. The two applications shown in Figures 1a and 1b could benefit significantly from plasma-assisted techniques to filter the dust particles out of the air or out of the production process and, therefore, avoid contamination. In astrophysics, the particle charge plays a crucial role in dust particle aggregation in protoplanetary disks, which eventually leads to planet formation. Moreover, fully understanding this process would contribute to the understanding of the formation and development of our solar system.

In this chapter, the basics of plasma and its afterglow are introduced in section 1.2. In section 1.3, the relevance of this research is conveyed by reviewing the importance of particle charging in numerous processes and applications. This is then followed by the working principle of plasma-assisted contamination control strategies in section 1.4. The introduction concludes with the research aim in section 1.5, followed by the thesis structure in section 1.6.

1.2 (Complex) plasmas

This research deals with partly ionised gas - a plasma - which in addition to atoms or molecules consists of charged species: electrons and ions. Compared to normal gas, these charges species significantly alter the properties of plasma. The latter is therefore commonly referred to as the fourth state of matter besides solid, liquid and gas. Although ninety-nine per cent of all visible matter in our universe consists of plasma, it was not until 1879 that Sir Williams Crookes identified the plasma state which he named "radiant matter" [3]. The term plasma was introduced by Irving Langmuir, as it reminded him of how blood plasma carried its components [4].



Figure 1.1: a) Wafer handler for photolithography applications being inspected, b) [Smog descends on Wuhan, Hubei China](#) by 云中君, licensed under [CC BY](#) / zoom from original, and c) [Planet-Forming Disk Around a Baby Star](#) by [NASA Universe](#), licensed under [CC BY](#) / zoom from original.

Well-known plasmas that can be found in nature are, for example, the sun (in essence a large ball of hot plasma), lightning, and the aurora borealis and australis (northern and southern lights). In laboratories, plasmas are often made by the application of an electric field to a gas. When the applied electric field is sufficiently large, breakdown will occur, in which electrons are freed from being bound to an atom, and a plasma is formed. This thesis studies a low-pressure plasma, i.e. the plasma created in an environment which has a pressure below atmospheric pressure. A characteristic of low-pressure plasmas (and also of some atmospheric plasmas) is its non-thermal state: the electrons are hot, typically 10 000 K, while the background gas remains close to room temperature. The non-thermal property of plasmas forms the cornerstone of many applications [5], such as plasma deposition [6, 7] and etching, [8], medicine [9], lighting [10], gas treatment [11, 12] and particle contamination control [13].

This thesis studies the interaction between small dust particles and plasma. Nano- to micrometre-sized particles can be inserted into a plasma, but can also be created by chemical reactions induced in it [14, 15]. The common term for a plasma that consists of neutrals, electrons and ions, and also of (charged) dust particles, is complex or dusty plasma. The freely moving electrons and ions tend to charge the larger dust particles, which drives numerous fundamental processes in various research fields, as will be explained in the following section. The particle charging in low-pressure plasmas is the main subject of this research.

In this work, the charging of dust particles is studied in a unique region of the plasma, i.e. its afterglow. The afterglow is the region where the plasma is not actively powered, i.e. the electric fields in the afterglow region are so small that heating of electrons is negligible. There are two different types of afterglows: temporal and spatial plasma afterglows. A temporal afterglow is created by switching off the plasma discharge, rendering it transient in time until all the plasma species have decayed. On the other hand, a Spatial Plasma Afterglow (SPA) is transient in space and constitutes the region just outside of the active plasma region. This thesis comprises a study of the particle charge and (de)charging in SPAs.

1.3 The charge of particles: a key parameter

The charge of (non-spherical) particles is a key parameter in many research fields such as complex plasma physics, astrophysics and aerosol science. In complex plasma physics, the particle charge drives many elementary processes, such as ion drag [16, 17], local Debye shielding [18], and Coulomb-interactions in strongly coupled plasmas [19, 20]. Moreover, during the plasma-assisted growth process of (nano)particles, the particle charge forms a key parameter steering the majority of the relevant elementary processes [21–27].

In astrophysics, particular attention is attributed to the charging of clustered particles [28–33], since these are commonly found in protoplanetary disks (see Figure 1c) where planet formation takes place [31–34]. The particle charge in these environments is essential for the aggregation process, leading to their explosive growth. In aerosol science, extensive research has reported on the charging of non-spherical particles at atmospheric pressures [35–40], with the particle charge being of vital importance in

determining the particles' size in differential mobility analysers that are often used for research purposes.

An understanding of the charging mechanisms of (non-spherical) particles embedded in media where free charge carriers are present is therefore of vital importance in a wide range of fundamental fields. Not only is the particle charge, as discussed above, an essential parameter in numerous fundamental processes, it also holds importance for many applications. For example, it has been shown that the charge of nanoparticles (NPs) in medications influences drug delivery and imaging [41–43]. Although having a higher cytotoxicity, positively charged NPs improve the efficacy of imaging, gene transfer and drug delivery [44].

Gold NPs are also frequently used in colourimetric sensing [45–48]. In this application, the aggregation of NPs is used, which is heavily influenced by their charge. Neutralisation of the NPs results in improved detection time, signal stability and sensitivity of the technique [49].

Another prominent example in this framework is the semiconductor industry. This major industry deals with the fabrication of delicate computer chips, a process in which particle contamination control is of the utmost importance [50]. The following section elaborates on why the particle charge forms the key parameter in potential plasma-assisted particle contamination control strategies and could, therefore, be highly beneficial for the production of ultra-clean systems in the semiconductor industry.

1.4 Plasma-assisted particle contamination control

The potential of plasma-assisted particle contamination control stems from the ability of plasma to electrically charge particles immersed in it [16], as well as to control particle trajectories by means of the self-induced electric fields at its boundaries [51]. The position and trajectory of plasma-charged particles may also be controlled by externally applied electric fields. In a practical application, this means that the contaminating particles are charged and discharged in a spatially limited region of plasma before being deflected by electric fields in the SPA.

To enable further developments of these contamination control strategies, knowledge of the charge and (de)charging of (non-spherical) particles in the SPA is desired. The few relevant plasma afterglow particle charging studies that were performed are limited to temporal plasma afterglows [52–59]. Compared to an SPA situation, those studies differ fundamentally regarding the distinct evolution of plasma parameters, such as electron temperature and plasma density.

1.5 Thesis focus

The research presented in this thesis has been conducted in the research group Elementary Processes in Gas Discharges (EPG) at the Eindhoven University of Technology. EPG has a long history of studying complex plasmas which is, for example, described in numerous PhD theses [60–67]. The current thesis focuses on the SPA of complex plasmas as described in the research goal below.

This research aims to obtain a fundamental understanding of the charge and (de)charging of microparticles in low-pressure spatial plasma afterglows.

The objective of this thesis has been divided into two research lines, mapped in the research framework displayed in Figure 1.2.

- The first research line focuses on the charge and charging of spherical microparticles in different types of SPAs through a study of the complex interplay of the charging processes in this region.
- The second research line reveals how clustered microparticles in the free SPA are charged. In the literature, several models are used to describe the charge of non-spherical particles none of which have been verified or refuted. Experimental proof answers this outstanding question.

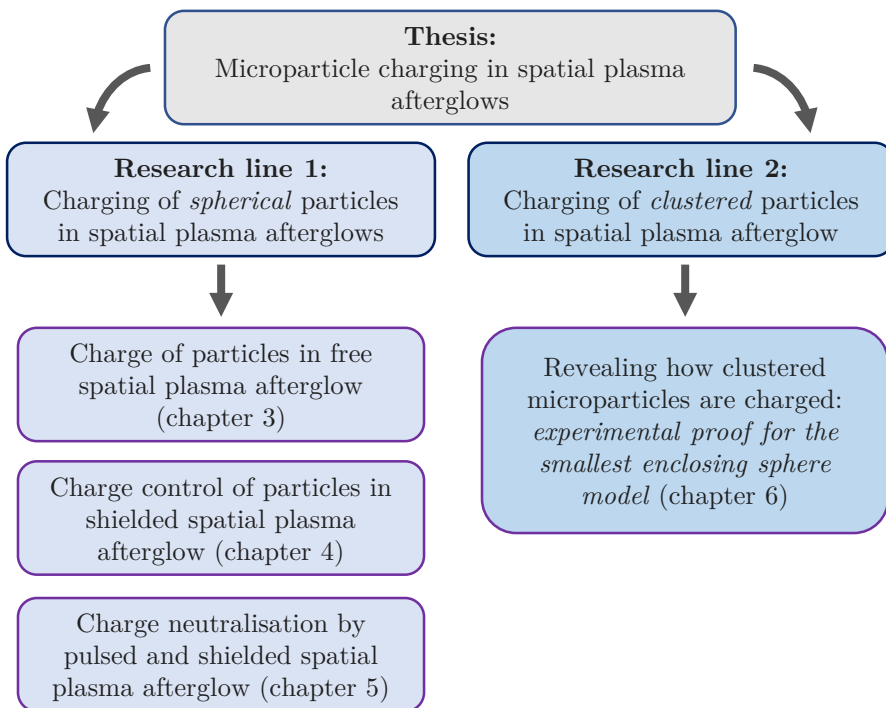


Figure 1.2: Overview of the thesis’s research framework. The research is divided into two research lines of which the results are discussed in chapters 3-6.

1.6 Thesis structure

The structure of this thesis is as follows:

Chapter two describes the physics of dusty plasmas and the relevant (plasma-induced) forces acting on the microparticles under these conditions.

Research line one comprises three chapters, each dedicated to the charge and charging in a different type of SPA:

Chapter three presents and discusses the experimental setup and the in-house developed particle tracking software, as well as charge measurements in the free SPA as a proof of principle test case. Moreover, it introduces a relatively simple timescale model to analyse the charge and (de)charging under these conditions.

Chapter four shows that the charge of microparticles can be accurately controlled in the shielded SPA. For this purpose, a mesh grid was used that shielded the afterglow from the plasma bulk. The governing mechanism of the measured particle charge control is presented and supported by measurements of the (plasma) currents in the shielded SPA.

Chapter five discusses the neutralisation of microparticles by pulsing the shielded SPA. Spatially resolved particle charge measurements are presented that show the particles' full neutralisation.

Research line two consists of one chapter:

Chapter six reveals the charge of clustered microparticles in the free SPA. By direct measurements of the particles' mass, size and charge, experimental proof is presented that pinpoints the model correctly describing the charge of non-spherical particles in SPAs at low pressure.

Chapter seven and **eight** finalise this research with general conclusions drawn from the respective chapters.

The physics of complex plasmas and the applied flow

Abstract

This chapter describes the physics important for the complex plasma experiments described in this research. In the latter, the studied microparticles are injected in an Inductively Coupled Plasma of which the basics are described. In addition, the plasma afterglow is treated, which refers to the plasma state after the ionisation source has been removed. When microparticles are inserted in a plasma, they are charged by the plasma species. This plasma-induced charging process and other relevant charging mechanisms taking place in the experiments are discussed. Also, an overview of the forces acting on the microparticles is given. Estimates of these forces show that gravity and neutral drag are dominant in the vertical direction, whereas in the horizontal direction, the electrostatic force stands out. In the experiments, a flow is introduced which influences the particle trajectories. A discussion of the flow profile and its entrance effects concludes the chapter.

2.1 Introduction

This chapter discusses the relevant theory needed for an understanding and analysis of the research presented in this thesis. Section 2.2 discusses the basics of radio frequency (RF) plasmas (subsection 2.2.1) with special attention for inductively coupled plasmas (subsection 2.2.2), followed by a discussion of the plasma afterglows basics (subsection 2.2.3) and complex plasmas (subsection 2.2.4). section 2.3 deals with the charging mechanisms of particles contained in plasmas. An overview of the relevant charging processes is given (subsection 2.3.1), including a discussion of the Orbital Motion Limited (OML) theory. All particles, charged or otherwise, are subject to several forces. These forces are treated in section 2.4. This chapter is finalised by a short overview of the relevant flow physics in section 2.5 which describes the flow profile and its entrance effects applied in the experiments discussed in chapter 3-5.

2.2 Plasma

As explained in the introduction (section 1.2), a plasma is an ionised gas, which consists not only of atoms or molecules but also of electrons, ions and excited species. This section discusses the physics of (complex) plasma and its afterglow.

2.2.1 Basic properties of plasma

Laboratory plasmas are generally created by sufficiently strong electric fields, which vary widely in terms of the frequency applied. Examples of regularly used plasmas are DC, AC (kHz range), RF (MHz range) and microwave (GHz range) plasmas. In the research presented in this thesis, a radiofrequency plasma (RF) plasma is used, which differs from most other types of plasmas in terms of the charged particles' ability to follow the applied electric field.

Plasma frequency

A crucial parameter to explain the ability of charged particles in the plasma to follow the applied electric field is the plasma frequency, given by

$$\omega_{e,i} = \sqrt{\frac{n_{e,i} Z_{e,i}^2 e^2}{m_{e,i} \epsilon_0}}. \quad (2.1)$$

Here, n_e and n_i stand for the electron and ion densities. $Z_{e,i}$ and $m_{e,i}$ represent the charge number and mass of the electrons and ions, while e stands for the elementary charge of an electron and ϵ_0 for the dielectric constant of vacuum. For a typical low-pressure plasma with $n_{e,i} = 1 \times 10^{15} \text{ m}^{-3}$, the plasma frequency of electrons and ions is $\omega_e/2\pi \approx 284 \text{ MHz}$ and $\omega_i/2\pi \approx 1 \text{ MHz}$ respectively. The vast difference in plasma frequency between ions and electrons is due to the disparity between the mass of both. In an RF plasma, which is often operated at 13.56 MHz, only the electrons have sufficiently small inertia to be able to follow the electric field oscillations. Consequently,

while the electrons are heated, the ions are only subject to the time-averaged electric fields, such as those present in the plasma sheath (as will be discussed later on in this section). Equation 2.1 predicts the substantial difference in power coupling between the different types of laboratory plasmas. In AC and DC plasmas, both electrons and ions can follow the field and are thus heated, in sharp contrast with an RF plasma.

Ionisation degree

The power delivered to the plasma discharge results in ionisation of the gas species. For a plasma consisting solely of electrons and positively charged ions, the ionisation degree is given by

$$\alpha = \frac{n_{e,i}}{n_{e,i} + n_n}, \quad (2.2)$$

where n_n is the density of the neutral gas species. A higher plasma power generally leads to more ionisation reactions and, thus, to a higher ionisation degree.

Debye length

A fundamental property of plasmas is quasi-neutrality. In the simplest case, this means that the total number of electrons and positive ions in a certain volume must balance at all times. Overall the plasma is neutral, however charge variations can occur on a length scale smaller than the so-called Debye length

$$\lambda_{D_{e,i}} = \sqrt{\frac{\epsilon_0 k_b T_{e,i}}{e^2 n_{i,e}}}. \quad (2.3)$$

Here, $T_{e,i}$ represents the electron or ion temperature. Even though the Debye length can differ for electrons and ions, it is regularly used without specifying the species in the form of the linearised Debye length

$$\frac{1}{\lambda_D^2} = \frac{1}{\lambda_{D_e}^2} + \frac{1}{\lambda_{D_i}^2}. \quad (2.4)$$

In the bulk of low-pressure plasmas $T_e \gg T_i$, in which case $\lambda_D \approx \lambda_{D_i}$.

Mean free path

In addition the Debye length, the mean free path also forms an important length scale in plasmas. It is defined as the distance between two subsequent collisions of a specific particle (1) (for example: electrons, ions or neutrals) with other particles (2), and is given by

$$\lambda_{\text{mfp},1} = \frac{1}{n_2 \sigma_{12}}. \quad (2.5)$$

Here, n_2 represents the density of particle (2) and σ_{12} the cross-section for collisions between species (1) and (2).

Plasma sheath

When plasma comes into contact with a surface, a positive space charge region near the surface, the plasma sheath, is formed. In principle, it is created to enable the plasma to remain quasi-neutral. When the plasma is initially switched on, electrons and ions travel to the surface of interest. The electrons, having much higher mobility (lower mass), reach the surface with higher velocities than the ions. At this initial stage, the electron flux towards the surface therefore exceeds the ion flux and, as a result, the surface becomes negatively charged. In turn, this negative charge repels the approaching electrons, whereas it attracts the ions. This mechanism continues until the electron and ion flux to the surface balance and quasi-neutrality is secured. As a consequence, the surface obtains a negative bias voltage with respect to the plasma, and a space charge region in which the ion density dominates over the electron density is formed in front of the surface. This sheath region is typically a few Debye lengths thick and is dependent on the collisionality, i.e. the pressure of the discharge [68].

2.2.2 Inductively coupled plasmas

For the purpose of this thesis, an Inductively Coupled Plasma (ICP) is used which is driven by radiofrequency oscillating fields. In ICPs, the power is transferred from induced electric fields to the plasma electrons rather than directly from the applied electric field in the case of capacitively coupled plasmas. A coil wrapped around a tube constitutes a common configuration for the generation of an ICP in which the electrons do not directly contact the coil.

As depicted in Figure 2.1, an ICP can be modelled as a transformer-coupled circuit. An RF-voltage is applied to a coil with self-inductance L_{11} and mutual inductance L_{12} between the actual coil and the inductance of the plasma (a virtual coil). In this model, the plasma consists of a resistive part R_p and an inductance L_p in order to account for the phase lag between the applied RF field and the RF conduction current due to the finite electron inertia [69]. To ensure efficient power coupling, a matchbox is generally used to convert the complex plasma impedance at the RF-frequency to a $50\ \Omega$ resistive load seen by the amplifier.

Since the amplitude of induced electromagnetic waves decreases when penetrating a conducting medium (which a plasma generally is), the electrons are only heated in a thin layer near the surface of the plasma, the so-called skin-depth layer δ . In a low-pressure plasma, where the electron-neutral collision frequency ν_m is much smaller than the operation frequency ω of the ICP, the skin depth is given by

$$\delta = \sqrt{\frac{m_e}{e^2 \mu_0 n_{es}}} \quad (2.6)$$

where n_{es} is the electron density in the skin-depth layer and μ_0 the vacuum permeability. Equation 2.6 only holds when δ is much smaller than the typical radius R and length l of the coil that is used for the generation of the discharge.

Electrodeless RF discharges can be operated in two different power coupling regimes: the so-called E- and H-modes [70, 71]. In the E-mode, the plasma is sustained by a capacitively coupled discharge since a significant voltage drop across the plasma sheath

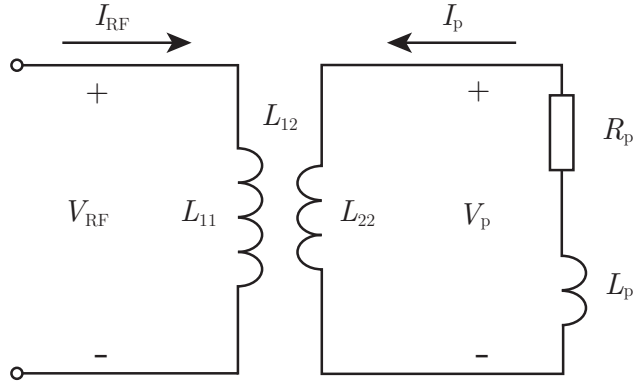


Figure 2.1: Schematic illustration of the equivalent transformer coupled model of an inductively coupled discharge.

exists [72]. This mode is characterised by low plasma powers and is always present when the plasma is ignited. In the H-mode, the inductive coupling prevails. Compared to the E-mode, it is characterised by an approximately two orders of magnitude higher plasma density and a much brighter light emission [73]. In chapter 4, it will be shown that in this thesis' experiments, the ICP is operated in the E-mode.

2.2.3 Plasma afterglow

This research focuses primarily on the particle dynamics in the afterglow region of the plasma. The term afterglow refers to the plasma state after the ionisation source has been removed, which can occur both in time (temporal plasma afterglow) and in space (spatial or remote plasma afterglow). In the afterglow, the plasma species transit back to the gas state, mostly recombining at a third body, such as the setup walls in case of relatively low-pressure discharges. Moreover, electrons lose (part of their) energy due to collisions with gas species [74] as well as diffusion to and successive recombination at the walls of the setup [75]. In chapter 3, a timescale model is presented that investigates the particle charge in the spatial plasma afterglow through a careful analysis of the plasma processes in this region.

Due to the decrease in plasma density, the governing mechanism for diffusion can change in plasma afterglows. As long as the Debye length is much smaller than the typical diffusion length Γ (determined by the geometry of the setup), plasma species diffuse jointly, coupled by Coulomb interactions, which is called ambipolar diffusion [16]. For plasma densities where $\lambda_D \gg \Gamma$, electrons and ions are no longer coupled and can diffuse freely. Chapter 5 discusses the transition from ambipolar diffusion to free diffusion taking place in the afterglow and its influence. The plasma afterglow can be affected by metastables (long-lived excited states) the presence of which strongly depends on the gas type. When present, these species can lead to super-elastic collisions heating the electrons [76].

2.2.4 Complex plasma

As explained in the introduction, a complex plasma consists, in addition to neutral (atoms or molecules) and charged species (electrons and ions), also of nano- to micrometre-sized particles which often become charged when interacting with the plasma. For the purpose of this thesis, mono-disperse microparticles are injected into the plasma. Complex plasmas are often created with large amounts of particles to study, such as phase transitions under microgravity conditions [77]. In the current research, a low microparticle density is used such that mutual Coulomb interactions between the particles can be neglected and only the interaction between particles and plasma remains as subject of investigation.

2.3 Charge and charging of dust particles

Similar to the description of the sheath formation in subsection 2.2.1, microparticle charging in a plasma environment can be described by the balancing of plasma species arriving at their surface. The evaluation of this current balance in the plasma bulk is not straightforward and has been subject to discussion in the literature over the past few decades. This is mainly because particle charging forms a mesoscopic process; some properties are described by theories also applicable to bulk material properties, whereas others can only be described using molecular theories. For example, the charge analysis of a microparticle in a plasma radiated by a laser requires knowledge of the microscopic surface processes occurring (electron attachment, ion capture, recombination) as well as an understanding of the macroscopic work function to study the laser effect. The particle work function constitutes a bulk property for particles larger than approximately 10 nm [25].

2.3.1 Charging processes

What follows is a brief overview of the relevant particle charging processes contained in this thesis.

Collection of charge carriers

In a plasma environment, dust particles varying in size from nano- to micrometres, are charged by the plasma species arriving at (and sticking to) their surface. As explained earlier, the mobility of electrons is much higher than that of ions, which causes electrons to dominate the initial current to the particles. In the plasma bulk, the particles therefore become negatively charged until an equilibrium between the fluxes is achieved.

The principal theory describing the process of particle charging by the collection of plasma species is called the Orbital Motion Limited (OML) theory and was originally developed for Langmuir probes by Mott-Smith and Langmuir in 1926 [78], representing, in principle, a relatively straightforward theory. The OML theory assumes that an isolated particle is surrounded by a “thick” sheath in comparison with the particle’s size ($\lambda_D \gg r_p$). Moreover, it assumes that the sheath around the particle is collisionless

for both electrons and ions ($\lambda_D \ll \lambda_{\text{mfp}}$), and that these species are collected by the particle when their orbits overlap the particle surface. Accordingly, the ion (I_i) and electron (I_e) current for Maxwellian electrons and exclusively positive ions collected by the particle are given by [79]

$$I_{i,e} = \begin{cases} I_{i0,e0} \left(1 - \frac{q_{i,e} \phi_s}{k_b T_{i,e}}\right) & \text{if } q_{i,e} \phi_s \leq 0 \\ I_{i0,e0} \exp\left(-\frac{q_{i,e} \phi_s}{k_b T_{i,e}}\right) & \text{if } q_{i,e} \phi_s \geq 0. \end{cases} \quad (2.7)$$

The plasma currents depend on the surface potential of the particle ϕ_s as well as on the charge of both ions q_i and electrons q_e and their temperature $T_{i,e}$. Furthermore, in Equation 2.7, $I_{i0,e0}$ is the current collected at $\phi_s = 0$

$$I_{i0,e0} = \pi r_p^2 n_{i,e} q_{e,i} \sqrt{\frac{8k_b T_{i,e}}{\pi m_{i,e}}}. \quad (2.8)$$

In equilibrium, the particle charge does not change due to arriving plasma species and the sum of the plasma currents is given by

$$\frac{\partial Q}{\partial t} = I_i + I_e = 0. \quad (2.9)$$

By assuming $n_i = n_e$ (which is generally the case in a quasi-neutral plasma) and $q_i = -q_e$, the particle's surface potential is determined by equating the electron and ion currents

$$\sqrt{\tilde{T}} \exp(-y) = \sqrt{\frac{m_e}{m_i}} (1 + \tilde{T} y), \quad (2.10)$$

where $y = \frac{e\phi_s}{k_b T_e}$ and $\tilde{T} = \frac{T_e}{T_i}$. Equation 2.10 shows that ϕ_s does not depend on the size of the particles or the plasma density, but solely on \tilde{T} . By considering a particle as a capacitor with capacity $C = 4\pi\epsilon_0\epsilon_r r_p$ with ϵ_r the relative permittivity, the particle charge is described by

$$Q = 4\pi\epsilon_0\epsilon_r r_p \phi_s \quad (2.11)$$

Collisionality corrections to OML The OML theory, as described above, assumes both electrons and ions to be collisionless. For $\lambda_D/\lambda_{\text{mfp,ia}} \approx 10^{-1}$, the particle charge is lowered because ion-neutral collisions increase the residence time of ions and consequently also the ion current [16, 80, 81]. For increasing $\lambda_D/\lambda_{\text{mfp,ia}}$, the ion current is reduced and the particle charge becomes more negative. At maximum, these effects change the charge of the particles by a factor of two to three compared to the OML predicted particle charge [16, 80, 81].

Secondary electron emission

When highly energetic electrons or ions collide with the surface of a particle, secondary electrons can be ejected from it when the energy of the incoming species is high enough

to cause ionisation of the surface material [82]. The probability for secondary electron emission depends not only on the energy of the colliding particle, but also on the work function of the particle's material. For a nanometre-sized particle, the work function can differ significantly from its bulk value due to an image charge induced on its surface [25].

Photoemission

Photons arriving at the surface of a particle can either detach electrons when an excess of electrons is present, or photoionise the particle material when the photon energy is above the threshold for the corresponding process. It stands to reason that the energy required for the latter is significantly higher than that needed for photodetachment. For both processes, the photoemission depends on the particle's material properties, the energy of the incoming photon and the surface potential [83]. Photodetachment typically requires UV photons [84], whereas photoionisation requires deep UV or EUV photons [85].

Thermionic emission

When the thermal energy of a particle overcomes its work function, electrons are ejected. This process, called thermionic emission, generally occurs for particles that are heated intensively for a short period by, for example, intense laser pulses. For polycrystalline silver with a work function of 4.3 eV, thermionic emission requires a particle temperature of approximately 1000 K [86].

Field emission

In contrast to the previously discussed charging processes, field emission does not require an energetic incoming specie, but rather the presence of a strong electric field. Under the influence of this electric field, some electrons can tunnel through the potential barrier and are thereby ejected from the particle. Not taking into account the shape of the particles, i.e. local field enhancement effects, the electric field strength threshold for field emission is around 10^9 V m^{-1} [87].

Resonant charge exchange

Resonant charge exchange transfer (RCT) also involves the tunnelling of electrons. In this case, a particle can lose an electron through the interaction with an excited atom or molecule. When the energy level of the excited state lies within the conduction band, electrons can tunnel through the potential barrier between the particle and the colliding excited specie [88]. RCT is, amongst other factors, determined by the surface state of the particle [89], which makes it a complicated process for the purposes of an accurate analysis.

Triboelectric charging

Triboelectric charging is a form of contact charging, i.e. it only requires a particle and a surface such as the surface of another particle. It is best known for the static electric charge one builds up when, for example, rubbing a balloon over hair. This effect is typically explained by the difference in work function between conducting materials. To describe the charging in the balloon-hair example, a charging description of the local surface states and defects is required [90], since electrons cannot move freely in an insulator. Triboelectric charging is a peculiar phenomenon, as the reasons on why completely identical particles are also able to charge each other are not fully understood [91,92].

In the experiments presented in this thesis, the particles are triboelectrically charged before injection in the setup (as will be discussed in chapter 3, section 3.2). Yet, this initial charge is always reset by the plasma charging effect.

2.4 Forces on particles

When dust particles are injected into plasma and its spatial plasma afterglow, they are influenced by several forces. This section discusses the forces acting on single microparticles. The forces acting on clustered microparticles are treated in chapter 6 where they are relevant for the interpretation of those experiments. This section first discusses gravity, buoyancy and the electrostatic force. Subsequently, the three relevant drag forces are treated: the neutral drag force (subsection 2.4.4), the ion drag force (subsection 2.4.5), and the thermophoretic force (subsection 2.4.6). This section concludes with a discussion on the radiation pressure and an overview of the typical magnitude of the presented forces.

2.4.1 Gravity

Every object on earth is subject to gravity; and so are microparticles. For a spherical particle of radius r_p and density ρ_p , the gravitational force is given by

$$\mathbf{F}_g = \frac{4}{3}\pi r_p^3 \rho_p \mathbf{g} \quad (2.12)$$

where \mathbf{g} is the gravitational acceleration.

2.4.2 Buoyancy

In a fluid with density ρ_n , gravity is partially counteracted by buoyancy (also called upthrust). The well-known Archimedes principle [93] states that the magnitude of buoyancy is equal to the weight of the fluid displaced by the object and can therefore be expressed as

$$\mathbf{F}_b = -\frac{4}{3}\pi r_p^3 \rho_n \mathbf{g}, \quad (2.13)$$

in most gasses $\rho_n \ll \rho_p$.

2.4.3 Electrostatic force

A microparticle with charge Q experiences an electrostatic force \mathbf{F}_e in the presence of the electric field \mathbf{E}

$$\mathbf{F}_e = Q\mathbf{E}. \quad (2.14)$$

When the electric field is generated by a neighbouring particle, Equation 2.14 results in

$$\mathbf{F}_{C,1} = k_e Q_1 Q_2 \frac{\mathbf{r}_1 - \mathbf{r}_2}{|\mathbf{r}_1 - \mathbf{r}_2|^3}, \quad (2.15)$$

where $k_e = 1/4\pi\epsilon_0$ with ϵ_0 representing the vacuum electric permittivity, and Q_i and \mathbf{r}_i the charge and the position vector of particle i . Equation 2.15 assumes the particles to be point charges. In a plasma, the presence of the electrons and ions (partially) shield the charge of microparticles. Therefore, the particles do not feel the full charge of the neighbouring particle but rather a reduced effective charge Q_{eff} , which is given by

$$Q_{\text{eff}} = Q \exp(-r/\lambda_D), \quad (2.16)$$

where r is the distance from the center of the (partially) shielded particle.

However, for an externally applied electric field, the situation is different. Daugherty et al. have shown that the electrostatic force acting on a microparticle is given by the vacuum force (Equation 2.14) for uniform plasmas when the particle size r_p is much smaller than the Debye length [94]. They assumed the sheath around the particle to be unperturbed without trapped ions around the particle. The non-trivial conclusion reported by Daugherty et al. states that although the sheath around the particle partially shields it from the surrounding plasma, it does not screen the dust particle from an externally applied electric field.

2.4.4 Neutral drag force

Like any other object, microparticles experience a drag force when moving through a medium due to momentum transfer by collisions with neutral gas atoms or molecules. The magnitude of the neutral drag force depends on the flow regime of the surrounding gas. Two key dimensionless numbers classify the flow regime. The first one is the Reynolds number, which compares the inertial to the viscous forces and is therefore defined as

$$Re = \frac{\rho_n v_p L}{\mu_n}. \quad (2.17)$$

Here, v_p is the velocity of the microparticles with respect to the flow, L the characteristic length scale, and μ_n the dynamic viscosity of the gas. For $Re \ll 1$, the flow can be considered laminar, whereas for $Re \gg 1$ the flow is considered turbulent. The second dimensionless number that defines the flow regime is the Knudsen number, and is given by

$$Kn = \frac{\lambda_{\text{mfp}}}{L}, \quad (2.18)$$

where λ_{mfp} is the mean free path between collisions of neutral gas atoms or molecules. For $Kn \ll 1$, the flow is in the continuum regime, while for $Kn \gg 1$ it is in the free molecular flow regime.

Continuum flow regime ($Kn < 0.01$)

For a laminar flow in the continuum regime, the neutral drag force is given by the well-known Stoke's law derived in 1851 by George Gabriel Stokes [95]

$$\mathbf{F}_{\mathbf{d},\mathbf{c}} = -6\pi\mu_n r_p \mathbf{v}_p \quad (2.19)$$

Transitional flow regime ($0.01 < Kn < 1$)

For $0.01 < Kn < 1$, the flow is in the transitional regime between continuum and free molecular flow. The Cunningham slip correction takes into account the partial slip at the surface of the particle [96,97]

$$\mathbf{F}_{\mathbf{d},\mathbf{t}} = -\frac{\rho_n C_d A_p |v_p|}{2C_c} \mathbf{v}_p, \quad (2.20)$$

where A_p is the projected area of the particle and $C_c = 1 + Kn(\alpha + \beta \exp(-\gamma/Kn))$ with α , β and γ empirically determined fluid and particle dependent constants. Additionally, C_d is the drag coefficient $C_d = a_1 + a_2/Re + a_3/Re^2$ with the constants a_1 , a_2 and a_3 . For $Re < 0.1$, Equation 2.20 reduces to $\mathbf{F}_{\mathbf{d},\mathbf{t}} = \mathbf{F}_{\mathbf{d},\mathbf{c}}/C_c$.

Free molecular flow regime ($Kn > 1$)

In the free molecular flow regime, $Kn \gg 1$, the Epstein relation describes the neutral drag

$$\mathbf{F}_{\mathbf{d},\mathbf{f}} = -\frac{4\pi}{3}\delta\rho_n r_p^2 v_{\text{th},n} \mathbf{v}_p, \quad (2.21)$$

for $v_p \ll v_{\text{th},n}$, where $v_{\text{th},n}$ is the thermal velocity of the gas atoms or molecules. In addition, δ is a constant accounting for the microscopic mechanism of the collisions between the particles and the gas atoms or molecules. For perfect specular reflections $\delta = 1$, whereas for diffuse reflections $\delta = 1.442$ for a thermal non-conducting particle [98].

2.4.5 Ion drag force

Ions with a directed velocity can also transfer momentum to the charged microparticles. This effect is, for example, prominent near the edges of the plasma discharge, where positive ions are accelerated in the electric field of the sheath. In contrast to the neutral drag force, the ion drag force is not only determined by the geometrical cross-section, but also by the Coulomb interaction between the charged microparticles and the ions, which significantly enlarges the cross-section as compared to the geometrical cross-section.

There are two different approaches to describe the ion drag force based on the ion collisionality. The first one is the Binary Collision (BC) formalism that solves the ion motion in the field induced by the charged particle. Consequently, the BC formalism is a ballistic approach, which can only be applied for ions that do not collide with background atoms or molecules. The key choice to make in the BC formalism is the ion-particle interaction strength for which several models exist in the literature [16, 99–101].

In the second approach, the linear plasma response formalism, ion-neutral collisions are taken into account self-consistently by calculation of the anisotropic electric field around the particle which induces the ion drag [102, 103]. This approach can only account for weak ion-particle coupling.

Here, for the purpose of providing an overview, the collisionless ion drag relation is given for the most common interaction potential, the Debye-Hückel potential (or Yukawa potential), which is in essence a screened Coulomb potential similar to the previously introduced effective charge (Equation 2.16). For the screening length of the Debye-Hückel potential, the linearised Debye length is assumed (Equation 2.4) [104]. The collisionless ion drag force consists of two components: the first component is caused by direct impact collisions, the second by Coulomb scattering of the ions in the field of the particle. The total ion drag force can be expressed as [69, 99]

$$\mathbf{F}_i = m_i n_i v_{i,\text{eff}} u_i \left[\pi \rho_c^2 + 4\pi \rho_0^2 \ln(\Lambda) \right]. \quad (2.22)$$

Here, $\rho_{c,0}$ is the impact parameter where $\pi \rho_c^2$ accounts for the direct impact collisions and $4\pi \rho_0^2 \ln(\Lambda)$ for the Coulomb scattering contribution. The maximum impact parameter at which ions are collected by the grain is given by

$$\rho_c = r_p \sqrt{1 + 2\rho_0/r_p}, \quad (2.23)$$

where $\rho_0 = Ze^2/mv_{i,\text{eff}}$ with Z the grain charge number and $v_{i,\text{eff}}$ the effective ion velocity

$$v_{i,\text{eff}} = \sqrt{u_i^2 + v_{\text{th},i}^2}. \quad (2.24)$$

In the latter, u_i is the directed or drift ion velocity and $v_{\text{th},i}$ the thermal ion velocity. The Coulomb scattering contribution is defined by the so-called Coulomb logarithm given by

$$\ln(\Lambda) = \ln \left[\frac{(\rho_0^2 + \rho_{\text{max}}^2)}{(\rho_0^2 + \rho_{\text{min}}^2)} \right]^{1/2}. \quad (2.25)$$

Here, ρ_{min} and ρ_{max} are the minimum and maximum impact parameters for the Coulomb interaction. For standard Coulomb scattering, $\rho_{\text{min}} = \rho_c$ and $\rho_{\text{max}} = \lambda_D$ [105], while it may be adapted based on the ion-particle interaction strength modelled, as explained at the outset of this section.

2.4.6 Thermophoretic force

A third drag force possibly acting on an airborne particle is the thermophoretic force, which is created due to the difference in momentum transfer by atoms or molecules in a

surrounding where a temperature gradient is present. The warmer gas species transfer more momentum than the colder species and, therefore, the particle experiences a net force in the direction opposing the temperature gradient. Similar to the previously discussed neutral and ion drag, the thermophoretic force strongly depends on the collisionality regime. In the continuum regime ($Kn \ll 1$), the thermophoretic force is given by [106]

$$\mathbf{F}_{\text{th,c}} = -\frac{9\pi r_p \kappa_g}{2\kappa_g + \kappa_p} \frac{\mu^2}{\rho_n T_n} \vec{\nabla} T_n \quad (2.26)$$

with κ_g and κ_p the thermal conductivity of the gas and the particle respectively and μ the coefficient of shear viscosity. In the free molecular flow regime ($Kn \gg 1$), the following equation describes the thermophoretic force [107]

$$\mathbf{F}_{\text{th,f}} = -\frac{32}{15} \frac{r_p^2}{v_{th,n}} \left[1 + \frac{5\pi}{32} (1 - \alpha) \right] \kappa_g \vec{\nabla} T_n. \quad (2.27)$$

Here, α is an accommodation coefficient which is assumed to be approximately equal to one, when the dust and particle temperatures are below 500 K [107]. The reader is referred to the literature for the thermophoretic force in the transition regime between the continuum and the free molecular flow regime [107–110].

2.4.7 Radiation pressure force

Photons colliding with particles impart a radiation pressure force. In contrast to astrophysical plasmas, the radiation pressure force caused by the plasma emitted light is negligible in magnitude in laboratory situations. Instead, photons from a laser predominantly impart a radiation pressure force on the microparticles, which is described by [111]

$$\mathbf{F}_{\text{rad}} = \frac{qn_1\pi r_p^2 I_{\text{laser}}}{c}, \quad (2.28)$$

where n_1 is the refractive index of the medium surrounding the particle, c the speed of light, I_{laser} the laser intensity and q a dimensionless factor. The latter parameter is determined by the absorption, reflection and transmission of the photons irradiating the particle surface [111].

2.4.8 Comparison of magnitude of forces

The forces described above strongly depend on the (plasma) parameters. Yet, it is insightful to compare the magnitude of these forces for different particle sizes, while keeping all other parameters constant. In Figure 2.2, these forces are plotted as a function of size where the following assumptions have been made for a typical spatial plasma afterglow situation. First, the electron and ion density are assumed to be $n_e = n_i = 10^{12} \text{ m}^{-3}$. In addition, the electrons, ions and neutrals are taken to be at room temperature $T_{e,i,n} = 293 \text{ K}$. The argon pressure is $p = 90 \text{ Pa}$ with an externally applied electric field of 5 kV m^{-1} . Moreover, a temperature gradient of $(dT_n/dx) = 1 \text{ K m}^{-1}$ in the horizontal direction and a laser intensity of $I_{\text{laser}} = 2 \times 10^3 \text{ W m}^{-2}$ are

assumed. Finally, the mass density of the particles is assumed to be $1.57 \times 10^3 \text{ kg m}^{-3}$ (which is the average density of the particles used in the experiments, see chapter 3) and the charge of the particles to be $Q = -10e$.

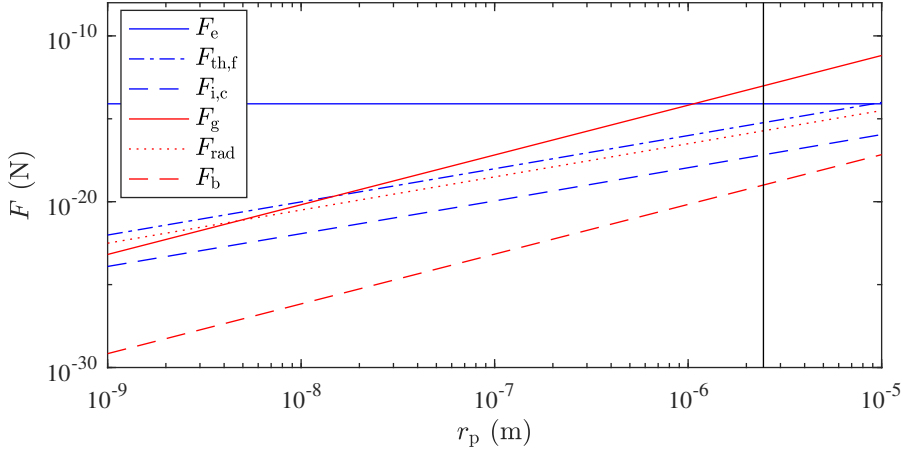


Figure 2.2: Comparison of the magnitude of the forces acting on the microparticles in a typical spatial plasma afterglow. Indicated in blue are the forces acting in the horizontal directions, and indicated in red the forces in the vertical direction. A vertical line is added to indicate the size of the particles used in the experiments described in this thesis.

In Figure 2.2, the relation for thermophoretic force in the free molecular flow regime is plotted since $Kn_{r_p} > 1$ for the specified argon pressure. For the ion drag, a collisional relation based on [102] is plotted since ion-argon collisions are taking place in the vicinity of the particles for the given experimental conditions. Note that in the afterglow void of any physical objects, the vertical electric field component is generally negligible. Figure 2.2 shows that in the horizontal direction, the electric force is dominant for the size of particles used in the experiments described in this thesis. In the vertical direction, gravity is dominant.

2.5 Flow

This section describes the flow theory relevant to the understanding of the experiments described in this thesis.

2.5.1 Entrance effects

When gas is injected into a duct of arbitrary size, the gas flow can be turbulent at the start due to high local flow velocities and therefore, a high Reynolds number (as described in subsection 2.4.4). It takes a certain distance L_e for the gas flow to develop its typical flow profile. Initially, when the gas is injected, only a thin shear layer is

present. Within the entrance length L_e , the shear layer grows until the flow profile is fully developed. It has been empirically shown that for a laminar flow, regardless of the duct shape, L_e is given by [112]

$$L_e = D [C_1 + C_2 Re_D], \quad (2.29)$$

where $C_1 \approx 0.5$, $C_2 \approx 0.05$ and D the typical width of the duct (most often its diameter). For distances larger than L_e from the gas injection point, the flow is considered fully developed. The velocity is then directed purely axially (in the x direction) and varies only with the lateral coordinates (y and z).

2.5.2 Flow profile

The flow profile of an incompressible Newtonian fluid that is fully developed is described by the Poisson equation [113]

$$\frac{\partial^2 u}{\partial y^2} + \frac{\partial^2 u}{\partial z^2} = \frac{1}{\mu_n} \frac{dp}{dx} = \text{const.} \quad (2.30)$$

Here, p is the pressure and u the flow velocity in the x direction, where x is the axial coordinate and y and z are the lateral coordinates as indicated in Figure 2.3.

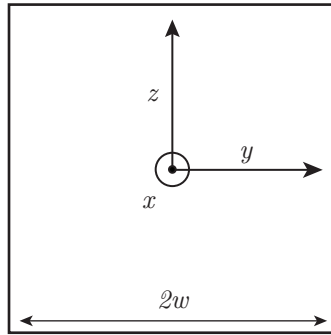


Figure 2.3: Cross-sectional view of a square tube indicating the axial coordinate x and the lateral coordinates y and z .

In the experiments described in this thesis, a square glass tube is used (as will be described in more detail in chapter 3 section 3.2) and therefore, the solution of the Poisson equation is given for a square duct of width $2w$ [113]

$$u_s(y, z) = \frac{16w^2}{\mu_n \pi^3} \left(-\frac{dp}{dx} \right) \sum_{i=1,3,5,\dots}^{\infty} (-1)^{(i-1)/2} \left[1 - \frac{\cosh(i\pi z/2w)}{\cosh(i\pi/2)} \right] \frac{\cos(i\pi y/2w)}{i^3}, \quad (2.31)$$

where $-w \leq y \leq w$ and $-w \leq y \leq w$. By integrating Equation 2.31 over the cross-section of the duct, the volume flow Q_s is obtained

$$Q_s = \frac{4w^4}{3\mu_n} \left(-\frac{dp}{dx} \right) \left[1 - \frac{192}{\pi^5} \sum_{i=1,3,5,\dots}^{\infty} \frac{\tanh(i\pi/2)}{i^5} \right]. \quad (2.32)$$

The discussed flow properties are taken into account in the design of the experimental setup and the measurements therein as discussed in chapter 3.

From experiments to charge

Abstract

This chapter introduces the designed setup and the in-house developed particle tracking software. Using this setup, the particle charge in a free spatial plasma afterglow is investigated and presented as “proof of principle measurements”. Under the conditions described in this work, the particle charge in this afterglow region is shown to be three orders of magnitude lower than the typical charge expected in the plasma bulk, which is explained by a relatively simple analytical model.

Part of this chapter is published as:

B. van Minderhout, A.T.A. Peijnenburg, P. Blom, J.M. Vogels, G.M.W. Kroesen and J. Beckers (2019), “The charge of micro-particles in a low pressure spatial plasma afterglow” *Journal of Physics D: Applied Physics* **52** 32LT03

3.1 Introduction

This chapter discusses the process of measuring the charge of microparticles in the spatial plasma afterglow (SPA). It covers the hardware of the setup and the data post-processing. Finally, to demonstrate proof of principle, first measurements are presented for the free SPA case. To describe the experimental setup, we will follow one of the microparticles moving through it and explain the different phases this particle “encounters”. This viewpoint is often called the Münchhausen perspective, named after Karl Friedrich Hieronymus von Münchhausen. As the myth goes, this German baron from the 18th century rode on a cannonball to reach the neighbouring city in times of war [114].

In section 3.3, the experimental setup and its main diagnostic are discussed, followed by the essence of the in-house developed particle tracking software in section 3.3. Section 3.4 discusses the proof of principle particle charge measurements. This chapter is finalised with a conclusion in section 3.5.

3.2 The setup and its main diagnostic

In this section, the designed and developed Plasma Particle Charging Investigation (PPCI) setup is introduced. All experiments described in this thesis have been performed in the PPCI setup. First, an overview of the setup is given, briefly discussing the main elements. After this bird’s eye view, we use the Münchhausen perspective and follow a microparticle on its journey from the top of the setup to its bottom.

The PPCI setup was a vacuum system with a base pressure of roughly 5×10^{-9} Pa. The eye-catching element was a 1 m long glass tube with a square (inner size 0.1 m x 0.1 m) cross-sectional shape. A sketch of it is shown in Figure 3.1. The top of the setup consisted of a stainless steel showerhead through which gas and particles were injected. This showerhead was directly mounted to the top of the glass tube. The square-shaped glass duct was chosen to increase the accuracy of the charge measurements and to optimise the analysis. Once injected, microparticles fell through an Inductively Coupled Plasma (ICP) which was generated using a square coil wound around the tube. In the SPA downstream of this plasma, the charge of the particles was obtained by measuring their acceleration in an electric field, externally applied using two Rogowski electrodes [115]. During their travel, the particles were illuminated with a laser system and their scattered light was recorded by a high-speed camera.

In the following sections, we switch to the Münchhausen perspective and look at the setup in more detail moving from the top to its bottom. Each of the following subsections is dedicated to one of the components of the PPCI setup.

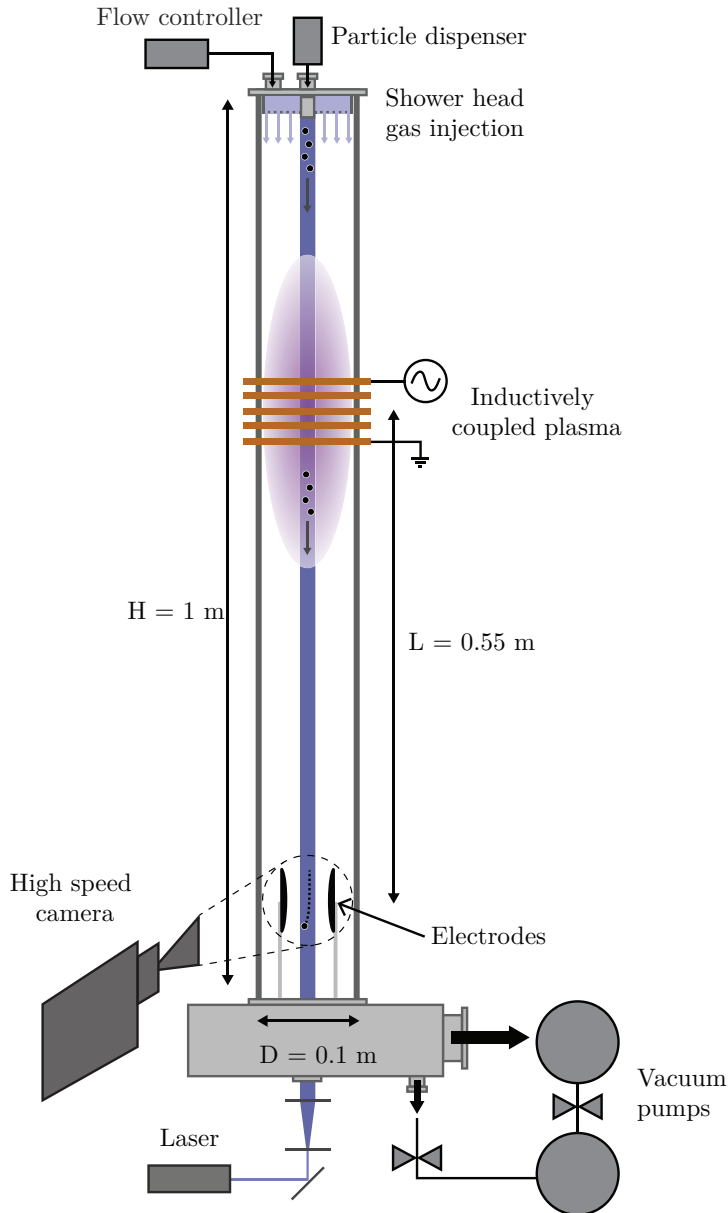


Figure 3.1: Schematic illustration of the designed and developed Plasma Particle Charging Investigation (PPCI) setup in which (from the top to the bottom) microparticles travel through a spatially limited region of plasma, after which their charge is measured by accelerating these particles in an externally applied electric field.

3.2.1 Microparticles

In the next sections, we follow a microparticle created in the factory of microParticles GmbH. The core of the particle consists of a polymer called melamine-formaldehyde (MF). The particle's outer layer is a stable porous silver layer of several hundred nanometres, making it resemble a rough orange, as shown in Figure 3.2. The silver coating minimised clustering of the particles by reducing the triboelectric charging as compared to non-conducting particles, as explained in the next section. In total, the particle diameter was $4.9 \pm 0.2 \mu\text{m}$, where the outermost layer consisted most likely of a stable silver oxide [116].

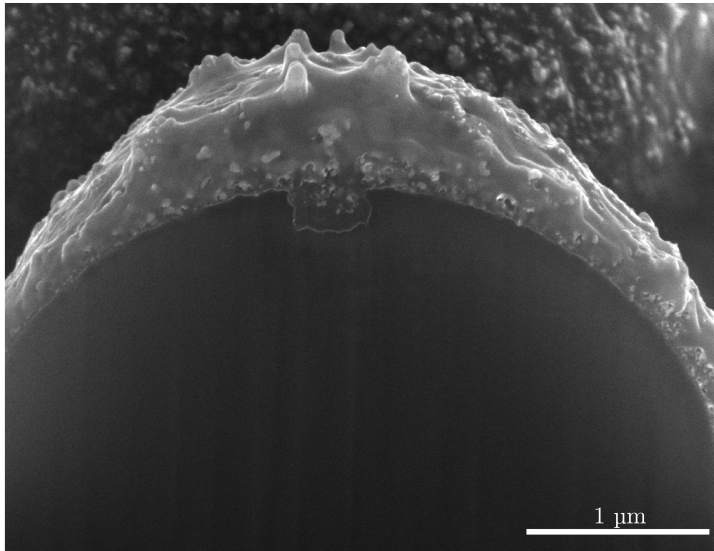


Figure 3.2: SEM image of the cross-section of a single silver coated melamine-formaldehyde microparticle. The cross-section is obtained by cutting the microparticle with a gallium Focused Ion Beam (FIB).

3.2.2 Particle dispenser

Figure 3.3 schematically depicts the particle dispenser of the PPCI setup. Its design is similar to the particle injectors used in earlier studies [117, 118]. The particles were placed in the container of the dispenser that had a $50 \mu\text{m}$ hole in its bottom. Its top was attached to a rod connected to an iron core which, in turn, was kept in place by a spring (indicated in green). The rod was centred by an isolating plastic plate, which gave the container a floating potential. Surrounding the iron core (indicated in

blue) was an electromagnet (indicated in red). When this magnet was powered and depowered by switching a current on and off through the coil, the iron core - and thus the container - moved axially, i.e. vertically. During these movements, some particles fell through the hole in the bottom of the container and were injected into the setup.

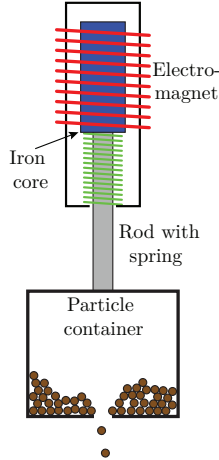


Figure 3.3: Schematics of the particle dispenser. Adapted from [66].

A consequence of using this method of injection was that during the movement of the container, the particles bounced back and forth, hitting other particles and, occasionally, the container's walls. This process caused the outer shell of the particles to become electrically charged, governed by the triboelectric effect, as explained in subsection 2.3.1. The particles could have equally well been charged positively or negatively, since the sum of the charge of all particles and the container's walls was preserved (assuming the container to be at a floating potential). Consequently, particles may stick together and form a clustered microparticle. The charging physics of these kinds of clusters will be treated in chapter 6. In the remainder of the current chapter, we will follow a single (non-clustered) microparticle.

3.2.3 Laser light scattering

After leaving the dispenser, the particle was illuminated by a diode laser sheet with a wavelength of 447 ± 8 nm. In order to create this laser sheet, the laser beam had to pass collimation optics, i.e. a negative and positive cylinder lens respectively. It subsequently entered the setup at the bottom through a Brewster window, minimising the reflection losses. The laser sheet was 3 mm thick and 40 mm wide and was oriented antiparallel to the velocity of the particles, i.e. vertically (see Figure 3.1). Therefore, this laser sheet illuminated the particles throughout the entire setup.

3.2.4 Showerhead

Straight after leaving the particle dispenser, the particle entered the showerhead. In this part of the setup, the flow was distributed evenly over the cross-section of the tube. An inventor image of the showerhead is shown in Figure 3.4. As the particle moved downwards, the circular tube in which the particle had been injected changed gradually to a rounded rectangular tube which was 5 mm thick and 40 mm wide. First, this shape ensured that the particles were injected in a volume roughly matching the cross-sectional dimensions of the laser sheet. Second, the size and the shape of the injection channel made it an ideal beam dump for the laser by preventing unwanted laser reflections that would have obscured the data analysis.

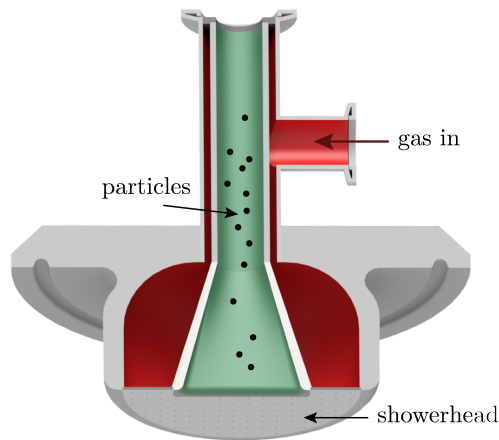


Figure 3.4: Cross-sectional view of the showerhead, i.e. the gas and particle injection system. The flow path is indicated in red, the path through which the particles travelled in green.

All around the particles, argon gas was injected through 200 holes of 0.5 mm in diameter. These holes were distributed equally around the injection slit and aimed to limit the flow entrance effects (see section 2.5). The argon gas flowing through the holes was regulated by a Brooks SLA850 mass flow controller (MFC). The particles were fully entrained in the flow after leaving the showerhead.

For the purpose of generating a homogeneous plasma (as explained in subsection 3.2.5), the showerhead contained no sharp edges, so that possible local field enhancements were minimised. This effect of field enhancement is known to sailors as St. Elmo's fire [119]. During thunderstorms, the electric field present is enhanced around sharp objects (such as the masts), which may create corona discharges. After the showerhead, we continue our travel downwards into the glass tube, where the plasma was generated.

3.2.5 Plasma source

After leaving the showerhead, the particle was accelerated vertically and antiparallel to the laser sheet due to gravity and the top-to-bottom argon flow. Naturally, a force opposing this acceleration also existed, because much lighter argon atoms collided with the particle. After a certain distance, gravity and the opposing so-called neutral drag force eventually balanced, giving the particle a constant settling velocity.

Moving downwards, the particle travelled in the middle of a five-turn square coil wound around the tube. At that moment, the particle had moved into the active plasma region. Besides laser light, it was illuminated by a series of different wavelengths emitted by the decaying excited atoms in the plasma. More importantly, electrons and ions collided with the particle surface, charging it negatively. The governing theory for this plasma-charging is elaborated upon in section 2.3.

The active plasma region in which the particle resided was created by sending a radiofrequency (RF) alternating current at 13.56 MHz through the coils. The RF signal was generated by an Agilent 33220A function generator, amplified by an E&I AB250 power amplifier, and matched with a T-matching circuit to convert the complex plasma impedance at 13.56 MHz to a $50\ \Omega$ resistive load seen by the amplifier. In subsection 2.2.2, the working principles of an Inductively Coupled Plasma (ICP) are explained.

Leaving the active plasma region, the plasma column became thinner because the plasma was also partially capacitively coupled with the top and the bottom of the setup. Chapter 4 and chapter 5 will elaborate upon a mesh grid placed in the setup about 0.2 m below the coil, which, except for shielding the SPA from the bulk, also enhances the capacitive coupling. No mesh grid was installed in the experiments described in this chapter.

At this point the particle was in the SPA. This region is unique because the evolution of plasma properties surrounding the particle, such as the density and the temperature of the plasma species, is far from understood.

3.2.6 Rogowski electrodes

The SPA region changes the particle charge. This very property constitutes the core research subject of this thesis. In the SPA, a DC electric field was generated using two vertically aligned Rogowski shaped electrodes [115]. The electric field accelerated the particle in the horizontal direction, i.e. perpendicular to the settling velocity vector. The curved shape of these Rogowski electrodes suppressed the field enhancement near their edges. This resulted in an increased maximum electric field that, when compared to parallel plate electrodes, could be applied without creating a DC glow discharge. The diameter of these parallel electrodes was 70 mm with a horizontal separation distance of 40 mm.

Knowledge of the electric field is important to obtain the particle charge from the measured acceleration. For this reason, a 2D electrostatic model was set up using COMSOL® [120]. The simulated electric field profile is shown in Figure 3.5. In the experiments described in this chapter and in chapter 4, the particles were detected in the central region between the electrodes spread over 5×40 mm and

20 x 30 mm respectively. For the purpose of analysis, the electric field was assumed to be homogeneous in this region (local variations in electric field were approximately 30% and 15% in the case of the experiments discussed in this chapter and chapter 4 respectively). In the experiments reported in chapter 5, the local electric field for each part of the particle trajectories will be taken into account (as will be elaborated upon in the methods section of chapter 5). In the analysis of chapter 6, the variations in the local electric field are corrected for by calculation of the trajectory-averaged electric field.

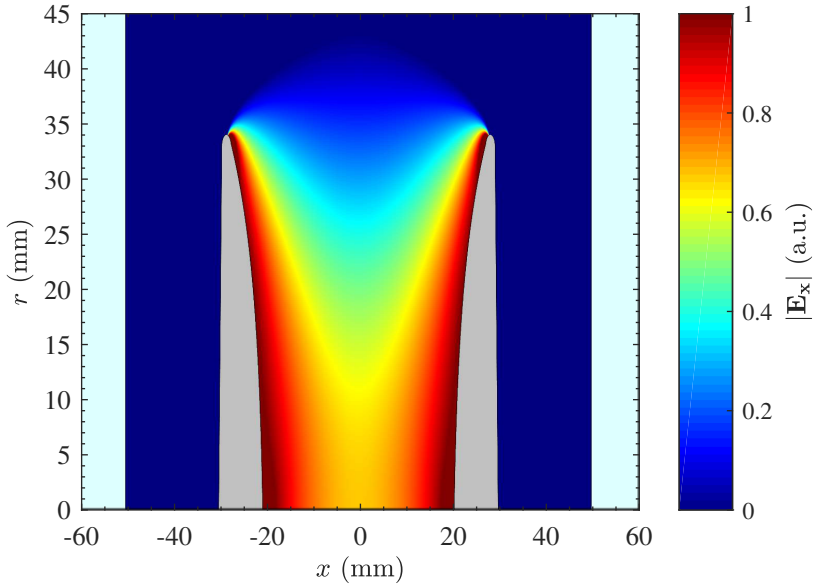


Figure 3.5: Normalised horizontal component of the electric field created between the Rogowski electrodes. The electrodes are indicated in grey and the glass tube in light blue. Cylindrical geometry was used (the x-axis is the axis of symmetry), which implies that the front and back glass plates of the tube were not taken into account in the simulation.

3.2.7 High-speed camera

The laser light scattered by the microparticles was imaged by a high-speed camera (Photron Fastcam mini UX100), where its viewing direction was perpendicular to the plane of the laser sheet (see Figure 3.1). The small thickness of this laser sheet assured that particles moving towards or away from the camera, i.e. particles moving parallel to the viewing direction of the camera, were not imaged over their full trajectory. Consequently, particles that moved out of the laser sheet were omitted in the subsequent post-processing (as explained in section 3.3). In Figure 3.6, five typical particle trajectories are shown: 54 frames were plotted together, with each frame coloured alternately red, blue and green to visualise the trajectories of the particles.

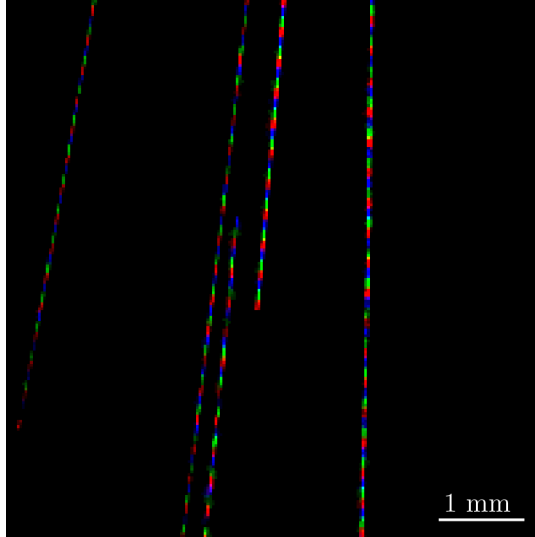


Figure 3.6: Raw image of five particles moving through the region of the applied electric field. 54 frames were subsequently coloured red, green and blue indicating the movement of the particles. The video was recorded in gray scale at 1000 fps.

The high-speed camera used for the imaging of the particle trajectories could measure up to 800 000 frames per second (fps) at a limited resolution and up to 4000 fps at a full resolution of 1280 x 1024 pixels. At the latter resolution, 8300 frames could be recorded using the installed 16 GB of memory, which results in a recording time of 2.08 s for the given frame rate. To synchronise the camera and the position of the particles, the camera was triggered by a TTL pulse, which is generated upon particle injection. This TTL pulse could be delayed by a BNC pulse generator 577-4C according to the experimental needs.

The particles appeared larger on the recorded images than their actual size as the optics were deliberately defocus. In this manner, it was easier to detect the particles since their size was smaller than the typical image length per pixel at the focal point. In more detail, the field of view was approximately 40 x 32 mm. Accordingly, 1 pixel corresponded to approximately 32 μm , which was much larger than the particle diameter. Therefore, the recorded image could not be used to measure the particle size. Yet, by defocusing the optics, the particle position could be determined more accurately (i.e. subpixel accuracy was achieved). This statement will be elaborated upon in section 3.3 discussing the particle tracking software. Finally, by taking photos of a 2 x 2 mm chequerboard, it was verified that aberrations did not distort the image.

3.2.8 Charge measurement

Having introduced all the elements of the PPCI setup, we can combine the parts of the setup described in subsection 3.2.6 and subsection 3.2.7 to form the main

diagnostic of this thesis: the particle charge measurements. Pivotal to the charge measurement is the horizontal acceleration, which the residually charged particles experience from the externally applied electric field. Once the temporal evolution of the horizontal component x of the particle trajectory is found, the horizontal acceleration d^2x/dt^2 can be retrieved. Considering that this acceleration is caused by the electric field E working on the particle charge Q , Newton's second law can be used to find the charge of the particles with mass m as $Q = [m/E(x)] [d^2x/dt^2]$. In the preceding, ion drag and plasma shielding are assumed to be negligible. The strength of this measurement technique is that the separate charge of multiple particles can be measured simultaneously on the condition that all particles are within the imaging region and do not mutually interact. The manner in which the temporal evolution of the horizontal particle trajectory component is obtained from the raw images, will be the subject of the next section.

3.3 Particle tracking

This section discusses the in-house developed particle tracking software. This means that from this point onwards the Münchhausen perspective will no longer be used. The particle tracking software consists of three parts, which will be treated in the next three subsections.

- **Particle detection**

In this part of the software, the particle positions were obtained from each frame of the recorded video.

- **Particle linking**

In the second part, the individual detected particle positions were linked and particle trajectories were composed by combining them.

- **Trajectory analysis**

In part three, the particle trajectories were fitted and their horizontal acceleration was obtained, amongst other parameters,.

3.3.1 Particle detection

The goal of the first part of the software was to determine the positions of all imaged particles in each frame. Therefore, a mask was created that indicated the regions in each frame where particles were detected by using a series of morphological operations. The exact location of each particle was determined by calculation of its intensity weighted midpoint. Here, it was important that each particle detection consisted of multiple pixels, which was experimentally achieved by deliberately placing the optics slightly out of focus (see subsection 3.2.7). In this way, the particle positions were, in each frame, determined with a subpixel accuracy of about $5\ \mu\text{m}$.

What follows here is a more detailed description of the 3-step process of the mask generation. The basis of this part of the code was created by L. Heijmans [66, 118] and further developed for our purposes. First, the recorded background frame was

subtracted. Second, the 12-bit grayscale images were processed using a 2D bandpass filter that suppressed pixel noise and slow-scale image variations, while information of the characteristic detection size was retained. Third, the frame was converted to a black and white image, after which a series of morphological operations (such as the removal of small areas from the image and the calculation of the image convex hull) was performed. In this way, noise can be filtered out, and all particle detection regions are made convex. Finally, the midpoint of each particle detection region was obtained, which was the input for the second part of the software.

3.3.2 Particle linking

In the second part, these individual particle positions were linked from frame to frame to create trajectories. For each particle detected at the top of a frame, a new trajectory was started. For all other particle positions, the cost (the difference between the measured and expected particle position, as explained below) was calculated to assign each individual particle detection to one existing trajectory. Thereby, a cost matrix was created and subsequently solved by finding the lowest total linking cost. Therefore, all positions in one frame were simultaneously assigned to the existing trajectories or new trajectories were started.

To describe this linking process in more detail, let us look at the first three frames of a video. In the first frame, the N positions were all taken to be the start of a new trajectory. Then, in the second frame, the Euclidean distance between the positions in the first frame and the new positions was calculated. Suppose we had M positions in the second frame. This gave a $M \times N$ cost matrix which was solved using the Hungarian assignment algorithm [121].

Additionally, this approach determined which positions formed the start of new trajectories beginning in the second frame. Using the two positions of each trajectory in frame 1 and 2, a prediction was made of the location in frame 3 using a Kalman filter, which outputted the velocity vector of the trajectory. This vector was used as the basis for the calculation of the linking cost. To calculate the linking cost, in contrast to the second frame, a non-Euclidean cost function was used, inspired by the work of Bekkers et al. [122]. Deviations perpendicular to the Kalman velocity vector were weighted more heavily than deviations parallel to the velocity vector. The procedure described for the third frame is then repeated for all remaining frames, thereby forming trajectories from the detected particle positions.

3.3.3 Trajectory analysis

The goal of the third part of the software was to obtain the horizontal acceleration of the trajectories. This acceleration is one of the key parameters to determine the charge of the microparticles, as will be explained in more detail in subsection 3.2.8. To this end, the trajectories were quadratically fitted and amongst other parameters, their horizontal velocity and acceleration (anti)-parallel to the externally applied electric field were obtained. In this manner, the determined velocity formed the initial velocity at the start of the field of view and the acceleration was the change in velocity within this region.

In the analysis, no filtering was applied to obtain the relevant data, for example, no criteria were imposed on the goodness of fit. The length of the trajectories was the only selection criterium that was used, meaning that trajectories shorter than a specific length were left out of the analysis. This selection removed trajectories that remained in the laser sheet for only a short time (see subsection 3.2.3).

3.4 Proof of principle

This section presents the charge measurement of microparticles in the SPA of the PPCI setup. It concerns the residual charge in the free SPA, i.e. without a grid between the coil and the Rogowski electrodes. The relevant data serve as a proof of principle for the introduced setup and the charge measurement diagnostic.

First, subsection 3.4.1 discusses the experimental parameters as well as the reheating of electrons in the SPA. Second, subsection 3.4.2 presents the accuracy of the charge measurements. Then, in subsection 3.4.3, the measured charge distribution is discussed, followed by the introduction of an analytical time scale model in subsection 3.4.4 explaining the respective results. Finally, subsection 3.4.5 compares the charge measurements to the model predicted charge.

3.4.1 Experimental parameters and reheating of electrons

The experiments described below were performed in argon with a background pressure of $p = 90$ Pa. From the top of the setup, a 50 sccm flow was injected which, together with gravity and the balancing of the neutral drag, resulted in a measured settling velocity of the microparticles of $v_{p,f} = 0.36$ m s⁻¹. This velocity was reached before particles entered the active plasma region. Additionally, the flow ensured stable plasma conditions. About 15 W of power was inductively coupled into the plasma. After passing through the plasma, the charge was measured by applying a DC electric field of 4.3 kV m⁻¹ to the electrodes.

As will be shown in the next sections, the electron temperature is a key parameter for the charge of the particles in the SPA. To verify that electron heating due to the remote electric RF fields from the ICP at the position of measurements remained small, we estimated the maximum field strength using the Biot-Savart law and the fourth law of Maxwell. Furthermore, the RF current going through the coil to generate the ICP was measured using the Octiv Poly VI probe produced by Impedans Ltd. In this way, the electric field was estimated to be $E_{RF} = 0.1$ V m⁻¹. This was indeed negligible with respect to the externally applied electric field of $E_{DC} = 4.3$ kV m⁻¹ and, hence, heating of electrons by the RF field in the SPA was expected to be negligible.

3.4.2 Accuracy of charge measurements

To verify that measurement errors such as lens aberrations and particle detection mistakes remained extremely small, we plotted the horizontal acceleration distribution from 148 trajectories in Figure 3.7a in the absence of flow. The particles travelled through a stationary argon gas in the absence of plasma and externally applied electric

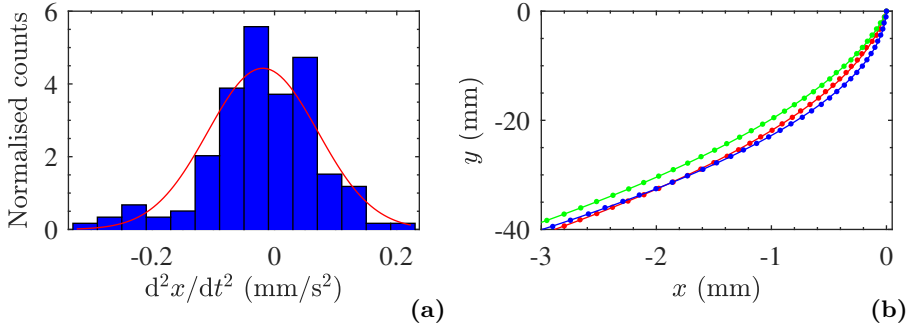


Figure 3.7: a) Histogram of the horizontal acceleration distribution for the situation without plasma, a stationary background gas and in the absence of an externally applied electric field. b) Three typical particle trajectories together with a quadratic fit in the region of externally applied electric field after passing the ICP. Every tenth data point is plotted for clarity; in addition to the starting point of each trajectory being transformed to the origin.

field. The mean ($3 \times 10^{-5} \text{ m s}^{-2}$) and standard deviation ($1 \times 10^{-4} \text{ m s}^{-2}$) of the distributions in Figure 3.7a show that the measurement errors were indeed small. It can be concluded that the mutual Coulomb interaction between particles due to their triboelectric charge was negligible. Particles do not repel or attract each other because of their low concentration and, hence, their large separation distance.

Figure 3.7b shows three typical particle trajectories travelling in the region of the externally applied electric field (after they have passed the ICP) together with a quadratic fit for each trajectory. These fits clearly overlap with the data points. From this, it was concluded that no significant neutral drag existed that acted on the microparticles in the horizontal direction obscuring our measurements. Note that the neutral drag scales with horizontal particle velocity $v_{p,x}$ and would, therefore, lower the net force on the particles as they accelerated in the electric field.

3.4.3 Charge distribution

Figure 3.8 shows the particle charge measurement in the form of two horizontal acceleration distributions. The distribution in blue shows the horizontal acceleration of the particles after passing the plasma discharge with a 50 sccm flow in the absence of the externally applied electric field. The mean ($a_f = -1.2 \times 10^{-2} \text{ m s}^{-2}$) and standard deviation ($\sigma_f = 2.0 \times 10^{-2} \text{ m s}^{-2}$) proved significantly larger than those in Figure 3.7a. We believe that flow disturbances around the electrodes caused the acceleration distribution to broaden with respect to the distribution in Figure 3.7a. The red distribution shows the measured acceleration, with a mean value of $a_p = -2.1 \times 10^{-1} \text{ m s}^{-2}$, for the situation where the electric field was switched on, while all other parameters were identical to those for the blue distribution. The clear shift between the two acceleration distributions in Figure 3.8 allowed the particle charge $Q = -30 \pm 7 e$ to be obtained.

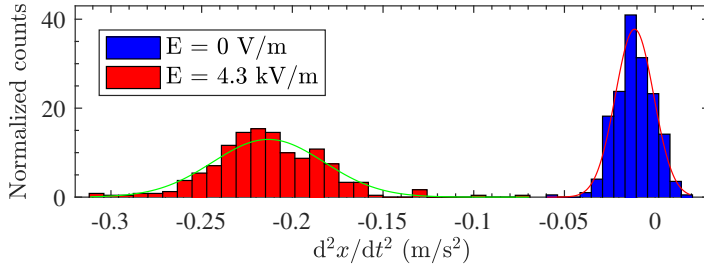


Figure 3.8: Particle charge measurement in the form of two acceleration distributions. The distribution in blue is composed of 319 particles that traveled through the SPA in the absence of externally applied electric field, whereas the distribution in red is composed of 297 particles that were subject to an electric field of $E = 4.3 \text{ kV m}^{-1}$.

The standard deviation of the red distribution in Figure 3.8 ($\sigma_p = 4.4 \times 10^{-2} \text{ m s}^{-2}$) was approximately a factor two larger than σ_f due to two reasons. First, the particles had a spread in Q/m because variations in size lead to variations in charge [123] and mass, each scaling differently with size. Second, purely monodisperse particles also have a spread in charge due to the stochastic nature of the plasma charging currents arriving at the particle surface, especially important for these low values of the particle charge in the SPA. For monodisperse particles, Khrapak et al. [124] showed that the coefficient $\delta = \sigma_Q/\sqrt{|Q|} = (0.46 - 0.50)$ for $T_e = (1 - 20) T_i$ (with T_e and T_i the electron- and ion temperature). For our measurements, $\delta \approx 1.3$, which was significantly higher than this theoretical value, from which we concluded that the dominant cause of this difference was due to the spread in the mass of our particles.

Figure 3.9 shows, as main result, the measured particle charge distribution, assuming σ_f to be zero. This charge distribution was obtained by correcting for the average acceleration measured without an electric field a_f and calculating the charge using Newton's second law using the supplier-provided particle mass of $m_p = 9 \times 10^{-14} \text{ kg}$.

3.4.4 Decharging model

The particle charge we measured was about three orders of magnitude lower than the charge that would be expected in the plasma core [123] but proved, however, still significant. To explain this charge, we proposed a simple analytical model describing the decharging of microparticles travelling through an ICP, consecutively followed by its SPA. Where in previous works such models had been used to analyse particle decharging in temporal plasma afterglows [52, 53, 56], our model extended the general thought and applied it to a SPA. In this approach, we neglected the influence of ion-neutral collisions. The developed model consisted of three typical timescales: the plasma-particle interaction timescale τ_{pp} , the particle charging timescale τ_Z and the electron temperature relaxation timescale τ_{T_e} . The following section is structured as follows. After introducing the timescales, we describe how the electron temperature T_e is estimated and the particle charge in the SPA is obtained.

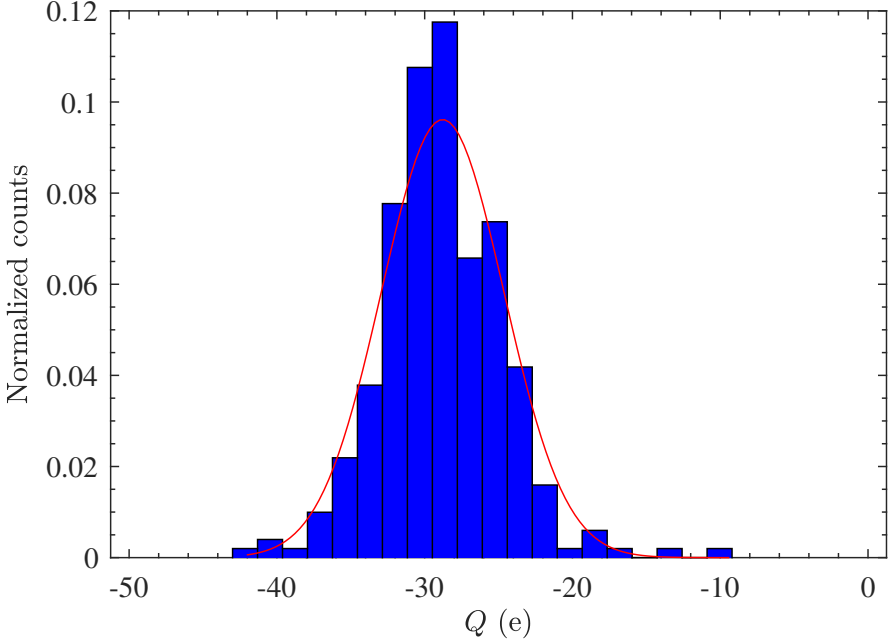


Figure 3.9: The measured particle charge distribution composed of 297 particles.

The plasma-particle interaction time τ_{pp} described the typical time a particle resided within a plasma region with constant plasma-parameters and was defined by

$$\tau_{pp} = \frac{\lambda_D}{v_{p,f}} \equiv \frac{\tau_{pp,0}}{\sqrt{\tilde{n}}}. \quad (3.1)$$

Here, λ_D was the (linearised) Debye length, the smallest length scale over which plasma parameters could be considered constant, and $\tilde{n} = n_{e,i}/n_{e,0}$ the dimensionless plasma density, where $n_{e,0}$ was the initial plasma density at the position of the coils, hereafter called the plasma core.

The particle charging timescale τ_Z represented the time needed for particles to reach their plasma-induced equilibrium charge and was defined by [125]

$$\tau_Z = \frac{\lambda_{D_{i0}}^2}{v_{T_i} a} \frac{1}{(1+y)} \frac{1}{\tilde{n}} \equiv \frac{\tau_{Z,0}}{\tilde{n}}. \quad (3.2)$$

Here, $\lambda_{D_{i0}}$ was the initial ion Debye length, $v_{T_i} = \sqrt{8k_b T_i / \pi m_i}$ the thermal velocity of the ions and $y = -eV(a)/k_b T_e$ the reduced particle potential with V the potential of the particle surface. Equation 3.2 originates from the Orbital Motion Limited (OML) theory [123] which evaluates the current balance of charged plasma species at the particle surface. Note that $\lambda_D > a$ everywhere in the SPA, which justified the use of OML theory [125].

The electron temperature relaxation timescale τ_{T_e} described the typical energy loss time for the electrons in the SPA region. Due to collisional energy losses, T_e

relaxed, which was described by $d\tilde{T}_e/dt = -(\tilde{T}_e - 1)/\tau_{T_e}$. The governed timescale for this relaxation was given by [74]

$$\tau_{T_e} = \sqrt{\frac{2m_i}{\pi m_e}} \frac{\lambda_{ea}}{v_{T_i}} \frac{1}{\sqrt{\tilde{T}_e}} \equiv \frac{\tau_{T_e, \infty}}{\sqrt{\tilde{T}_e}} \quad (3.3)$$

Here, λ_{ea} was the mean free path between electron-argon collisions and $\tilde{T}_e = T_e/T_i$. Possible energy loss caused by diffusion to the tube walls and successive recombination [126], rendered it hardly feasible to make accurate estimations and could only decrease τ_{T_e} even more. Hence, Equation 3.3 provided an upper limit for τ_{T_e} .

The model described above was only valid if the particles could adapt their charge to plasma changes in the SPA, i.e. $\tau_Z < \tau_{pp}$. Since $\tau_{pp} \propto 1/\sqrt{\tilde{n}}$ and $\tau_Z \propto 1/\tilde{n}$, τ_Z exceeded τ_{pp} for densities below $(\tau_{Z,0}/\tau_{pp,0})^2 n_{e,i} = 2 \times 10^{11} \text{ m}^{-3}$. This density limit was close to the free diffusion regime, where the diffusion of ions and electrons was no longer governed by ambipolar diffusion. This regime starts when the ratio $\lambda_D/\Lambda \sim 1$, where $\Lambda \approx D/2\pi$ is the typical diffusion length, assuming an infinitely long square beam [127, 128].

The main parameter that determined the particle charge in our SPA was T_e . It was likely that $T_e \sim T_i$ at the position of charge measurement. We supported this statement with three arguments. First, the model showed that $\tau_{T_e} \ll \tau_I = L/v_{p,f}$, where τ_I was the time that the particles resided in the plasma and L the distance between the active plasma region and the position of particle charge measurement (see Figure 3.1). Second, we showed that the local RF electric strength at the bottom of the setup was small, $E_{RF} \approx 0.1 \text{ V m}^{-1}$ (see subsection 3.4.1). Considering that the electron mean free path $\lambda_{ea} \approx 2 \text{ mm}$, heating of electrons was negligible at this position in the SPA. Moreover, there were no resonant electron attachment processes on vacuum impurities close to $\tilde{T}_e \sim 1$ [129–131]. In conclusion, the output of this model using $T_e = T_i$, according to OML theory, proved the particle charge at the late stage of the SPA $Q_m = -175 e$.

3.4.5 Comparison of model and results

Both the measured charge $Q = -30 \pm 7 e$ and the model-predicted charge $Q_m = -175 e$ indicate particle charges that were significantly lower compared to the situation in the plasma bulk. The fact that they deviated by a factor of six from one another could be due to plasma shielding, the transition from ambipolar to free diffusion, collisionality corrections in the ion flux to the particle surface and the presence of anions. These mechanisms and their relative importance will be discussed below.

First, to exclude the possibility of plasma shielding [16], the measured horizontal acceleration as a function of the average horizontal distance of the particles between the electrodes is plotted in Figure 3.10. If there were plasma present between the electrodes, the acceleration would have varied with the distance (since the particle charge scales with the plasma potential). However, both the data with (in red) and without (in blue) the externally applied electric field show the same slope. Therefore, we can conclude that there was no significant amount of plasma present between the electrodes that affected our measurements. This statement is supported by the particle

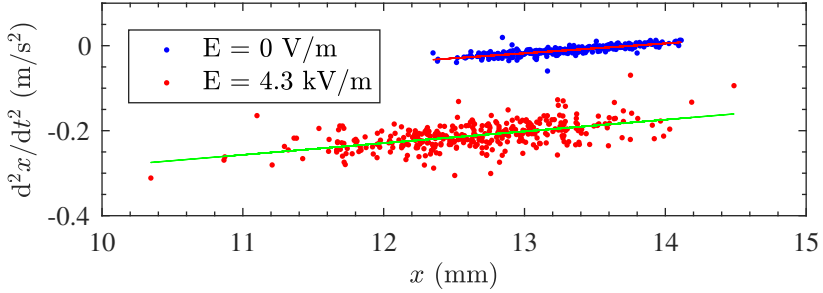


Figure 3.10: Plot of the measured horizontal acceleration as a function of the horizontal distance between the electrodes. Each blue data point depicts a particle that has travelled through the plasma with a 50 sccm flow in the absence of the externally applied electric field. In contrast, each red data point depicts a particle that was subject to an electric field of $E = 4.3 \text{ kV m}^{-1}$, with all other conditions identical to those for the blue circles. The origin of the x-axis is at the left electrode as seen from the position of the camera.

trajectories and quadratic fits shown in Figure 3.7b of which the clearly overlapping trajectories and fits indicate that the particles did not discharge during the typical 0.1 s measurement time.

Second, in the free diffusion regime the ratio $n_i/n_e > 1$ since electrons diffuse faster than ions, which causes the particles to discharge with respect to Q_m . Cou edel et al. [56] have shown that the transition to free diffusion influences the particle charge, which could explain (part of) the difference between the predicted model and the measured particle charge.

Third, collisionality, which could influence the ion current to the particle, was not taken into account in the discharging model. For $\lambda_D/\lambda_{ia} \approx 10^{-1}$, the particle charge was lowered because the ion current to the particle surface was increased due to a longer residence time of ions around the particles [16,80]. For increasing λ_D/λ_{ia} , the particle charge became more negative since ion-neutral collisions reduced the ion current. This effect could have changed Q by a factor 2-3 as compared to the OML particle charge [16,80]. It is therefore likely that collisionality did not constitute the only mechanism accounting for the difference between measurements and model.

Finally, the presence of anions could have influenced the particle discharging as the current of these anions to the particle surface would have directly affected the charging. However, since the production of anions could only occur for T_e of several eV [129–131] and since the lifetime of the dominant anions that could be present in our setup was much smaller than τ_I [132], the influence of anions was considered negligible.

3.5 Conclusion

In this chapter, we have introduced the PPCI setup together with the particle tracking algorithm. Both elements form the main diagnostic of this thesis. The power of the used technique lies in the fact that the individual charge of multiple particles can be measured simultaneously.

In this way, we have measured the charge of microparticles $-30 \pm 7 e$ in a low-pressure spatial plasma afterglow 0.55 m from the active plasma region, which is three orders lower than the particle surface charge expected in the connected bulk plasma. A relatively simple model was developed and applied to this plasma geometry. This made it possible to qualitatively explain the vast difference in particle charge between the bulk and its spatial plasma afterglow.

Charge control of microparticles in a shielded plasma afterglow

Abstract

This chapter discusses charge control of microparticles from ~ -40 to $+10$ elementary charges is presented. This is achieved at 90 Pa argon in the spatial plasma afterglow of an inductively coupled plasma by solely changing the strength of an externally applied electric field. Crucial in the presented experiments is the use of a grounded mesh grid in the cross-section of the setup, separating the active plasma region from the shielded spatial plasma afterglow. While in the regions above the mesh grid all particles reached a constant negative equilibrium charge, the actual control achieved in the shielded spatial plasma afterglow can most probably be explained by variations in the local ion density. The achieved charge control not only opens up possibilities to study nanoscale surface charging physics on micrometer length scales, it also contributes to the further development of plasma-based contamination control for ultra-clean low-pressure systems.

This chapter is published as:

B. van Minderhout, J.C.A. van Huijstee, B. Platier, A.T.A. Peijnenburg, P. Blom, G.M.W. Kroesen and J. Beckers (2020), “Charge control of micro-particles in a shielded plasma afterglow” *Plasma Sources Science and Technology* **29** 065005

4.1 Introduction

In dusty or complex plasmas, i.e. plasmas containing nano- to micrometer sized particles, the plasma-induced particle surface charge is known to be one of the key parameters driving elementary processes such as ion drag [16, 17], local Debye shielding [18], Coulomb-interactions in strongly coupled plasmas [19] and plasma-particle synthesis [14]. In the latter example, the particle charge is especially important in the particle coagulation step [26, 27]. In the bulk of a plasma, microparticles typically reach a permanent negative charge of $(10^3 - 10^4)$ elementary charges [123]. This is due to the fact that the particle charge is determined by the balance of ion and electron fluxes reaching the surface of the particle. Since the electrons are much more mobile than ions, an equilibrium in flux is achieved for a negative surface potential.

In the region where the plasma was not actively powered, i.e. the plasma afterglow, the typical charge of particles proved significantly lower than in the plasma bulk [52, 53, 133]. The evolution of the particle charge, however, differs for temporal and spatial plasma afterglows. Where in the temporal afterglow the charge is determined by the plasma changes in time [52–59], in the largely unexplored Spatial Plasma Afterglow (SPA), the particle charge is determined by the spatial evolution of plasma parameters, such as the electron temperature and the plasma density. In the case of the temporal afterglow, it is a well-established fact in the literature that a DC field can influence the particle charge. Wörner et al. [134] experimentally showed that a DC field could shift the charge distribution of microparticles from a negative to a positive mean value at high dust densities. The authors studied this effect for a single DC electric field strength. In addition, Couédel et al. showed that the particle charge was determined by the manner in which the transition from ambipolar to free diffusion took place [56]. In any case, it remains difficult to control the particle charge in the plasma afterglow. Yet, particle charge control opens up a wide variety of opportunities both from a fundamental and an application perspective.

Fundamentally, charge control of microparticles allows one to study nanoscale surface physics on micrometer length scales. Examples of relevant processes are photodetachment [135], photoionisation [136], charge attachment [137, 138] and secondary electron emission [139]. From an application point of view, charge control of particles could improve the properties and deposition of silicon nanocrystals, which are synthesised in reactive plasmas [140] for the creation of nanodevices.

In addition, particle contamination has become an increasingly significant problem in many ultra-clean low-pressure systems, as is evident from the multi-billion-dollar semiconductor industry [50]. Charge control in this situation is an important step in enabling in situ particle contamination control [133]. The principle of such a plasma-assisted particle mitigation technique is based on the ability of plasma to both electrically charge the contaminating particles and to affect the trajectories by the plasma-induced electric fields [51].

Considering that the mentioned fundamental opportunities and applications have high potential, carefully controlling the charge of these particles is crucial. This has been far from trivial until now, which is illustrated by the following three examples.

First, it is virtually impossible to generate or directly inject neutral particles in a system because of the triboelectric effect [141]. Consequently, a charge control technique must be able to reset the triboelectrically induced charge distribution, which includes both positively and negatively charged particles [118].

Second, Bennet et al. reported on a multi-step charge control process [142]. In this process, the microparticle was encapsulated in a water droplet prior to charging the droplet in a plasma discharge. The droplet then evaporated outside the plasma until the Rayleigh limit was reached. The authors (*ibid.*) claimed that when the droplet collapsed, a precise amount of charge was delivered to the particle because of this Rayleigh limit. This example showed that controlling the charge of microparticles is a complex and multi-step process in which one has to deal, for instance, with plasma afterglow effects and water vapour contamination, for instance.

Third, the PK4 experiment has the ability to carefully alter the particle charge in the active plasma region [143, 144]. While the control of the microparticle charge in the latter experiment was achieved by varying the pressure, these variations in pressure also changed the drift velocity and the position of the particles.

The respective examples show not only that plasma is needed to reset the initial charge of the particles, but also that a complicated multi-step process is required to get a precise amount of charge on microparticles outside the active plasma region.

In previous work, we measured the particle charge in the free SPA [133] (see chapter 3), i.e. without application of a mesh grid. In chapter 3 we have shown that the charge in the free SPA was significantly lower than the charge in the plasma bulk, which then served as a proof of principle of our measurement technique. In this chapter, we introduce a plasma-based method to control the charge of microparticles around zero ($\sim -40e$ to $+10e$) through the application of a grounded mesh grid and through variation of a DC electric field below and towards the mesh grid. The applied electric field in this work changes the local ion density in the shielded SPA, thereby allowing charge control over particles with both positive and negative charges. The strength of this technique is that it involves only a one-step process.

In the next sections of this chapter, the author will first discuss the particle charging theory (section 4.2) and subsequently introduce the experimental setup and diagnostics used in section 4.3. Special focus will be on the key variable in the presented method, i.e. the externally applied electric field. Subsection 4.4 then discusses the proof of principle of our charge control method. The physical interpretation is elaborated upon in section 4.5 which is divided in our experiment's three defined regions: the active plasma region, the sheath above the mesh grid, and the shielded SPA where the actual charge control is achieved.

4.2 Particle charging theory

As explained in the introduction, dust particles generally acquire a negative charge in a low-pressure plasma [123]. The acquired charge is in most cases described by the Orbital Motion Limited (OML) theory [123, 145]. In this theory, the plasma sheath around the particle is assumed to be collisionless and, furthermore, it is assumed that ions and electrons are collected by the particle when their orbits overlap. The OML

theory can be applied only as long as the particle radius $r_p \ll \lambda_D$, where λ_D is the Debye length, the smallest length scale on which plasma parameters can be considered constant.

For an isolated particle in a plasma with Maxwellian electrons and exclusively positive ions, the ion current I_i and the electron current I_e collected by the particle can be expressed as [79]

$$I_{i,e} = \begin{cases} I_{i0,e0} \left(1 - \frac{q_{i,e} \phi_s}{k_B T_{i,e}}\right) & \text{if } q_{i,e} \phi_s \leq 0 \\ I_{i0,e0} \exp\left(-\frac{q_{i,e} \phi_s}{k_B T_{i,e}}\right) & \text{if } q_{i,e} \phi_s \geq 0. \end{cases} \quad (4.1)$$

As can be seen, the ion and electron current depend on the surface potential of the particle ϕ_s as well as on the charge $q_{i,e}$ and the temperature $T_{i,e}$ of the ions and the electrons. Furthermore, in Equation 4.1, k_B is the Boltzmann constant and $I_{i0,e0}$ is the current collected at $\phi_s = 0$. By solving the current balance $I_i = I_e$, the particle charge Q can be derived for a spherical particle according to

$$Q = 4\pi\epsilon_0\epsilon_r r_p \phi_s \quad (4.2)$$

where ϵ_0 and ϵ_r are the respective vacuum and relative permittivities.

At $p = 90$ Pa argon, the pressure used in this work, the plasma sheath (around the particle) is not collisionless and the ion current is, therefore, altered by ion-neutral collisions. Yet, these collisional effects only change the particle charge in the plasma bulk by a factor three at maximum [16,80] and, therefore, collisional effects are omitted in the analysis in this work.

The particle charging timescale τ_Z , which is the characteristic timescale a particle needs to reach its equilibrium charge in a plasma, can be derived from the OML theory. For the usual situation in a low-pressure plasma where $T_e \gg T_i$ the charging timescale τ_Z is given by [125]

$$\tau_Z = \frac{4\epsilon_0}{e^2} \sqrt{\frac{k_B T_i \pi m_i}{8}} \frac{1}{r_p n_{e,i} (1 + y_0)}. \quad (4.3)$$

Here, e is the elementary charge of an electron, m_i the ion mass and y_0 the equilibrium value of the reduced particle potential $y = e\phi_s/k_B T_e$.

4.3 Experimental setup

This section presents the experimental setup and the particle diagnostic. The following paragraph briefly introduces the main elements of the Plasma Particle Charging Investigation (PPCI) setup [133], followed by an elaboration of the most relevant parts in separate subsections, moving from the top to the bottom of the setup.

The PPCI setup is a vacuum system consisting of a 1 m glass tube with a base pressure of roughly 5×10^{-9} Pa. A sketch of the PPCI setup is shown in Figure 4.1. In order to increase the accuracy of the charge measurements and to simplify the analysis, a square cross-sectional shape was chosen for the tube with an inner width of $D = 0.1$ m.

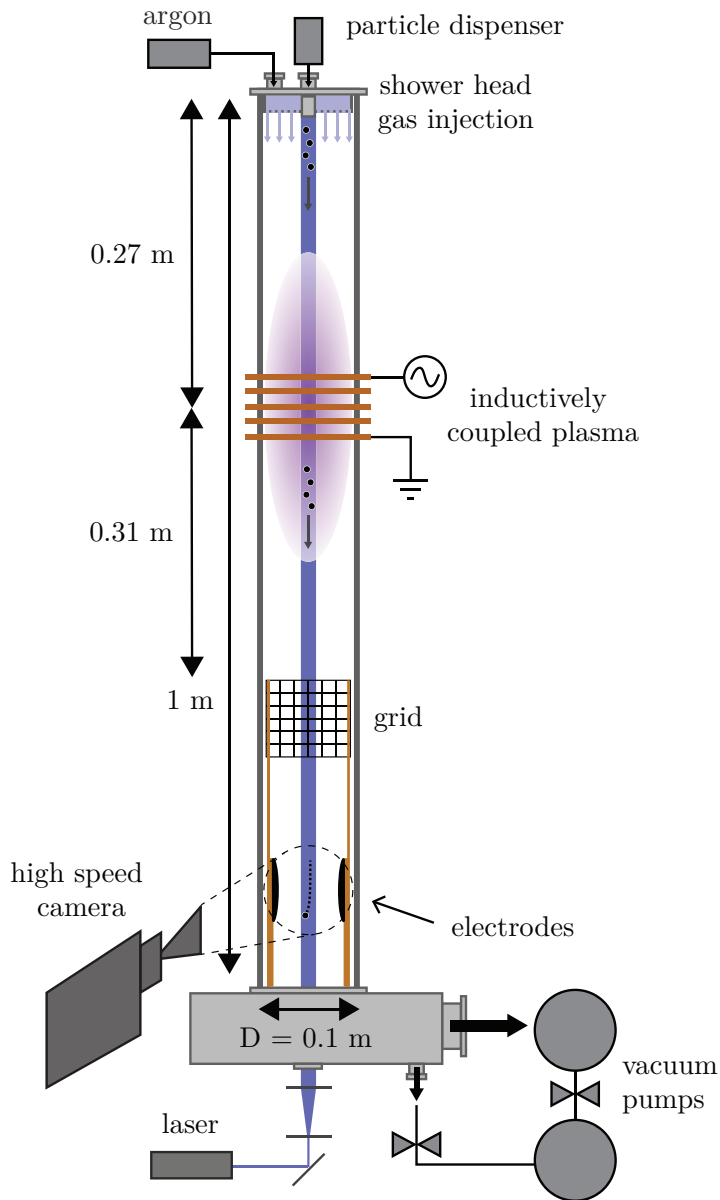


Figure 4.1: Schematic drawing of the PPCI setup in which microparticles fell through a spatially limited region of plasma after which their charge was measured by accelerating them in an externally applied electric field. In this study, the SPA was shielded from the active plasma region by a grounded mesh grid.

At the top of the glass tube, a shower head was mounted through which gas and particles were injected. After injection, these particles fell through an Inductively Coupled Plasma (ICP) which was generated using a five-turn square coil wound around the outside of the tube. This active plasma region was shielded from the remainder of the setup by a grounded metal mesh grid in the cross-section of the tube downstream of the ICP. In the shielded SPA below the mesh grid, the charge control of the particles was verified by measuring the position, velocity and acceleration of these particles in an externally applied electric field created by two Rogowski electrodes [115]. During their fall through the entire setup, the particles were illuminated with a laser system and their scattered light was recorded by a high-speed camera.

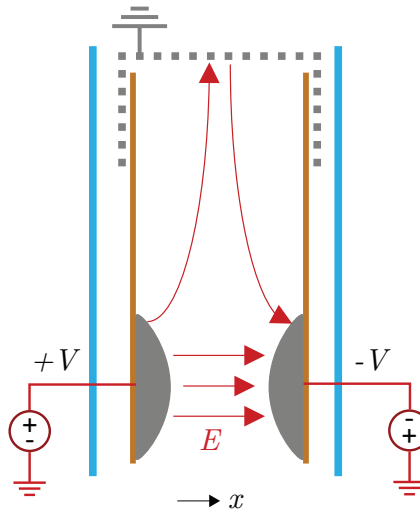


Figure 4.2: Sketch of the field lines present in the shielded SPA of the PPCI setup. Indicated in blue are the walls of the glass tube, in brown the peek (polyetheretherketone) stands that support the electrodes and the mesh grid, and in red the field lines. The potential is applied to the electrodes using two power supplies.

4.3.1 Particle and gas injection

At the top of the PPCI setup, particle and gas injection were combined in the showerhead. The microparticles, supplied by microParticles GmbH, consisted of a melamine formaldehyde (MF) core and a porous silver coating with a thickness of ~ 100 nm to minimize triboelectric charging effects [141]. These particles, with a diameter $4.9 \pm 0.2 \mu\text{m}$ and (supplier-provided) particle mass of $m_p = 9 \times 10^{-14}$ kg, were injected using a particle dispenser similar to those used in earlier studies [117,118]. After injection, the particles left the showerhead at its center through a 5 mm thick and 40 mm wide slit. On the one hand, this slit ensured that particles were injected

into a defined volume matching the laser sheet dimensions; on the other hand, the slit served as a beam dump for the laser. The 10 sccm argon flow, regulated with a Brooks SLA850 mass flow controller, was distributed over the entire cross-section of the tube through ≈ 200 holes of 0.5 mm in diameter equally distributed around the slit. In this manner, the flow entrance effects were reduced and stable particle injection was ensured. In addition, the flow combined with gravity accelerated the particles to a measured settling velocity $v_{p,f} = 0.13 \text{ m s}^{-1}$.

4.3.2 Active plasma region

By sending a radiofrequent (RF) current at 13.56 MHz through a five-turn square coil wound around the outside of the tube, an ICP was created inside the tube. The RF signal was generated with an Agilent 33220A function generator, amplified by an E&I AB250 power amplifier and matched with a T-matching circuit in order to convert the complex plasma impedance at 13.56 MHz to a 50Ω resistive load seen by the amplifier. Taking the center of the coil as a reference, the coil was placed 0.27 m under the showerhead and 0.31 m above the grounded mesh grid. This mesh grid limited the active plasma region in volume and created the SPA region downstream. The region below the mesh grid will be referred to in this thesis as the shielded SPA, which is of main interest in this work.

The wires of the mesh grid had a diameter of 0.37 mm and the distance between two wires was 1.13 mm. Because of the presence of the mesh grid, the plasma was mainly capacitively coupled, which was supported by the plasma density measured using the Microwave Interferometer MWI 2650. This MWI system had an operating frequency of 26.5 GHz and was used and described in previous research [146, 147]. The measured density 26 mm above the mesh grid, obtained using extrapolation and without sheath path length correction, was $n_{e,i} \approx 10^{14} \text{ m}^{-3}$. The measured value of $n_{e,i}$ corresponded to the E-mode of ICPs [71] which is the capacitive mode. The main message here is that the plasma was mainly capacitively coupled due to the presence of the mesh grid. In this manner, 6 W of power was delivered to the plasma volume at an argon pressure of $p = 90 \text{ Pa}$.

4.3.3 Rogowski electrodes

The plasma-induced charge of the microparticles was measured by accelerating them in an externally applied DC electric field directed perpendicular to the settling velocity vector of the particles. This field was created by applying a voltage difference between two Rogowski electrodes [115]. The curved shape of these electrodes suppressed the field enhancement near the edges of the electrodes, which increased the maximum electric field that could be applied in the central region of the electrodes without creating a DC glow discharge. The Rogowski electrodes were 70 mm in diameter and had a separation distance of 40 mm. A 2D electrostatic model was set up in COMSOL to obtain the electric field profile as shown in Figure 4.3, from which follows that the horizontal field strength in the central region $30 \times 30 \text{ mm}$ between the Rogowski electrodes (indicated in Figure 4.3 by dashed lines) differed at max. 30%. Consequently, the electric field was considered to be constant in this region.

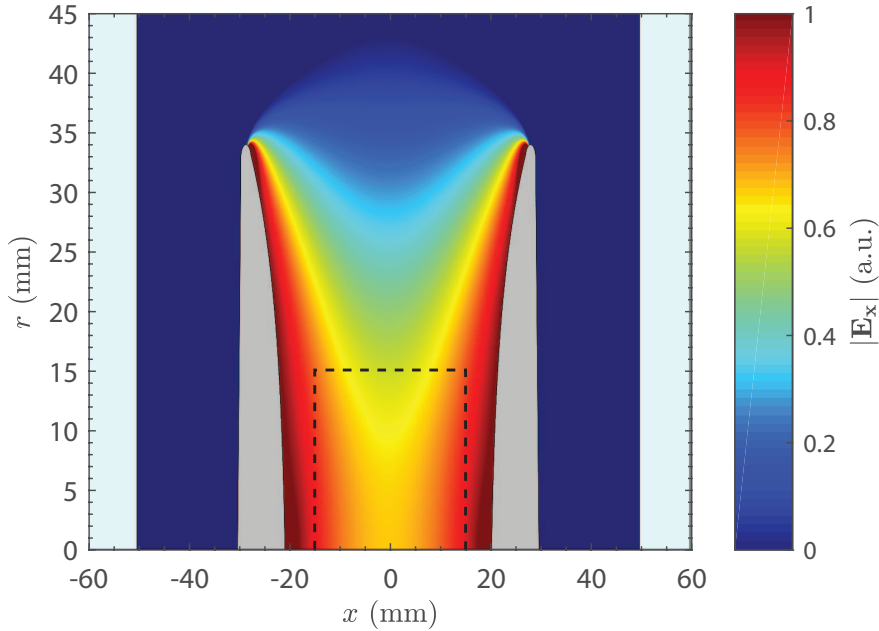


Figure 4.3: Normalised horizontal component of the electric field created between the Rogowski electrodes. The electrodes are indicated in grey and the glass tube in light blue. Cylindrical geometry is used (the x-axis is the axis of symmetry), which implies that the front and back glass plate of the tube are not taken into account in the simulation. A potential difference of 300 V is applied between the electrodes.

The breakdown electric field between the electrodes was experimentally measured to be $E_{bd} = 8 \text{ kV m}^{-1}$ while the ICP was ignited. The maximum electric field used in the experiments was 5 kV m^{-1} , far below E_{bd} . Therefore, it is evident that possible reionisation had a negligible effect on the particle charge.

In addition to the field between the electrodes, the presence of the grounded mesh grid also created a field above the electrodes both in the horizontal and vertical directions. In Figure 4.2 field lines are sketched which visualize these field components.

Using a Trans Impedance Amplifier (TIA), the AccTec electrometer 2, the anode and cathode currents to ground were measured to analyse the electron and ion current received by the electrodes. Figure 4.4 schematically depicts the configuration in which these experiments were performed. In order to suppress the RF noise, a low-pass RC-filter was applied with a cut-off frequency of 100 kHz. In addition, the current measurements were performed in a floating configuration, i.e. the oscilloscope (Agilent DSO-X 2020A) and the TIA were not grounded, as indicated in Figure 4.4. In order to increase the accuracy of the current measurements, the TIA was read out by an oscilloscope over a period of 2 s with a sampling frequency of 25 kHz. Subsequently, the

average current was used in the further analysis. It will be shown in the results section that the electrodes played a crucial role in the particle charge control, in addition to their importance for the charge measurement.

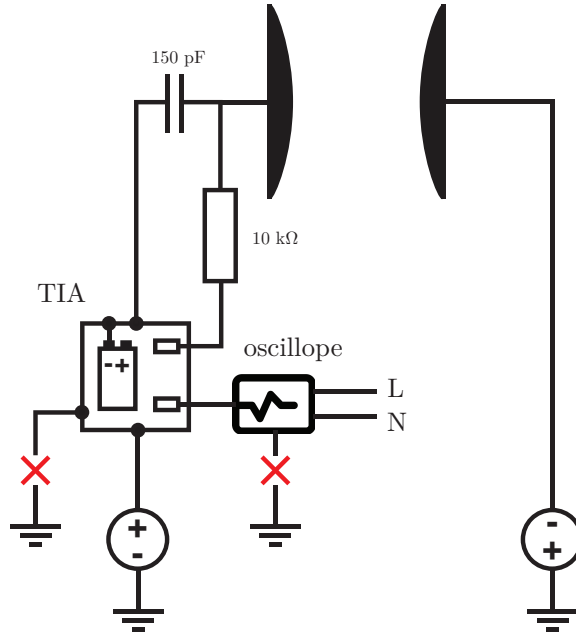


Figure 4.4: Sketch of the electrical configuration in which the cathode and anode current to ground have been measured. Neither the Trans Impedance Amplifier (TIA) nor the oscilloscope are grounded.

4.3.4 Particle trajectory imaging

The trajectories of the particles were visualised within the imaging window by laser light scattering. To this end, a diode laser with a central wavelength of 447 nm was used together with collimation optics and cylindrical lenses to create a 3 mm thick and 40 mm wide laser sheet. This laser sheet was directed antiparallel to the direction of the settling velocity of the particles (see Figure 4.1). The scattered laser light was imaged by a Photron Fastcam mini UX100 high-speed camera at 1000 fps, with its viewing direction perpendicular to the plane of the laser sheet. It is the 3 mm thickness of this laser sheet which assured that particles moving towards or away from the camera, i.e. particles that were moving parallel to the viewing direction of the camera, were only shortly imaged and thereby omitted in the analysis. A representation of the typical raw data of the measured particle trajectories is shown in Figure 4.5 which clearly shows the low particle density in our experiments.

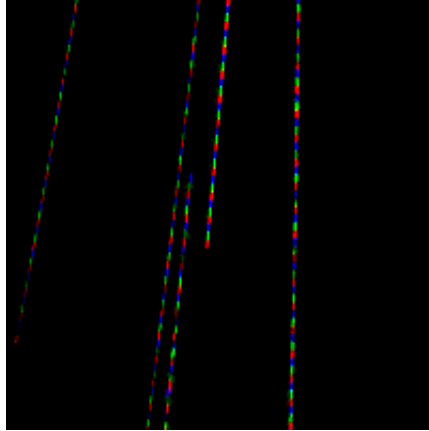


Figure 4.5: Typical raw image of particles travelling in the region between the electrodes. 54 frames are subsequently coloured red, green and blue indicating the movement of the particles. The images are recorded in gray scale at 1000 fps. The representation shows a zoomed part (6×6 mm) of the total field of view.

The field of view (FoV) of the camera was approximately 40 mm in a horizontal direction and 32 mm in a vertical direction, with the particles only being detected in the central 30 mm in a horizontal direction (see Figure 4.9). Consequently, 1 pixel corresponded to roughly $32 \mu\text{m}$, which is much larger than the diameter of the microparticles. In order to increase the particle detection accuracy, the optics were slightly put out of focus. As a result, the particles were detected on multiple pixels and their positions could consequently be determined at sub-pixel accuracy.

4.3.5 In-house developed particle tracking software

In order to obtain information about the charge of the microparticles, their horizontal velocity and acceleration were obtained from the recorded trajectories using in-house developed particle tracking software written in Matlab. The analysis consisted of a three-step process.

First, the positions of all particles in each frame were determined. Using morphological operations, a mask was generated that located the positions of all particles. The exact location of each particle detection was determined by calculation of its intensity weighted midpoint. Here, it was important that each particle detection consisted of multiple pixels. This was achieved by deliberately placing the optics slightly out of focus (see subsection 4.3.4). In this way, the particle positions were determined in each frame with an accuracy of approximately $5 \mu\text{m}$.

Second, these individual particle positions were linked in order to create trajectories. For the particles detected at the top of the frames a new trajectory was started. For all other particle positions, the cost (the difference between the measured and expected particle position) was calculated to assign the detections to each existing trajectory. In this way, a cost matrix was created and subsequently solved by finding the lowest

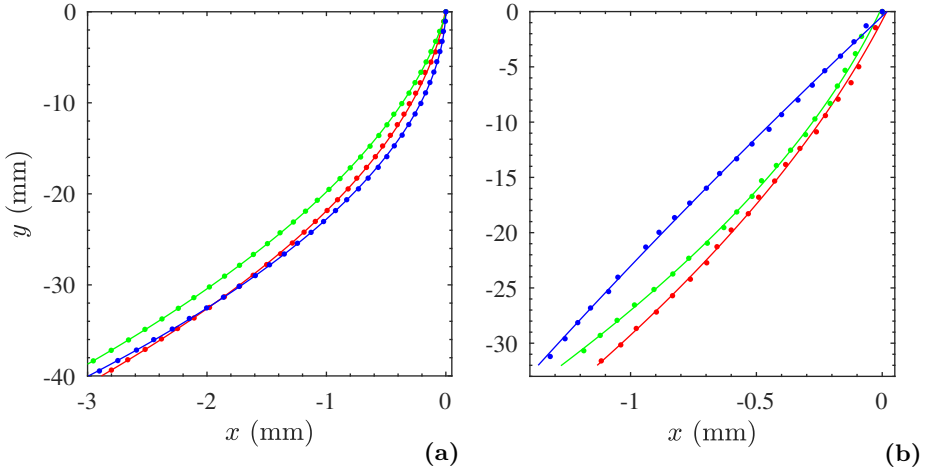


Figure 4.6: Three typical particle trajectories together with a quadratic fit in the region of an externally applied electric field. Figure (a) shows the trajectories in the free SPA for $E = 4.3 \text{ kV m}^{-1}$ [133] and Figure (b) in the shielded SPA for $E = 1.25 \text{ kV m}^{-1}$. Every tenth data point is plotted for clarity. In addition, the starting point of each trajectory is transformed to the origin.

total linking cost. Thereby, all positions in one frame were simultaneously assigned to the existing trajectories, or new trajectories were started. In more detail, the linking cost was determined by the difference between the Kalman filter's prediction of the next position of the trajectory and the particle detections. The cost matrix was solved using the Hungarian assignment algorithm.

Third, the trajectories were quadratically fitted and their horizontal velocity and acceleration (anti)-parallel to the externally applied electric field were obtained amongst other parameters. In this manner, the determined velocity was the initial velocity with which particles entered the field of view, and the acceleration the change in velocity within this region. The locally obtained acceleration was not the local derivative of the velocity.

4.3.6 Charge measurement

In previous work [133] (see chapter 3), the charge in the free SPA with the same configuration but without grid, was obtained from the horizontal acceleration which the residually charged particles experienced in the region of externally applied electric field. The particle charge in this chapter, however, is based on the horizontal velocity. While the horizontal acceleration of the small particle charges was not much larger than the flow disturbances, the horizontal velocity showed the integrated effect of the electric field in the region above the field of view. The flow disturbances are discussed in more detail in subsection 4.5.3. The velocity was therefore used for analysis of the particle charge instead of the acceleration.

To illustrate the difference between the particle trajectories measured in the free SPA [133] and the shielded SPA reported here, typical trajectories of both situations are shown in Figure 4.6. It is clear that the acceleration of the trajectories in Figure 4.6(b) is smaller than that in Figure 4.6(a). Independent of the charge, the strength of this measurement technique was the ability to simultaneously measure the individual charge of multiple particles as long as all particles were within the imaging region.

More details on the accuracy of this measurement technique were elaborated upon in our previous publication [133](see chapter 3). In that study, it was also shown that mutual Coulomb interaction between the particles could be neglected due to the low particle density. In addition, it was shown that the afterglow plasma did not influence the electric field distribution at the position of the electrodes. These experiments were performed in the free SPA where the plasma density was higher than in the shielded SPA reported here. Therefore, it can be concluded that the afterglow plasma did not influence the field distribution at the position of the electrodes in the experiments reported in this work.

4.4 Results of charge control

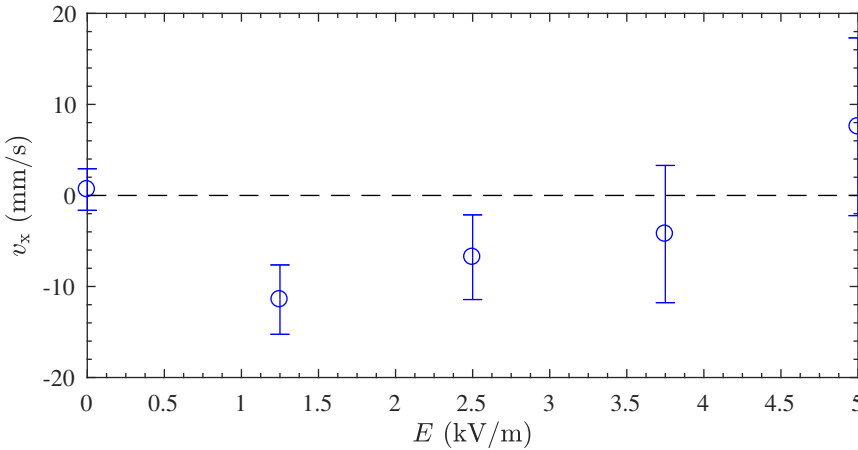


Figure 4.7: Horizontal velocity v_x as a function of the externally applied electric field strength E in the shielded SPA. The bars around the data points do not represent an error, but rather the spread indicated by the one-sigma interval. Furthermore, the figure shows the combined data of 10 separate experiments (two for each value of E) consisting in total of 8623 particles.

In this section, the proof of principle of the particle charge control technique is presented. Figure 4.7 shows the horizontal velocity v_x of the particles as a function of the externally applied electric field E applied to the electrodes in the shielded SPA. This figure shows that $v_x \approx 0 \text{ mm s}^{-1}$ for $E = 0 \text{ V m}^{-1}$ which is expected, since the electric force (if present) is the dominant one in the horizontal direction. The fact that

v_x is not exactly equal to zero for $E = 0 \text{ V m}^{-1}$ is caused by flow effects as explained later in this chapter. In addition, it shows that v_x is initially negative when a field is applied and becomes less negative with an increasing field strength, eventually even reaching a positive mean value. The sign of v_x is a direct indication of the particle charge sign. While a negative value of v_x corresponds to negatively charged particles, a positive value indicates that the particles are positively charged. Section 4.5 will show that the vertical electric field between the mesh grid and the electrodes (see Figure 4.2) holds a key role in the charge control principle.

An upper estimate of the particle charge Q is shown in Figure 4.8. This estimate is obtained by assuming that the measured horizontal velocity is solely caused by the integrated effect of the electric field created by the electrodes above the field of view (FoV). The FoV is indicated by the dashed lines in Figure 4.3. This means that, for the charge estimate, it is assumed that the horizontal electric field strength above the electrodes is zero (between the electrodes and the mesh grid).

More specifically, the electric field between the electrodes, but in the $y_t = 20 \text{ mm}$ above the FoV (see Figure 4.3), is taken to be constant with a magnitude equal to E in the centre of the electrodes. Using the vertical settling velocity ($v_{p,f} = 0.13 \text{ m s}^{-1}$), the residence time of the particles is obtained $t_r = y_t/v_{p,f} = 0.15 \text{ s}$. The particle charge in electrons can then be estimated using the simple formula $Q = v_x m_p / E t_r$, which originates from the assumption that the horizontal velocity is caused by a constant electric-field-driven acceleration during t_r . The upper estimate for the particle charge obtained in this way is in accordance with the particle charge measured in the free SPA in our previous work [133] (see chapter 3).

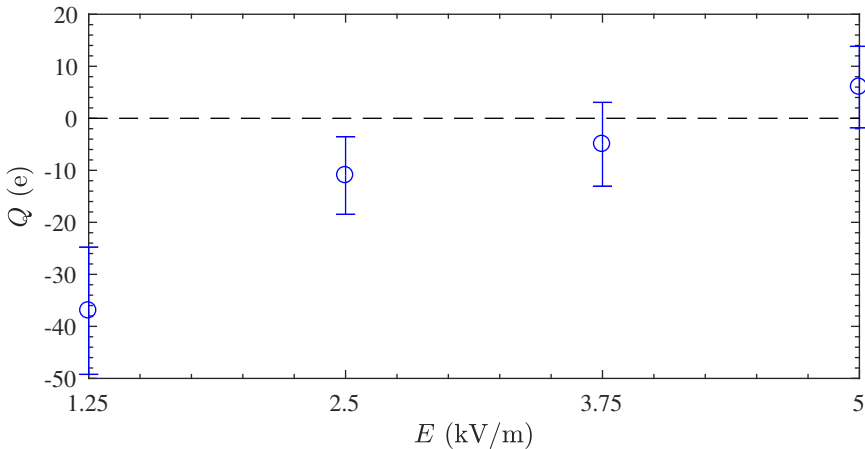


Figure 4.8: Upper estimate of the charge Q as a function of the externally applied electric field E in the shielded SPA. The bars around the data points do not represent an error, but rather the spread indicated by the one-sigma interval. Furthermore, the figure shows the combined data of 10 separate experiments (two for each value of E) consisting in total of 8623 particles.

Note that the bars around the data points in Figure 4.7 and Figure 4.8 do not represent an error, but rather the spread in v_x and Q (which is indicated by the one-sigma interval). It can be observed that the spread in v_x increases with increasing magnitude of E , whereas the spread in Q remains approximately constant, which is in accordance with expectation. For a higher electric strength, the deviations in electric force and, consequently, also the deviations in v_x are more distinct. The approximately constant spread in Q is not only caused by variations in particle size, leading to variations in charge and mass, but also by the stochastic nature of the plasma charging currents arriving at the particle surface [124]. These effects were discussed in more detail in our previous work [133] (see chapter 3).

The trends observed in v_x and Q as a function of E prove the ability to control the charge of the microparticles in the PPCI setup by varying only the externally applied electric field. It will be shown in the next section that this can be explained by the local changes in ion density in the shielded SPA.

4.5 Physical interpretation

This section is dedicated to the interpretation of the physical processes that determine the presented charge control. In the following subsection, arguments and results are discussed to explain and substantiate the proof of principle presented in section 4.4. These results are explained in three subsections corresponding to the three main regions which determine the charge of the microparticles: the active plasma region, the sheath layer above the mesh grid and the shielded SPA.

4.5.1 Active plasma region

In the active plasma region, the initial triboelectric charge distribution is reset and all particles reach an equilibrium charge which will be estimated here. Collisional effects will be briefly discussed as well.

In the quasineutral active plasma region, Orbital Motion Limited (OML) theory (see section 4.2) can be applied to calculate the charge of the particles [123, 148]. For a typical electron temperature of $T_e = 1$ eV [72, 149], the charge acquired by the $4.9 \pm 0.2 \mu\text{m}$ particles is around $Q_a = -5 \times 10^3 e$. The plasma density in the active plasma region was measured using microwave interferometry (MWI) (see subsection 4.3.2) and resulted in a typical value of $n_{e,i} = 10^{14} \text{m}^{-3}$. Consequently, the charging timescale of the particles was in the order of microseconds (see Equation 4.3). If this is compared to the fact that the particles resided in the active plasma region for several seconds, it can be concluded that all particles (assuming mono-dispersity) reached the same equilibrium charge independent of their initial triboelectric charge. Additionally, it should be mentioned that the dust particle density was sufficiently small to assume not only that the particles did not influence the plasma parameters, i.e. the so called Havnes parameter [150] which is around 10^{-4} , but also that mutual Coulomb-interactions were negligible (see subsection 4.3.6).

4.5.2 Sheath above mesh grid

It is likely that the charge of the microparticles, acquired in the active plasma region, changed drastically in the sheath layer above the mesh grid, as in this region the free electron density was depleted. In the next paragraph, the effect of the ion current, which is dominant over electron current, on the particle charge will be estimated. In addition, the influence of possible particle scattering on the mesh grid will be treated in the remainder of this section.

The plasma-charged particles were partially discharged in the sheath region above the grounded mesh grid. To provide a first order estimate of this effect, the total ion current arriving at the surface of the particles was calculated, neglecting Coulomb interactions between the ions and the particle, and assuming that the electron density equalled zero in this region. Using these assumptions, the number of ions collected by a dust particle N_i was estimated by

$$N_i = \pi r_p^2 v_b n_i \tau_t \approx 10^3. \quad (4.4)$$

Here, r_p stood for the radius of the particle, v_b the Bohm velocity and τ_t the transit time of the particle through the sheath region. The latter parameter was estimated by dividing the sheath size, taken to be 10 mm, by the settling velocity $v_{p,f} = 0.13 \text{ m s}^{-1}$. Consequently, the particle charge decreased from the plasma bulk value ($Q_a = -5 \times 10^3 e$) in the sheath layer above the mesh grid to approximately $Q_s = -(10^2 - 10^3) e$.

In addition to the local discharging, the particles were also influenced by an electric field in the sheath region above the mesh grid. Due to the orientation of the grid and the fact that the mesh grid size was much smaller than the sheath thickness, the electric field was mainly oriented in the vertical direction anti-parallel to the movement of the particles. Therefore, this vertical electric field did not influence the horizontal component of the trajectories measured between the electrodes.

Prior to a discussion of the results of the shielded SPA (subsection 4.5.3), the possible influence of particles scattering on the mesh grid is treated here. In Figure 4.9, a histogram of the horizontal position x of the first detection of 9119 trajectories is shown both with plasma (in red) and without plasma (in blue). The respective figure shows distinct peaks in the histograms at the positions where particles were not blocked by the wires of the mesh grid.

It is concluded that there was no significant scattering of both the triboelectrically charged and plasma charged particles on the mesh grid. Consequently, it is assumed that there was no significant charge exchange between the particles and the mesh grid. Moreover, no flow turbulence was detected to the extent that it influenced the particle trajectories. Heijmans et al. [118] have shown that the triboelectric charge of $100 \mu\text{m}$ polystyrene particles can be as large as $\pm 5 \times 10^6 e$. This shows that the triboelectric particle charge can be of the same magnitude or even larger than the particle charge in the active plasma region.

Yet, the minima between the peaks in Figure 4.9 are not zero. This could be caused by two factors. First, the mesh grid was not perfectly aligned with the laser sheet. Since the laser sheet was approximately 3 mm thick (see subsection 4.3.4), several rows of the mesh grid were imaged simultaneously. Consequently, overlapping peaks could

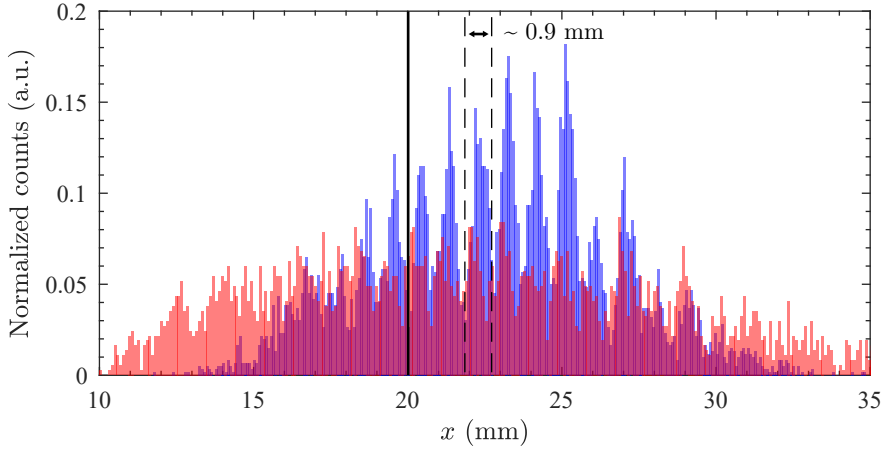


Figure 4.9: Histogram of the horizontal position x of the first detection of each trajectory for the situation without plasma (in blue) and with 6 W ICP (in red) for $E = 0 \text{ V m}^{-1}$. The figure shows the combined data of three separate experiments for each configuration consisting in total of 7791 particles without plasma and 3909 particles with plasma. The solid vertical line at $x = 20 \text{ mm}$ indicates the axis of symmetry.

have been created which could have resulted in non-zero minima. Second, the flow was compressed by the curved electrodes which means that the peaks were pushed together as well. This effect can also be seen in the distance between the peaks in Figure 4.9, which is approximately 0.9 mm, significantly smaller than the expected separation distance of 1.5 mm (see mesh grid geometry subsection 4.3.2). The effect of the curved electrodes on the flow will be discussed extensively in subsection 4.5.3.

When comparing the histograms of the particle density with and without plasma in Figure 4.9, it is clear that the plasma causes the particles to be more spread out over at least the volume of the laser sheet. This increase in spread could be caused by the temperature gradient present in the argon flow. Previous studies have shown that the neutral gas temperature in a low-pressure ICP strongly depends on the operation mode and can be elevated above room temperature [149, 151]. In addition, the increase in spread could be caused by the ion drag force pushing the particles to the walls of the glass tube.

Furthermore, it is clear that the local maxima of the distributions depicted in Figure 4.9 have shifted. This could be caused by the already mentioned flow compression effect and the horizontal temperature gradient since most of the particles passed through the right of the center of the electrodes (the center is at $x = 20 \text{ mm}$ in Figure 4.9 as indicated by the vertical solid line). Moreover, the global maxima of the distributions have also shifted. The cause of this effect is uncertain, since the particle charge in the situation where $E = 0 \text{ V m}^{-1}$ is unknown.

4.5.3 Shielded spatial plasma afterglow

The previous sections have discussed the influences of the active plasma region and the sheath above the mesh grid. In these regions, all particles reached a constant negative equilibrium charge independent of their initial triboelectric charge. The actual control of the charge was achieved in the shielded SPA. This section provides a detailed explanation of the governing mechanism.

First, the influence of the electrodes on the particle trajectories, as well as the measured horizontal acceleration as a function of the electric field strength, are discussed. Second, a current measurement is presented which shows that the ratio of n_i/n_e was actually changed by varying the electric field strength. Third, the magnitude of the ion drag is estimated, with the conclusion that this force proved negligible and thereby did not contribute to the observed phenomena. Finally, it is shown that ions were focused on the cathode and thereby created an asymmetric spatial charge distribution.

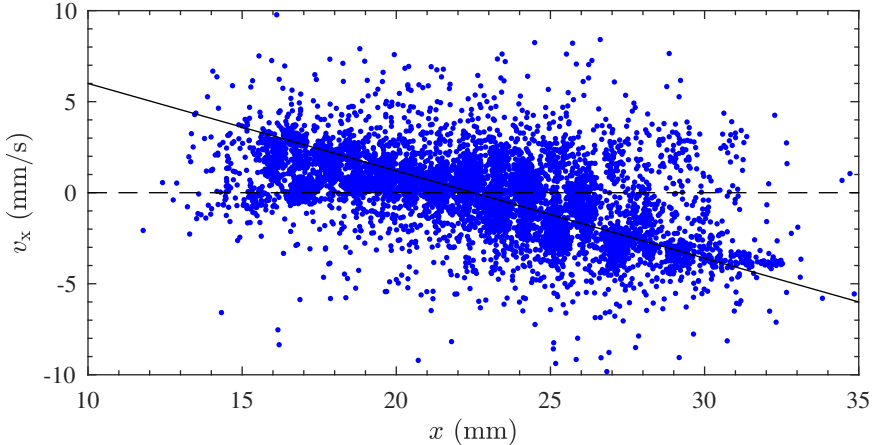


Figure 4.10: Scatter plot of the horizontal velocity v_x as a function of the first x position for the case without plasma and $E = 0 \text{ V m}^{-1}$. The figure shows the combined data of three separate experiments consisting in total of 7791 particles. A solid line is added to illustrate the v_x dependence on x and a dashed line to indicate the zero-crossing.

Acceleration at the electrodes

The curved electrodes that were used to generate the electric field had a separation distance of 40 mm (see subsection 4.3.3), whereas the tube had an inner width of 0.1 m. Consequently, the flow was compressed at this position, which influenced the particle trajectories. Figure 4.10 shows the horizontal velocity v_x , while Figure 4.11 illustrates the horizontal acceleration a_x for the situation without plasma and $E = 0 \text{ V m}^{-1}$. As expected, for most particles the initial velocity was directed towards the center of the tube, positive for $x \lesssim 20 \text{ mm}$ and negative for $x \gtrsim 20 \text{ mm}$, while the acceleration

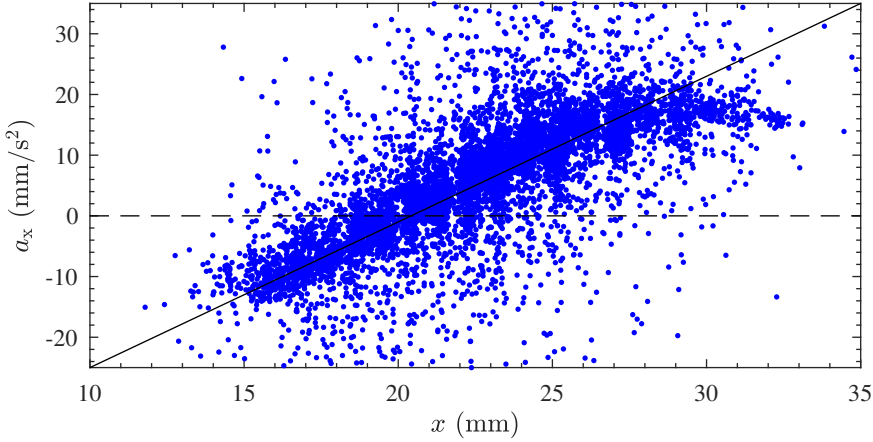


Figure 4.11: Scatter plot of the horizontal acceleration a_x as a function of the first x position for the case without plasma and $E = 0 \text{ V m}^{-1}$. The figure shows the combined data of three separate experiments consisting in total of 7791 particles. A solid line is added to illustrate the a_x dependence on x and a dashed line to indicate the zero-crossing.

was directed outwards, negative for $x \lesssim 20$ mm and positive for $x \gtrsim 20$ mm. Yet, some particles had a velocity directed away from the center of the tube. This can be explained by the fact that some particles were detected for the first time below the symmetry axis of the electrodes (see Figure 4.3), where the flow was spreading out again.

In Figure 4.12, the horizontal acceleration is shown as a function of the electric field E . While the measured acceleration provides information about the local charge between the electrodes, the horizontal velocity provides information about the charge in a larger region of the shielded SPA through the integrated effect of the electric field above and between the electrodes. Consequently, the integrated trend of the particle charge is better observed in the velocity which is therefore used in the analysis of the charge control.

Current received by electrodes

A key point when it comes to charge control is the confirmation that the presence of the mesh grid and the electrodes attracted ions from the sheath above the mesh grid into the shielded SPA. In fact, the mesh grid caused the ions to be focused in the region below. This effect is well known in the literature and is extensively used for plasma-based ion sources [152, 153]. More specifically, the chosen geometry created a vertical DC electric field between the electrodes and the grounded mesh grid (see Figure 4.2). This vertical electric field most likely attracted ions from the sheath into the shielded SPA. Due to the presence of the horizontal field between the electrodes, the plasma species likely gained a non-uniform spatial distribution in a horizontal

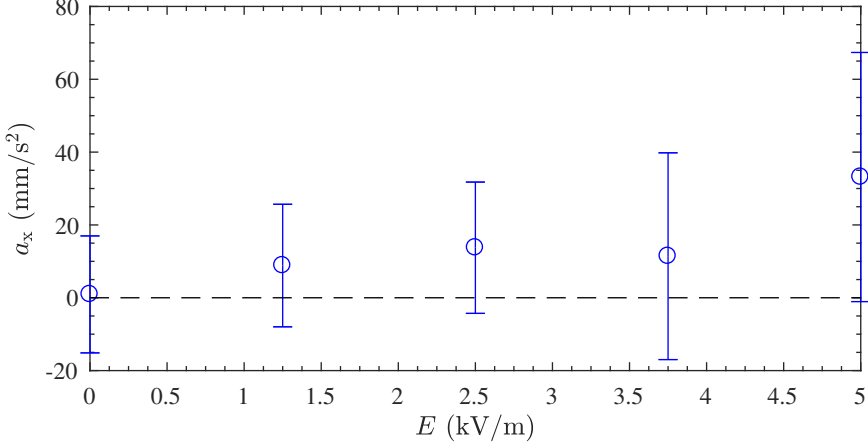


Figure 4.12: Horizontal acceleration a_x as a function of the externally applied electric field E in the shielded SPA. The figure shows the combined data of 10 separate experiments (two for each value of E) consisting in total of 8623 particles.

direction. In order to substantiate this statement, the current going to both electrodes was measured separately in a floating configuration (see subsection 4.3.3) and the results are shown in Figure 4.13.

It is clear from this graph that the anode current exceeded the cathode current up to a field strength of approximately 4.5 kV m^{-1} , after which the cathode current exceeded the anode current. This trend matched the observed trend in horizontal velocity as a function of E (see Figure 4.7). Assuming that the anode current was mostly caused by the electrons and the cathode current by ions, Figure 4.13 indicates that the local ion density was responsible for the charge control of the microparticles. In addition, it can be observed that the anode and cathode current were of the same order of magnitude. Yet, the electron velocity was much larger than the ion velocity, even if both electrons and ions were approximately at room temperature. Thus, assuming that both electrons and ions were collected by the total area of the electrodes, which formed a first order estimate, the ion density likely dominated the electron density according to $n_i/n_e \approx v_e/v_i \propto m_i/m_e$, where m_e is the electron mass.

The ion density was estimated under the presented assumptions using $n_i = I_c / Av_{d,i}e = 10^{11} \text{ m}^{-3}$. Here, A was the cathode surface area and $v_{d,i}$ the ion drift velocity. For the estimation of n_i the cathode current at $E = 1 \text{ kV m}^{-1}$ was used. The estimated ion density of $n_i = 10^{11} \text{ m}^{-3}$ means that the linearised Debye length was in the sub cm range and in the same order of magnitude as the diffusion length [127, 128], which was given by $D/2\pi \approx 2 \text{ cm}$, assuming an infinitely long square beam. Hence, the interaction strength between ions and electrons was decreased and, thus, the plasma species were no longer bound by ambipolar diffusion [154, 155]. This in turn altered the electron and ion current arriving at the particle surface and, consequently, the particle charge. As stated in the introduction, Couédel et al. [56] have shown that the manner in which the transition from ambipolar to free diffusion takes place influences the

particle charge. Overall, the current measurement presented here confirmed our earlier statement that an electric field-induced altering of the local ion density is responsible for the charge control.

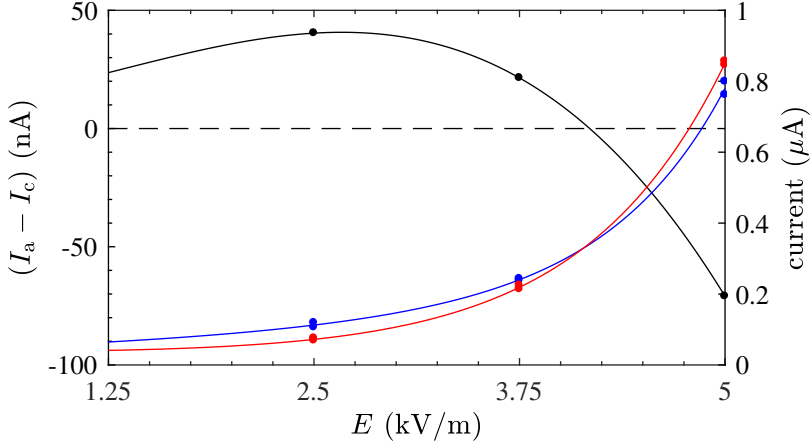


Figure 4.13: In black, the difference between the anode and the cathode current as a function of the applied electric field E . In addition, the individual anode and cathode current are plotted in blue and red respectively. For each value of E the current has been measured twice in separate experiments which is indicated by two points for both currents at each E value in the plot. Fit curves are solely added in the figure to guide the eye.

Ion drag

It has been shown in the previous section that ions dominate the shielded SPA region. What follows, therefore, is a discussion of the possible influence of the ion drag force on the horizontal velocity. For 90 Pa argon, the ion drag force has been described by the linear plasma response formalism which took ion-neutral collisions into account. However, ion absorption at the particle surface was neglected [16, 103]. Using the formalism for a flowing plasma [102], the electric field-induced velocity component of the ions was included in the estimate of the ion drag. First, it can be concluded that the ion drag force is approximately a factor 10 smaller than the electric force on a microparticle with a charge of $1e$ when $n_e < 1 \times 10^{13} \text{ m}^{-3}$ and assuming $T_e < 1 \text{ eV}$ and $E = 1 \text{ kV m}^{-1}$. Second, it can be concluded that, according to the linear plasma response formalism, the ion drag force scales linearly with the ion velocity and can consequently not explain the measured change in v_x as a function of E . Hence, these two arguments show that the ion drag force proved negligible in the shielded SPA.

Asymmetric ion distribution

If free ions and electrons were present in the shielded SPA, it would be expected that these free charge carriers were non-uniformly distributed between the electrodes in the

presence of an electric field. In that case, the charge of the particles and, consequently, their velocity, should also depend on their position. This very effect can be observed in Figure 4.14, where the mean value and standard deviation of v_x are plotted for all positions with the data grouped in spatial bins of 1 mm. It is clear that the velocity had a maximum negative value close to the anode which increased with the distance to this electrode, eventually becoming positive near the cathode. This situation corresponds to the expected distribution of charge carriers: more electrons at the anode and more ions at the cathode. Consequently, the particles experienced an increased positive ion flux near the cathode, while they remained negatively charged close to the anode. In conclusion, the asymmetric velocity distribution fully corroborates that a free positive space charge in the shielded SPA was the dominant reason for the observed charge control.

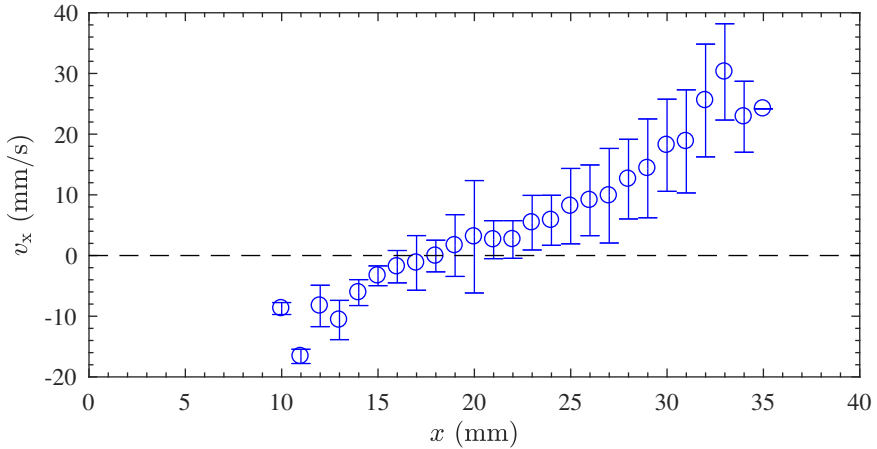


Figure 4.14: Horizontal velocity v_x as a function of the first x position for $E = 5 \text{ kV m}^{-1}$ and a plasma power of 6 W. The figure shows the combined data of two separate experiments consisting in total of 1244 particles. The corresponding data is averaged in spatial bins of 1 mm in size.

4.6 Conclusion

In this chapter, we have shown that the charge of microparticles can be controlled by shielding the spatial plasma afterglow from the bulk plasma through the application of a mesh grid and by changing an externally applied electric field strength below this mesh grid. In this manner, the particle charge has been controlled from small negative to small positive charges, typically in the range of $Q = \pm 10 e$, by varying the local ion space charge distribution in the shielded spatial plasma afterglow. The governing mechanism for this variation in ion density is the vertical electric field component arising from the geometry of the setup. These variations in ion density have been confirmed by measurement of the separate currents received by each of the electrodes,

which generated the external electric field, and by the asymmetric distribution of the horizontal velocity v_x as a function of the horizontal distance x . The strength of the reported technique is that the actual control was achieved in the shielded spatial plasma afterglow, while the particles reached a constant equilibrium charge in the other regions above the mesh grid.

The achieved control of the particle charge not only opens up ways to study nanoscale surface charging physics on micrometer length scales and fundamental plasma-plasma-particle interactions, it also contributes to the further development of plasma-assisted contamination control strategies.

Charge neutralisation of microparticles by pulsing a shielded spatial plasma afterglow

Abstract

In this chapter, it is shown that microparticles can be effectively neutralised in the (spatial) plasma afterglow of an inductively coupled plasma. A key element in the reported experiments is the utilisation of a grounded mesh grid separating the plasma bulk and the “shielded” plasma afterglow. Once particles - being injected in and charged by the inductively coupled plasma - had passed this mesh grid, the plasma was switched off while the particles continued to be transported under the influence of both flow and gravity. In the shielded spatial plasma afterglow region, the particle charge was deducted from their acceleration in an externally applied electric field. Our experiments demonstrate that all particles were neutralised independently of the applied electric field magnitude. The achieved neutralisation is of primary importance for the further development of plasma-assisted contamination control strategies as well as for a wide range of other applications, such as colourimetric sensing, differential mobility analysers, and medical applications.

This chapter is accepted for publication:

B. van Minderhout, J.C.A. van Huijstee, A.T.A. Peijnenburg, P. Blom, G.M.W. Kroesen and J. Beckers (2021), “Charge neutralisation of microparticles by pulsing a low-pressure shielded spatial plasma afterglow” *Plasma Sources Science and Technology*, <https://doi.org/10.1088/1361-6595/abd81f>

5.1 Introduction

The charge of nano- and microparticles is a key parameter in many processes in various research fields. In dusty or complex plasmas, i.e. plasmas containing nano- to micrometre-sized particles, microparticles typically acquire a permanent negative charge of $(10^3 - 10^4)$ elementary charges in the plasma bulk [123,148]. Under these conditions, the particle charge is determined by the balance between ion and electron fluxes reaching the particle's surface. Since the electrons are much more mobile than ions, an equilibrium in flux is achieved for a negative surface potential and, thus, for a negative particle charge. This negative charge drives many elementary processes such as ion drag [16, 17], local Debye shielding [18] and Coulomb-interactions in strongly coupled plasmas [19, 20]. Also, during the plasma-assisted growth process of nanoparticles, the negative particle charge is a key parameter [21–24]. However, for some processes, neutral or even positively charged particles are required, which is illustrated by the following three examples.

First of all, the aggregation of gold nanoparticles (GNPs) is frequently used in colourimetric sensing [45–48]. Adding salt is a common method to induce aggregation. Yet, the salt-induced aggregation by charge screening is a slow process that makes quantitative and reproducible measurements difficult when the GNPs are charged [49]. Zhang et al. have recently reported that charge neutralisation of the GNPs improved detection time, signal stability, and sensitivity of the colourimetric sensing method [49].

Second, nanoparticles (NPs) are intensively tested for use in medical products, especially in imaging and drug delivery [41–43]. It has been shown that a positive surface charge of the NPs improves the efficacy of imaging, gene transfer, and drug delivery [44]. Yet, positively charged NPs also have higher cytotoxicity. These examples show that the charge of NPs is a crucial parameter for the application in medical products and that it benefits from being accurately controlled.

Third, in the field of aerosol science, differential mobility analysers (DMAs) are used to accurately measure the particle size distribution [156]. The DMA is a powerful technique on the condition that the initial particle charge distribution is known. Therefore, considerable efforts are put in the neutralisation of particles in the field of aerosol science [157–160], which recently led to the development of sophisticated models [161, 162].

The three examples discussed above show that neutral particles are of the utmost importance for processes in numerous research fields. Besides the three applications discussed above, this research is primarily driven by the development of contamination control strategies [13]. In many ultra-clean low-pressure systems, such as in the major semiconductor industry [50], contamination by particles has become an increasingly urgent challenge. Plasma-based techniques have a high potential for preventing particle contamination since plasmas can simultaneously charge the contaminating particles and alter their trajectories by the plasma-induced electric fields [51].

Crucial in the neutralisation method reported in this chapter is the pulsed Spatial Plasma Afterglow (SPA) and the presence of a mesh grid shielding the active plasma region from the afterglow. In the afterglow, where the plasma is not actively powered, the typical particle charge is significantly lower than in the previously discussed plasma

bulk [52, 53, 133]. Most research has focused on the temporal afterglow, where the particle charge is determined by the plasma changes in time [52–59]. In the largely unexplored SPA, the particle charge is determined by the spatial evolution of plasma parameters. These parameters evolve differently in the spatial and temporal plasma afterglow, which directly affects the particle charge. For example, Couëdel et al. have shown that the particle charge is determined by how the transition from ambipolar to free diffusion takes place [56].

In previous work, we have measured the charge of microparticles in the free and shielded SPA [133, 163] (see chapter 3 and chapter 4). The shielded SPA is created by the application of a mesh grid in the setup’s cross-section separating the active plasma region from the SPA. In the latter situation, the particle charge was controlled from ~ -40 to $+10$ elementary charges by variation of the external electric field strength [163]. Note that in those experiments, the used inductively coupled plasma (ICP) was powered continuously.

In this chapter, we report neutralisation of microparticles in the shielded SPA by switching off the plasma discharge after all particles were below the mesh grid. Spatially resolved particle charge measurements confirmed the neutralisation of the particles. The local charge was obtained by segmentation of the trajectories and by measuring the local particle acceleration in the region of an externally applied electric field.

The following section deals with the plasma decay timescale together with the particle charging theory, followed by an overview of the experimental setup in section 5.3. The experimental procedure differs in two aspects from previous work: the pulsing of the plasma discharge and the segmentation of the particle trajectories to measure spatially resolved the charge and decharging. Section 5.4 presents the charge neutralisation results, while section 5.5 discusses the charge evolution in the SPA up to the moment that the plasma was switched off. Finally, several mechanisms are proposed that could explain the relevant results.

5.2 Theory

This section first offers a brief discussion of the theory of plasma decay in the temporal afterglow. The particle charge evolution as a function of the particle position was a highly dynamic process in the reported experiments, where the particle charge varied by approximately three orders of magnitude. The latter evolution is examined in section 5.5, which addresses the equilibrium charge particles obtained in the plasma bulk and the corresponding particle charging timescale.

5.2.1 Plasma decay

For the conditions in this study, the loss of plasma is determined by (ambipolar) diffusion to the walls and by subsequent recombination. While, due to the low pressure, volume recombination processes were negligible, the low microparticle density ($n_d \approx 10^6 \text{ m}^{-3}$) ensured that recombination at the surface of the particles could be neglected as well.

The density decay as a function of time due to diffusion and successive wall recombination can be described by $d\tilde{n}/dt = -\tilde{n}/\tau_L$, where $\tilde{n} = n_{e,i}/n_0$ with $n_{i,e}$ the momentary plasma density and n_0 the initial plasma density. In addition, τ_L is the timescale of diffusive plasma loss which is given by [164]

$$\tau_L = \frac{\Lambda^2}{D_a} = \frac{3\Lambda^2}{\lambda_{ia}v_{th,i}} \frac{1}{(1+\tilde{T})} = \frac{2}{(1+\tilde{T})} \tau_L^\infty. \quad (5.1)$$

Here, Λ is the characteristic diffusion length, D_a the ambipolar diffusion coefficient, $v_{th,i}$ the thermal speed of the ions and λ_{ia} the ion mean free path. Furthermore, $\tilde{T} = T_e/T_i$ where T_e and T_i are the electron and ion temperatures, and τ_L^∞ is the asymptotic value of the plasma decay time.

Equation 5.1 is only valid as long as the plasma decay is governed by ambipolar diffusion and successive wall recombination. When the electron Debye length $\lambda_{De} > 0.1\Lambda$, ions and electrons no longer diffuse together [155]. Experiments [154, 165] and a theoretical study [166] have shown that during the transition from ambipolar to free diffusion, the diffusion and recombination rate initially increases since the ions are accelerated by the “escaping” electrons. When the ions can no longer follow, the diffusion of the ions becomes slower than that of the electrons, i.e. the diffusion of ions approaches the free diffusion limit [154, 165, 166].

5.2.2 Particle charging

As stated in the introduction, particles generally acquire a permanent negative charge in the bulk of a low-pressure plasma [123]. In many cases, the acquired charge is described by the Orbital Motion Limited (OML) theory, which assumes that the electrons and ions are collected by the particles when their orbits overlap the particle surface [123, 145]. Furthermore, OML theory assumes that the electrons and ions have collisionless orbits.

For higher pressures, the ions collide with neutrals within the plasma sheath surrounding the particle. However, Khrapak and Morfill [16] and Khrapak et al. [80] have shown that in plasma discharges these collisional effects only change the particle charge by a maximum factor of three compared to the OML predicted value for microparticles. Accordingly, ion collisions within the sheath are omitted in the analysis of this study.

For an isolated particle with radius $r_p \ll \lambda_{De}$ in an electropositive plasma containing Maxwellian energy-distributed electrons, the ion current I_i and the electron current I_e are given by [79]

$$I_{i,e} = \begin{cases} I_{i0,e0} \left(1 - \frac{q_{i,e}\phi_s}{k_B T_{i,e}}\right) & \text{if } q_{i,e}\phi_s \leq 0 \\ I_{i0,e0} \exp\left(-\frac{q_{i,e}\phi_s}{k_B T_{i,e}}\right) & \text{if } q_{i,e}\phi_s \geq 0. \end{cases} \quad (5.2)$$

The currents are determined by the surface potential of the particle ϕ_s , the temperature $T_{i,e}$ and the charge $q_{i,e}$ of the ions and electrons. Furthermore, k_B stands for the Boltzmann constant and $I_{i0,e0}$ for the current collected at $\phi_s = 0$. By considering the particle as a capacitor, it follows that the particle charge Q is given by

$$Q = 4\pi\epsilon_0\epsilon_r r_p \phi_s \quad (5.3)$$

where ϵ_0 and ϵ_r are the respective vacuum and relative permittivities.

In addition, the characteristic time to reach the equilibrium charge, the so-called particle charging timescale τ_c , can be derived using the OML formalism as being [125]

$$\tau_c = \frac{4\epsilon_0}{e^2} \sqrt{\frac{k_B T_i \pi m_i}{8}} \frac{1}{r_p n_{e,i} (1 + y_0)}. \quad (5.4)$$

Here, e is the elementary charge of an electron, m_i the ion mass and y_0 the equilibrium value of the reduced particle potential $y = e\phi_s/k_B T_e$. Equation 5.4 is valid in the usual situation for low-pressure plasmas where $T_e \gg T_i$.

5.3 Experiment

In this section, the experimental setup is only summarised since it has been extensively described in our previous publications [133, 163] (see chapter 3 and chapter 4). Compared to our earlier study, two differences in the experimental procedure are treated in more detail: the pulsing of the ICP and the segmentation of the particle trajectories to obtain the spatially resolved particle charge.

5.3.1 Setup

The experiments were performed in a vacuum system consisting of - amongst other components - a 1 m long square glass tube with an inner width of $D = 0.1$ m. The vacuum system is called the Plasma Particle Charging Investigation (PPCI) setup [133], a sketch of which is shown in Figure 5.1. At the top, a shower head was mounted which regulated both the 10 sccm flow and the particle injection. These particles, $4.9 \pm 0.2 \mu\text{m}$ in diameter, consisted of a melamine-formaldehyde (MF) core and a porous silver coating with a thickness of ~ 100 nm to minimise triboelectric charging effects [141]. The operating pressure was 90 Pa argon (at a background pressure of 10^{-9} Pa). In addition, the flow combined with gravity accelerated the particles to a measured settling velocity $v_{p,f} = 0.13 \text{ m s}^{-1}$ [163].

A square coil wound around the outside of the tube generated an inductively coupled plasma at 13.56 MHz. Hereby, 6 W of power was delivered to the plasma volume. The active plasma region was shielded from the remainder of the setup through application of a grounded mesh grid placed in the cross-section of the tube downstream of the ICP. This mesh grid consisted of 0.37 mm thick wires with a spacing of 1.13 mm between two wires. The area below the mesh grid will be referred to as the shielded SPA.

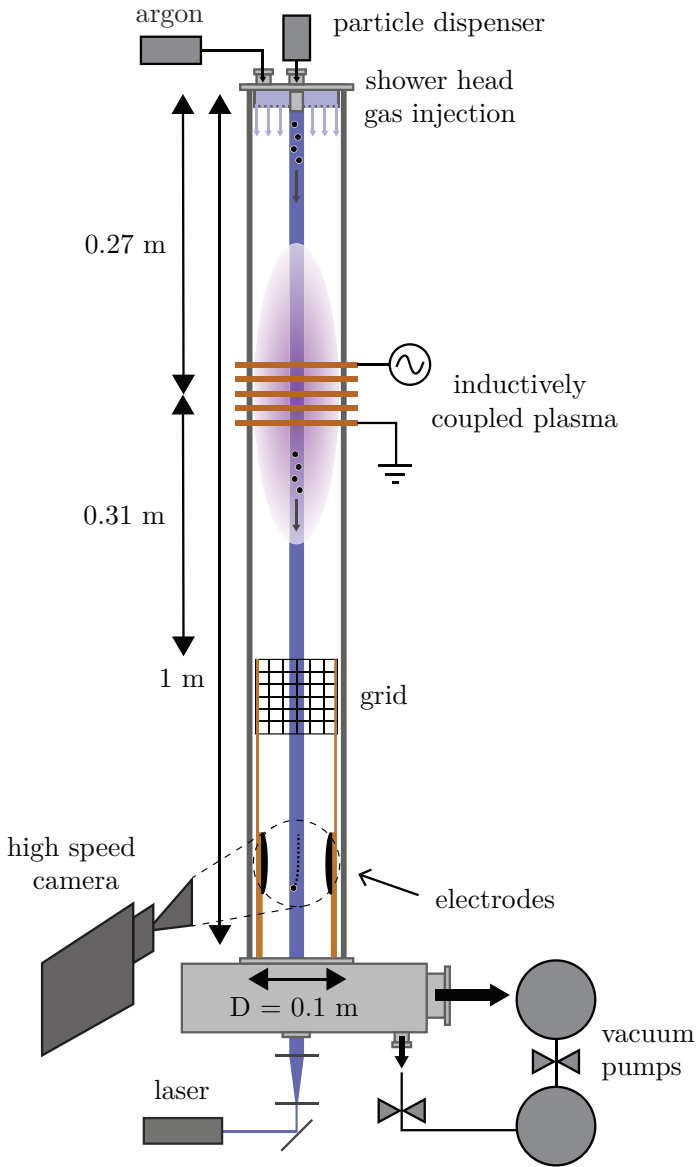


Figure 5.1: Sketch of the PPCI setup in which microparticles (injected at the top) travelled through the active plasma discharge and the shielded SPA region, of which the latter is created by utilisation of a grounded mesh grid. The mesh grid was placed in the cross-section of the tube. After the particles were positioned below the mesh grid in the shielded SPA, their charge was measured by accelerating in an external electric field. (Figure from [163].)

In the shielded SPA, the charge neutralisation of the particles was verified by measuring the position, velocity and acceleration of the microparticles in an externally applied electric field created by two parallel and vertically aligned Rogowski electrodes [115]. These electrodes were 70 mm in diameter and had a separation distance of 40 mm. The electric field profile, generated by applying a potential difference across the two electrodes, was simulated in COMSOL using a 2D electrostatic model of which the result is shown in Figure 5.2. Subsection 5.3.2 contains an explanation of how the neutralisation was measured using this electric field strength simulation. Moreover, the breakdown electric field between the electrodes was experimentally measured to be $E_{\text{bd}} = 8 \text{ kV m}^{-1}$ while the plasma discharge was switched on. This breakdown field is much higher than the maximum electric field (5 kV m^{-1}) used in the presented experiments. Consequently, possible reionisation had a negligible effect on the particle charge and additional plasma shielding.

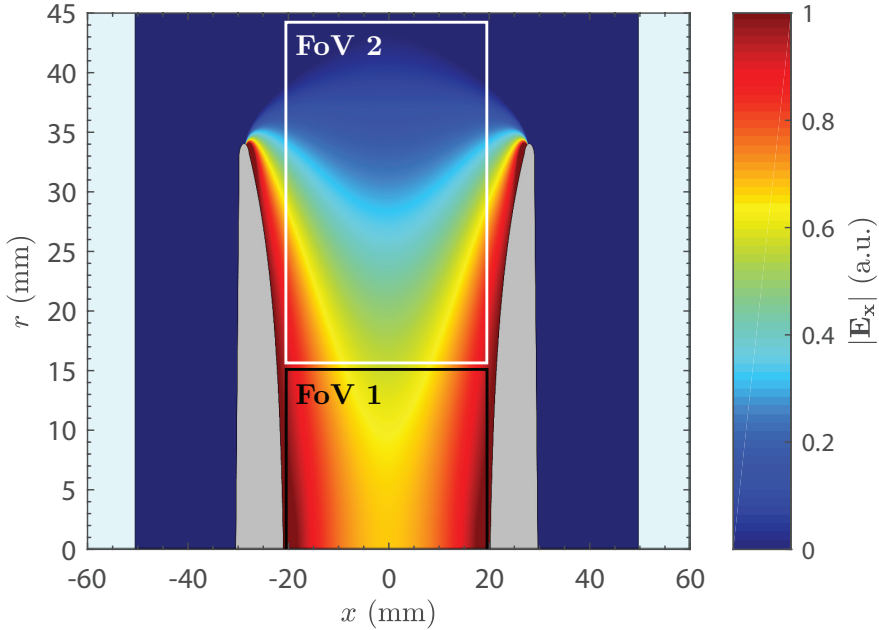


Figure 5.2: Plot of the simulated normalised horizontal electric field component created by the Rogowski electrodes. Cylindrical geometry was assumed in the simulation, where the x -axis was the axis of symmetry. Therefore, the glass plates in the front and at the back of the electrodes were not included. Indicated in grey are the electrodes, in light blue, the glass tube and in black and white the two camera positions. FoV 1 corresponds to the camera focused on the central region of the electrodes and FoV 2 to the camera focused on the top part of the electrodes. (Figure adapted from [163].)

The particles were illuminated by a laser system (central wavelength 447 nm), and their scattered light was recorded by a high-speed camera focused on the region between electrodes. As shown in Figure 5.1, this laser sheet was vertically directed and had a thickness of 3 mm. This thickness assured that particles moving towards or away from the camera, i.e. particles travelling parallel with the viewing direction, were only briefly imaged and thereby omitted in the analysis. The camera's field of view (FoV) was approximately 40 mm in the horizontal and 32 mm in the vertical direction, with a resolution of approximately 32 μm per pixel. The particle density ($n_d \approx 10^6 \text{ m}^{-3}$) in our experiments was low so that, typically, 10 – 100 particles were imaged simultaneously and therefore did not mutually interact.

To obtain information about the particle charge, each particle's position, velocity and acceleration were retrieved using in-house developed particle tracking software. More details about the setup and the developed software can be found in our previous work [163] (chapter 4). Furthermore, it was illustrated that the plasma afterglow did not influence the electric field distribution at the position of the electrodes in the case of a free SPA [133]. The experiments reported here are performed in the shielded SPA where the density was even lower than that in the free plasma afterglow. It can be thus be concluded that the afterglow did not influence the distribution of the externally applied electric field.

5.3.2 Procedure

This section discusses the experimental procedure of performed experiments. First, the pulsing of the plasma discharge is elaborated upon. Second, the spatially resolved particle charge measurements are treated.

Pulsing of the ICP

The charge neutralisation experiments have been performed using a pulsed ICP. The plasma was switched off after all particles were below the mesh grid, as indicated by the four sketches in Figure 5.3 showing the situation with plasma switched on for $t < 0$ s, and plasma switched off for $t = 0$ s, $t = 1$ s and $t = 2$ s. Note that the particles travelled from the mesh grid to the electrodes in ≈ 2 s and consequently, at $t = 1$ s, they resided in the middle between mesh grid and electrodes. In the sketch, the active plasma region is indicated in purple and the shielded SPA in blue. The sketch for $t = 0$ s corresponds to the situation just after the plasma was switched off, with the decaying plasma not indicated in this sketch. As explained in the theory (subsection 5.2.2), the typical plasma decay time can be calculated using Equation 5.1. For the geometry of the PPCI setup, the diffusion length Λ was given by $D/2\pi \approx 2$ cm where the glass tube was assumed to be an infinitely long square tube [127, 128]. Hence, the asymptotic value of the plasma decay timescale was $\tau_L^\infty = 30$ ms. Only particles detected between $t_p = (0.5 - 1.6)$ s after the plasma was switched off were used in the analysis. After $t_p = 1.6$ s, no particles were detected as a consequence of the injection method. Since $t_p \gg \tau_L^\infty$, it can be assumed that the plasma had fully decayed at the moment the particle charge was measured, although in the transition

from ambipolar to free diffusion, the plasma decay briefly slowed down (as explained in subsection 5.2.1).

Due to the injection method, not all particles were injected simultaneously and were, accordingly, spread out in space vertically, as indicated in Figure 5.3. Hence, the individual particles travelled through a different shielded SPA depending on their position when the plasma was switched off, as illustrated in Figure 5.4. These sketches indicate the different spatial plasma distribution through which particles detected at $t < 0$ s, $t = 0$ s, $t = 1$ s and $t = 2$ s have travelled, before being imaged in the central region between the electrodes. The particles travelled in ≈ 2 s from the mesh grid to the electrodes.

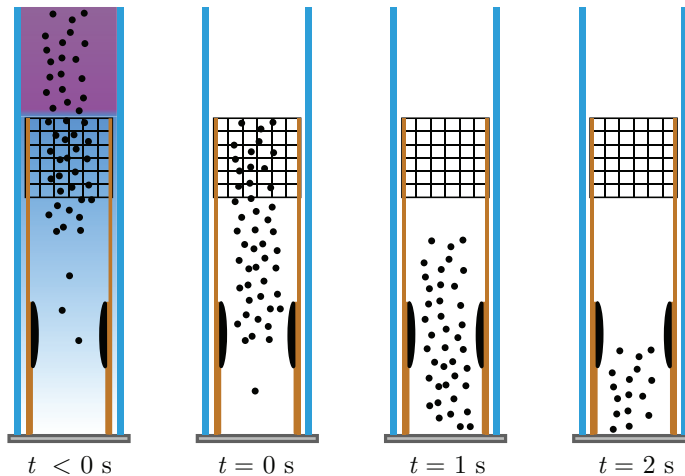


Figure 5.3: Schematic drawing of the plasma and its shielded SPA at four moments in time. The ICP is switched off when all particles were located below the mesh grid. This moment is referred to as $t = 0$ s. After approximately 2 s, the last particles resided between the electrodes. The decaying plasma is not indicated in the sketch for $t = 0$ s.

As indicated in the sketch of Figure 5.4 for $t < 0$ s, particles detected before the plasma was switched off travelled through the complete shielded SPA. The sketch for $t = 1$ s depicts the shielded SPA through which the particles detected at $t = 1$ s travelled. The particles resided roughly in the middle between the mesh grid and the top of the electrodes when the plasma was turned off (see the sketch for $t = 1$ s of Figure 5.3). Accordingly, they travelled solely through the upper part of the shielded SPA. It is obvious that the particles detected at $t = 2$ s after the plasma was switched off travelled through a plasma free region below the mesh grid as indicated in the sketch for $t = 2$ s of Figure 5.4.

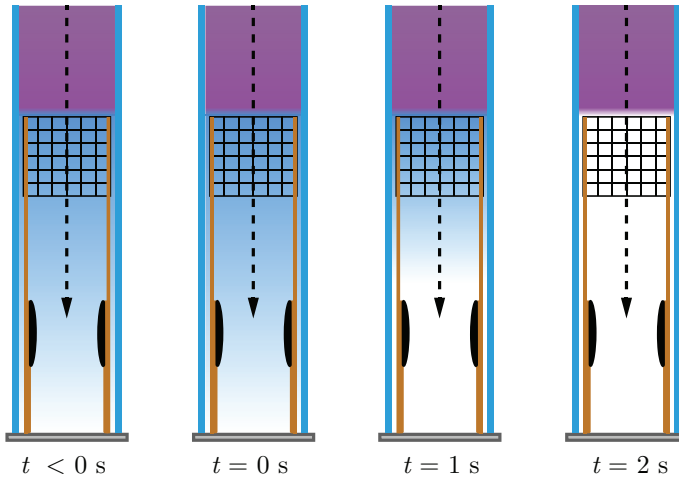


Figure 5.4: Schematic drawing of the plasma configuration and its afterglow experienced by the particles that were detected at four different times. The particle trajectories are indicated by a dashed line. Where Figure 5.3 shows the plasma configurations at different times, the respective sketches indicate the plasma distribution experienced by the particles detected at the given time when they travelled through the shielded SPA.

Local charge measurement

Where in previous work [133, 163] (see chapter 3 and chapter 4) the particle charge was determined from the full particle trajectories, the trajectories in this study were segmented. The segments were 5 mm long in a vertical direction and consisted of (20 – 38) particle positions. For each segment, a local fit was made to obtain the local velocity and acceleration. The fitting procedure was similar to the one used in our previous work [163] (see chapter 4). Also, in this current study, the experiments were performed with two different camera positions, as indicated in Figure 5.2. In this way, the velocity and acceleration were measured with a spatial resolution of 5 mm over a range of 50 mm.

To obtain the local charge for each trajectory, the segment-averaged electric field was calculated using the performed electrostatic simulation (see Figure 5.2). The non-uniformity of the electric field was, thereby, taken into account. In this study, both the local charge and the trajectory-averaged charge were obtained and, labelled by subscripts l and f respectively.

5.4 Results

This section presents and discusses the spatially resolved particle charge measurements, thereby revealing the neutralisation that has taken place.

In Figure 5.5, the vertical position y is plotted versus the local horizontal accel-

ation $a_{x,1}$. The plasma discharge was switched off after all particles were below the mesh grid, as treated in the previous section. In Figure 5.5, $y = 0$ corresponds to the centre position between the electrodes, and positive y is defined as the region above the electrodes. As indicated in the caption of the figure, $a_{x,1}$ is plotted for three different electric field strengths. Particles measured at different times are combined and thereby averaged. The time trend observed in $a_{x,1}$ is treated in appendix subsection 5.7.3. Note that the bars around the data points do not demonstrate an error but rather the spread, as will be elaborated further upon in this section.

It is clear that independent of the electric field strength, $a_{x,1}$ became approximately zero at $y = 30$ mm. Since the electric force was dominant in the horizontal direction, the trend in $a_{x,1}$ shows that the microparticles were neutralised as they moved through the final stage of the SPA.

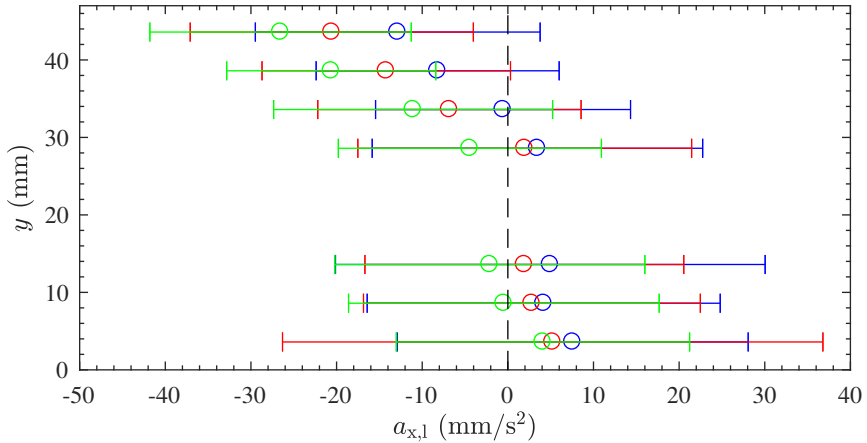


Figure 5.5: Plot of the vertical position y as a function of the local horizontal acceleration $a_{x,1}$ for three different electric field strengths: blue $E = 1.25 \text{ kV m}^{-1}$, red $E = 2.5 \text{ kV m}^{-1}$ and green $E = 5.0 \text{ kV m}^{-1}$. The graph shows the combined data of two different camera positions as explained in subsection 5.3.2. For each electric field strength at least two separate measurements have been combined for each camera position resulting in the following number of full particle trajectories: $E = 1.25 \text{ kV m}^{-1}$ 461 in FoV1 and 233 in FoV2, $E = 2.5 \text{ kV m}^{-1}$ 253 in FoV1 and 153 in FoV2 and $E = 5.0 \text{ kV m}^{-1}$ 202 in FoV1 and 160 in FoV2. The given electric field strength corresponds to the value in the centre of the electrodes.

In the remainder of this section, three observations from Figure 5.5 are briefly discussed. The detailed description and the corresponding data of each observation can be found in the appendix of this chapter. The section concludes with a presentation of the local particle charge results.

First of all, it is apparent that $a_{x,1}$ for $y = (0 - 30)$ mm has a slightly higher value for $E = 1.25 \text{ kV m}^{-1}$ compared to the trends for $E = 2.5 \text{ kV m}^{-1}$ and $E = 5 \text{ kV m}^{-1}$. This was caused by the displacement of the particles in the region above the electrodes ($y > 35$ mm) due to the electric field present. Accordingly, the particles were most

centred for $E = 5 \text{ kV m}^{-1}$ and least centred for $E = 1.25 \text{ kV m}^{-1}$. Since the flow was compressed at the position of the electrodes, the off-centre particles (i.e. $x \neq 0 \text{ mm}$) obtained a small horizontal acceleration, which explains the observed difference in $a_{x,1}$ for the three electric field strengths. In the appendix subsection 5.7.1, this effect has been explained in more detail with the corresponding graphs.

For $y = (35 - 45) \text{ mm}$ the measured $a_{x,1}$ was not influenced by the same effect since the particles were not yet displaced at these positions (see appendix subsection 5.7.1). To draw conclusions from the difference in $a_{x,1}$ in this region, we needed to take into account the difference in the local electric field. The end of section 5.5 will show that the electric field strength most likely influenced the initial charge.

Second, and as already mentioned, it should be noted that the bars around the data points do not demonstrate an error but rather the spread indicated by the one-sigma interval. Remarkably, the spread in $a_{x,1}$ proved constant for all electric field strengths. It was expected to scale with the electric field strength as discussed in our previous publication [163]. The observed constant spread was caused by the local flow profile at the position of the electrodes, as is elaborated upon in appendix subsection 5.7.2.

Third, the local acceleration is not plotted in Figure 5.5 for $y = (15 - 25) \text{ mm}$ since too few detected particles existed at these positions. This effect was predominantly caused by particles moving out of the laser sheet volume. Hence, the trajectories of the particles ended before they reached the bottom of the FoV. The relevant data and the full explanation are elaborated in appendix subsection 5.7.3.

While the trend for $a_{x,1}$ presented in Figure 5.5 gives useful insights into particle neutralisation, the neutralisation is most clearly presented by the spatially resolved particle charge Q as shown in Figure 5.6. The charge Q was obtained from $a_{x,1}$ by taking into account the non-uniform electric field, as explained in subsection 5.3.2. First and foremost, the trend in Q shows that the particles neutralised independently of the electric field strength, i.e. the particle charge reached a constant value of zero.

Moreover, it is clear that the spread in Q decreased as the electric field strength increased. As explained in the second point of this section (and in appendix subsection 5.7.2), this was caused by the constant flow-induced spread in $a_{x,1}$. Furthermore, it is apparent that the particle charge at the top of FoV1 ($y = 43 \text{ mm}$) was most negative for the smallest electric field strength $E = 1.25 \text{ kV m}^{-1}$ and increased for higher values of E . This trend seems to correspond with the particle charge control described in our previous work [163] (see chapter 4). Yet, in the current situation, not all particles have travelled through the entire shielded SPA, since the plasma discharge was switched off after all particles were located below the grid. In addition, in the final stage after the plasma discharge was switched off, the ion and electron fluxes to the particles were altered making a direct comparison impossible.

Our findings are consistent with the studies reported by Chen et al. [167, 168]. The authors have measured the charge of plasma-synthesised nanoparticles (NPs) in the shielded SPA using a continuously powered plasma flow tube reactor. A bipolar charge distribution of singly charged NPs was found, from which it was concluded that most NPs were probably neutralised in the SPA [168]. Our spatially resolved particle charge measurements confirm that is indeed likely that most NPs were neutralised.

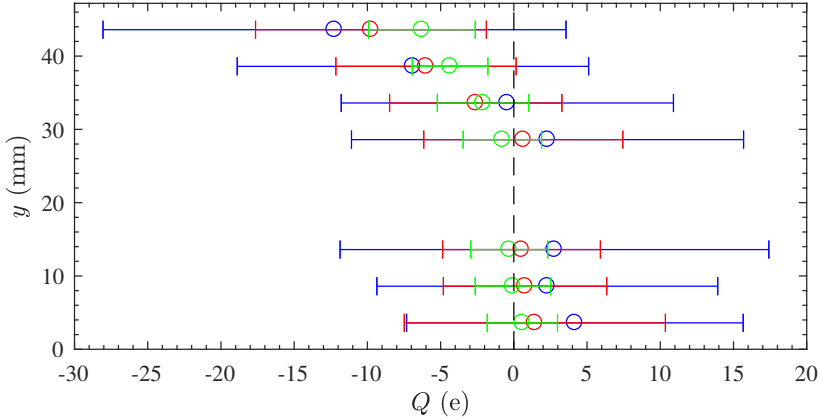


Figure 5.6: Plot of the vertical position y as a function of the particle charge Q for three different electric field strengths: blue $E = 1.25 \text{ kV m}^{-1}$, red $E = 2.5 \text{ kV m}^{-1}$ and green $E = 5.0 \text{ kV m}^{-1}$. For each electric field strength at least two separate measurements have been combined for each camera position resulting in the following number of full particle trajectories: $E = 1.25 \text{ kV m}^{-1}$ 461 in FoV1 and 233 in FoV2, $E = 2.5 \text{ kV m}^{-1}$ 253 in FoV1 and 153 in FoV2 and $E = 5.0 \text{ kV m}^{-1}$ 202 in FoV1 and 160 in FoV2. The given electric field strength corresponds to the value in the centre of the electrodes.

5.5 Physical interpretation

As shown in section 5.4, the particle charge was successfully neutralised in the pulsed SPA independently of the externally applied electric field. The exact mechanisms responsible for the reported neutralisation are not fully understood. In this section, possible mechanisms are discussed, including neutralisation by (trapped) ions, photo-detachment and charge exchange reactions that could, possibly combined, account for the observed neutralisation. First, the evolution of the particle charge through the active plasma region and the sheath above the mesh grid has been summarised for overview. A more detailed description can be found in our previous work [163] (see chapter 4).

Particle charge evolution up to the electrodes

Initially, the microparticles were triboelectrically charged upon particle injection. Then, in the active plasma region, the particles acquired a negative charge of roughly $Q_p = -5 \times 10^3 e$, which is described by OML theory (see subsection 5.2.2). Since the time the particles resided in the active plasma region was much larger than τ_c (see Equation 5.4), all particles reached the equilibrium charge. After the active plasma region, the particles discharge in the sheath above the mesh grid due to the local electron depletion. It is estimated that the particle charge after travelling through the sheath had decreased to $Q_s = -(10^2 - 10^3)$ elementary charges [163].

5.5.1 Neutralisation by (trapped) ions

The initially negatively charged particles might have been partially discharged in the shielded SPA by (trapped) ions arriving at the particle surface. Yet, this process is not very likely to have played a dominant role in neutralisation because of two distinct reasons. First, the plasma density at the position of the electrodes was estimated in our previous publication [163] to be $n_{e,i} \approx 10^{11} \text{ m}^{-3}$ when the plasma discharge was switched on. In this work, the particle charge was measured $t > 0.5 \text{ s}$ after the plasma discharge was switched off. Recalling that the typical plasma decay timescale was $\tau_L^\infty = 30 \text{ ms}$ (see subsection 5.2.1 and subsection 5.3.2), it can be concluded that $n_{e,i} \ll 10^{11} \text{ m}^{-3}$ and that, consequently, the trapped ion concentration was negligible [169]. Second, the applied electric field between the electrodes was at maximum 5 kV m^{-1} , while the measured breakdown field strength of 8 kV m^{-1} proved much larger. Therefore, reionisation could have not occurred in the region where the neutralisation took place. In conclusion, (trapped) ions most likely have not neutralised the particles since far too few ions were present locally.

5.5.2 Neutralisation by photodetachment

The laser system used in this research had a photon energy of 2.8 eV , which is below the work function of silver [170]. Hence, it is concluded that photodetachment has likely not contributed to the observed charge neutralisation in this study.

5.5.3 Neutralisation by charge exchange

Another mechanism that could be at play here is resonant charge transfer (RCT) between the microparticles and impurities in the system. RCT reactions can take place as long as the energy levels of the receiving atoms or molecules' excited states lie within the conduction band of the metal [88]. This means that, for the silver-coated particles used in this study, the atoms or molecules should have excited states with energies below 3.7 eV [171]. The latter criterion was satisfied for many molecules such as N_2 , O_2 , H_2O , OH [172]. These species occurred as impurities within the setup and were observed with a residual gas analyser at the base pressure of the PPCI setup (10^{-9} Pa). The process of RCT is, amongst others, determined by the surface state, such as the presence of adsorbates [89], which shows the complexity of RCT. We do not fully understand why the RCT process would stop once the particles are neutralised. This is possibly due to an induced dipole interaction between particle and molecules aiding the RCT, which is, of course, absent for neutral particles. Another possibility would be that the RCT is influenced by the externally applied electric field present in the neutralisation region, similar to the observed lowering of the work function in the case of stainless steel [173]. In conclusion, resonant charge transfer reactions could have played a role in the observed neutralisation.

5.6 Conclusion

In this study, microparticles have been neutralised by switching off the plasma discharge once the particles were located below the mesh grid. This mesh grid shielded the SPA from the active plasma region. In this manner, the initial triboelectric charge has been subsequently reset by the active plasma discharge and the sheath above the mesh grid. The particle charge was measured in the shielded SPA above and between the electrodes. Above the electrodes, the particle charge varied between $Q = -(6 - 12)e$, depending on the applied electric field strength, which influenced the received ion flux. Independent of the applied electric field strength, all particles were neutralised within 15 mm from the start of the detection region.

The observed neutralisation could - in ascending order of certainty - be due to photo-detachment, neutralisation by (trapped) ions and resonant charge exchange reactions. The measured neutralisation is not only crucial for colourimetric sensing [49], differential mobility analysers [159] and many medical applications [44], it also contributes to the further development of plasma-assisted contamination control strategies [13].

5.7 Appendix

In this appendix, the three observations from Figure 5.5 (discussed in section 5.4) are explained in more detail with the corresponding graphs.

5.7.1 Positive acceleration after neutralisation

The first observation was the slightly higher value of $a_{x,1}$ for $y = (0 - 15)$ mm in the situation where $E = 1.25 \text{ kV m}^{-1}$ compared to the trends for $E = 2.5 \text{ kV m}^{-1}$ and $E = 5 \text{ kV m}^{-1}$. This difference in $a_{x,1}$ was caused by a combination of two effects.

First, the particles were displaced by the electric field before they became neutralised. In Figure 5.7, $a_{x,f}$ is plotted versus the horizontal position x of the first moment the particle is detected for $E = 0 \text{ kV m}^{-1}$ and $E = 5 \text{ kV m}^{-1}$. This figure shows the acceleration of the full particle trajectories, i.e. the trajectories are not segmented. Furthermore, the camera was focused on the central region between the electrodes (see Figure 5.2). Figure 5.7 shows that the particles passed the electrodes on the right-hand side of the setup if no electric field was applied (the centre of the setup was at $x = 20$ mm, as indicated by the dashed vertical line). Consequently, the average value of $a_{x,f}$ for $E = 0 \text{ kV m}^{-1}$ was larger than zero. Figure 5.7 illustrates that the particles for the situation where $E = 5 \text{ kV m}^{-1}$ have shifted to the centre, compared to the situation without electric field applied, and accordingly the average value of $a_{x,f}$ was closer to zero.

Second, the curved shaped electrodes caused the flow to be compressed at the position of the electrodes, which influenced the particle trajectories. While particles detected on the right-hand side of the FoV ($x \gtrsim 20$ mm) had a positive $a_{x,f}$, particles detected on the left-hand side ($x \lesssim 20$ mm) had a negative $a_{x,f}$. The combination of

both effects explains the observed difference in $a_{x,1}$ for $y = (0 - 15)$ mm, depending on the electric field strength in Figure 5.5.

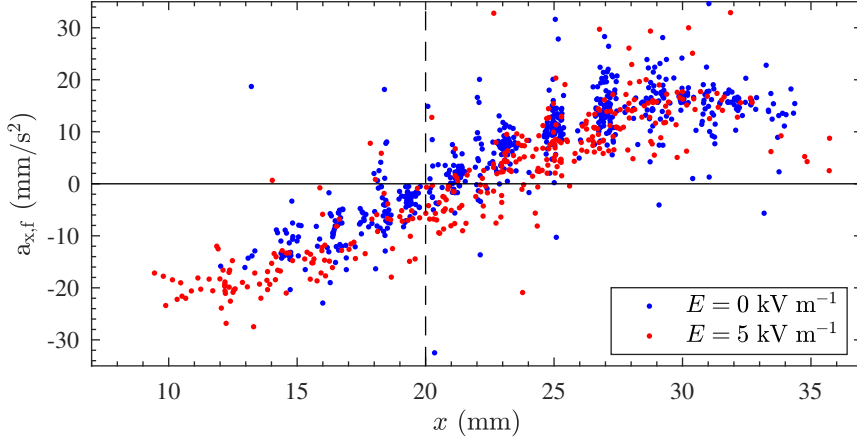


Figure 5.7: Scatter plot of the trajectory-averaged horizontal acceleration $a_{x,f}$ as a function of the horizontal position x , with the camera focused on the central region between the electrodes (as indicated in Figure 5.2). Figure 5.7 shows the combined data of four measurements (two for each electric field strength). The given electric field strength corresponds to the value in the centre of the electrodes.

In Figure 5.8, $a_{x,f}$ is plotted versus the horizontal position x , for the camera focused at the top part of the electrodes. The horizontal acceleration is plotted for $E = 0 \text{ kV m}^{-1}$ and $E = 5 \text{ kV m}^{-1}$. Both trends showed no dependence of the horizontal position until they diverged into two branches at $x \approx 25$ mm, i.e. both negative and positive values of $a_{x,f}$ have been measured for the same x position. This is due to a combination of a flow and imaging effect. First, the particle trajectories were S-shaped since they were compressed due to the electrodes. Second, some particles travelled out of the laser sheet before the end of the FoV and, thereby, their trajectory was only partially imaged. The combination of these effects caused relatively short particle trajectories to have a negative a_x , while the particle trajectories that were imaged in full FoV had a positive $a_{x,f}$.

Upon comparison of the $E = 0 \text{ kV m}^{-1}$ and $E = 5 \text{ kV m}^{-1}$ data, it is clear that, on average, the particles were not shifted by the electric force, as was the case with the camera focused on the central region between the electrodes (see Figure 5.7). This observation is in accordance with expectations, since at the top part of the electrodes, the particles had only just entered the region of applied electric field strength. In contrast, in the central region of the electrodes, they had experienced the integrated effect of the electric field of the whole region above.

Figure 5.7 and Figure 5.8 show the influence of the mesh grid on the spatial particle distribution. The fact that the grid structure was visible in the spatial particle distribution shows that particle scattering on the mesh grid had a negligible influence. This effect has been discussed in our previous work [163] (see chapter 4).

In conclusion, the compression of the flow and the displacement of the particles explain the difference between the trends in $a_{x,1}$ for the different electric field strengths in the region $y = (0 - 15)$ mm. On the other hand, the same flow effect did not influence the measured $a_{x,1}$ for $y = (35 - 45)$ mm, since the particles were not yet displaced at this position.

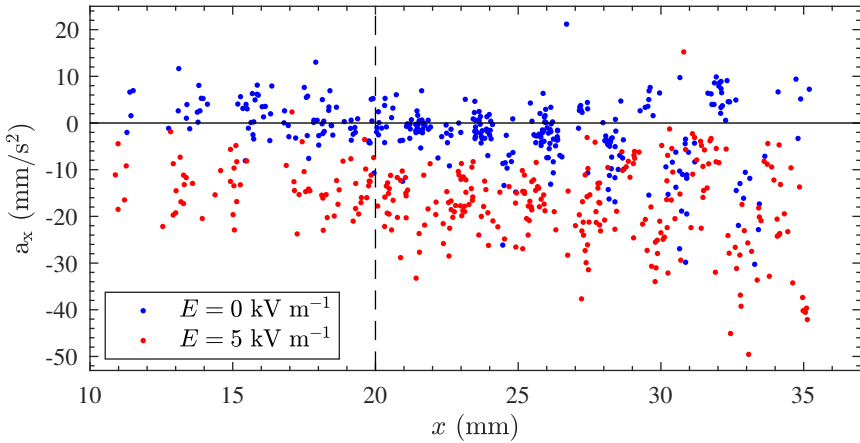


Figure 5.8: Scatter plot of the trajectory-averaged horizontal acceleration $a_{x,f}$ as a function of the horizontal position x , where the camera was focused at the top part of the electrodes (as indicated in Figure 5.2). The figure shows the combined data of four measurements (two for each electric field strength). The electric field strength given corresponds to the value in the centre of the electrodes.

5.7.2 Constant spread in acceleration

The second noteworthy observation from Figure 5.5 is the constant spread in the measured local acceleration independent of the electric field strength. According to expectations, the spread in acceleration caused by the electric force, would be proportional to the electric field strength. The measured constant spread in $a_{x,1}$ was caused by the flow acceleration distribution, as already shortly mentioned in section 5.4.

In Figure 5.9, the $a_{x,f}$ distribution is plotted for $E = 0 \text{ kV m}^{-1}$, $E = 2.5 \text{ kV m}^{-1}$ and $E = 5 \text{ kV m}^{-1}$, where each distribution is divided between the left part of the FoV, $x < 20$ mm indicated in green, and the right part of the FoV, $x > 20$ mm indicated in blue. It clearly shows that the $a_{x,f}$ distribution was a bimodal distribution and that the spread was independent of the electric field strength. Also, the already mentioned shift in the position of the particles and the corresponding change in $a_{x,f}$ is visible (also see appendix subsection 5.7.1). In conclusion, the constant spread in $a_{x,f}$ proved independent of E and was predominantly caused by the flow distribution.

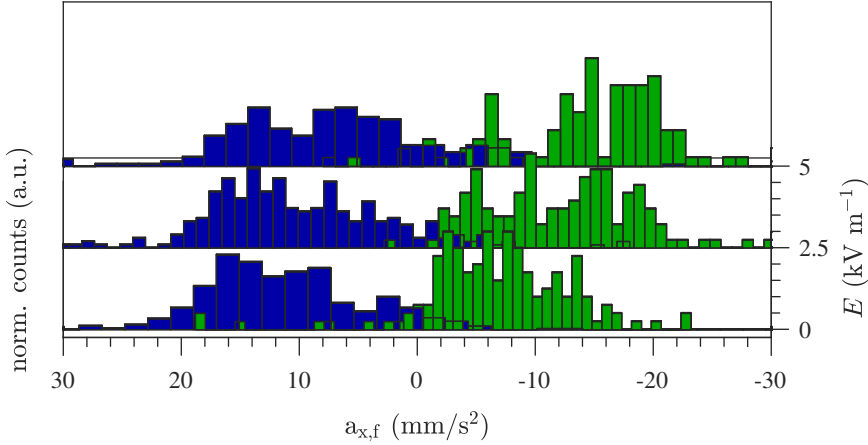


Figure 5.9: Histograms of the trajectory-averaged horizontal acceleration $a_{x,f}$ as a function of the horizontal position x , measured in the central region between the electrodes for three different electric field strengths. Indicated in blue are the particles measured on the right-hand side of the FoV ($x > 20$ mm). Indicated in green are the particles measured on the left-hand side of the FoV ($x < 20$ mm). The given electric field strength corresponds to the value in the centre of the electrodes.

5.7.3 Measured acceleration at the end of FoV 2

The third observation from Figure 5.5 is the omitted points for $y = (20 - 30)$ mm. While the plotted points consisted on average of 200 particles, the omitted points were not plotted due to a scarcity of particle detections there. The latter was caused by particles moving out of the laser sheet, which was most probably due to particles having a small velocity component towards or away from the camera. The particles thereby left the imaging region before the end of the FoV as the laser sheet had a thickness of only 3 mm.

This section will first analyse and discuss the trajectory-averaged acceleration $a_{x,f}$ as a function of t . The observed trend in $a_{x,f}$ highlights the importance of sufficient particle detections for each local position of y . Second, the average time t and the horizontal position x as a function of y are treated, giving a full overview on why the $a_{x,l}$ was not plotted for $y = (20 - 30)$ mm.

In Figure 5.10 the trajectory-averaged horizontal acceleration $a_{x,f}$ is plotted against the starting time of the trajectories, where $t = 0$ s corresponded to the moment the plasma discharge was switched off. Whereas the trend for $E = 0$ kV m⁻¹ showed almost no dependence on t , the trend for $E = 5$ kV m⁻¹ decreased as function of t , i.e. particles had a higher negative acceleration if they were detected later. This means that the particle charge was not constant in time, which can most probably be explained by the ion flux received by the particles in the shielded SPA (the region below the mesh grid).

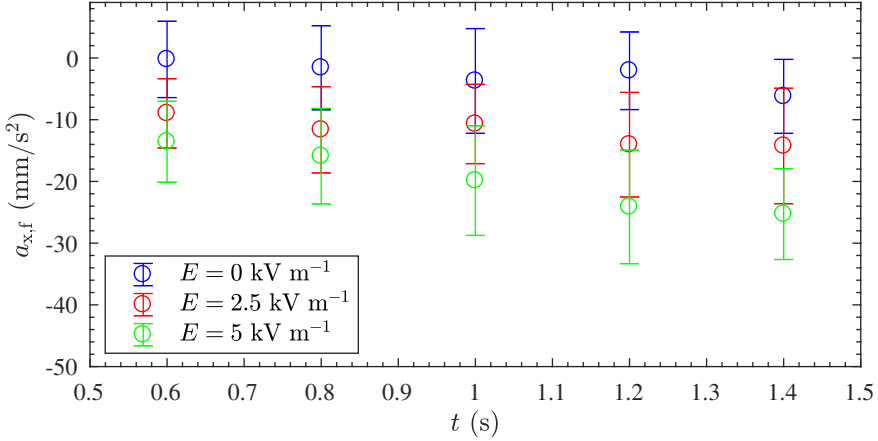


Figure 5.10: Plot of the trajectory-averaged horizontal acceleration $a_{x,f}$ as a function of time after the plasma was switched off for three different electric field strengths. The given electric field strength corresponds to the value in the centre of the electrodes with the camera focused on the central region of the electrodes (FOV1).

Particles detected at $t = 0.5$ s were approximately 65 mm above the FoV when the plasma was switched off. Hence, these particles travelled through the almost full shielded SPA before the plasma discharge was switched off. Yet, particles detected at $t = 1.5$ s were approximately 65 mm below the grid when the plasma discharge was switched off. Hence, these particles travelled through an almost entirely decayed shielded SPA (as sketched in Figure 5.4). This distinction in experienced afterglow by the particles explains the difference in the ion flux the particles experienced and, hence, the difference in observed $a_{x,f}$.

Figure 5.5 combines the particles detected at different times for each value of y . Thereby, the trend in $a_{x,f}$ was averaged out as long as enough particles were detected at each position and at each moment in time. To verify this, the vertical position y was plotted as a function of the average detection time t_d in Figure 5.11, where $t_d = 0$ s corresponds to the moment the particles were injected. As expected, t_d decreased approximately linearly with increasing height due to the constant settling velocity of the particles. The small offset in the decreasing lines of FoV1 and FoV2 were most probably caused by camera positions misalignments of several millimetres. As explained at the outset of this section, fewer particles were detected at the end of FoV2 (18.6 mm and 23.6 mm). Also the average horizontal position s of the particle beam as a function of y deviated from the trend at these y values, as depicted in Figure 5.12. Therefore, both t_d and s deviated from the linear trend. Consequently, these data points are omitted in Figure 5.5 and Figure 5.6.

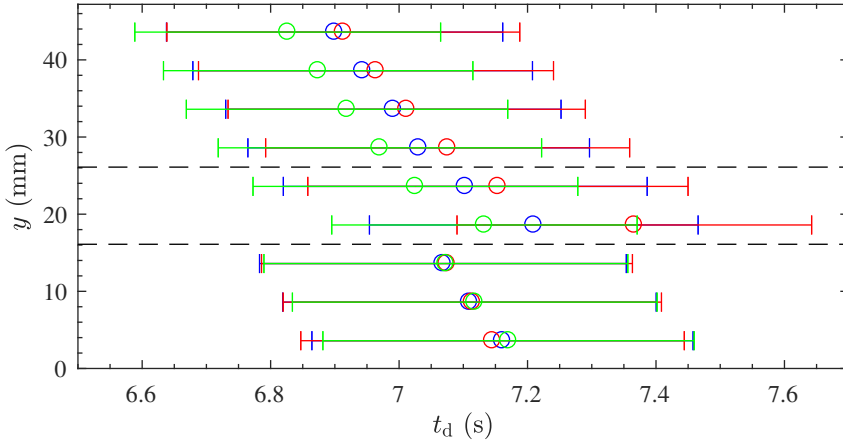


Figure 5.11: Plot of the vertical position y as a function of the detection time t_d for three different electric field strengths: blue $E = 1.25 \text{ kV m}^{-1}$, red $E = 2.5 \text{ kV m}^{-1}$ and green $E = 5.0 \text{ kV m}^{-1}$. The given electric field strength corresponds to the value in the centre of the electrodes. The horizontal dashed lines indicate the region at the end of FoV2 where insufficient particles were detected.

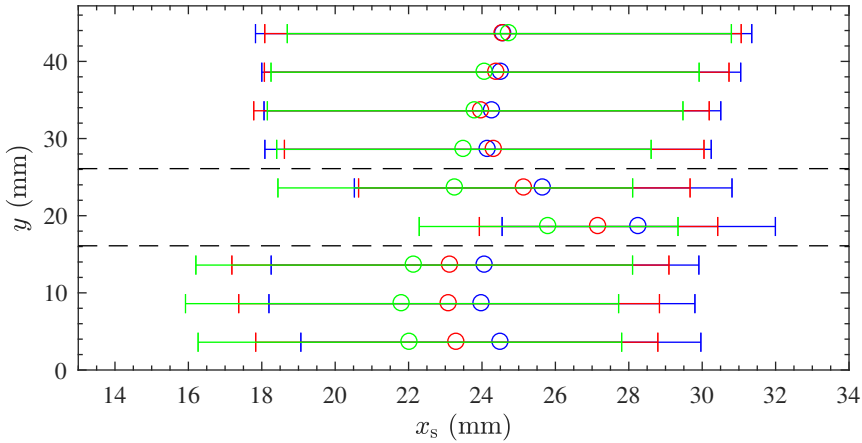


Figure 5.12: Plot of the vertical position y as a function of the segment-averaged horizontal position x_s for three different electric field strengths: blue $E = 1.25 \text{ kV m}^{-1}$, red $E = 2.5 \text{ kV m}^{-1}$ and green $E = 5.0 \text{ kV m}^{-1}$. The given electric field strength corresponds to the value in the centre of the electrodes. The horizontal dashed lines indicate the region at the end of FoV2 where insufficient particles were detected.

Revealing the charge of clustered microparticles: proof for the smallest enclosing sphere model in the spatial plasma afterglow

Abstract

Plasma-induced charging of non-spherical microparticles is a crucial parameter in complex plasma physics, aerosol science and astrophysics. Yet, the literature describes this charge by two competing theories, neither of which has been experimentally verified or refuted. This chapter offers experimental proof that the charge on a two-particle cluster (doublet) in the spatial afterglow of a low-pressure plasma equals the charge obtained by the smallest enclosing sphere and that it should therefore not be based on its total capacitance. To support this conclusion, the size, mass and charge of single particles (singlets) and doublets were measured with high precision. The measured ratio between the plasma-afterglow-induced charges on doublets and singlets was compared to both theories and showed perfect agreement with the predicted ratio using the smallest enclosing sphere model, while being significantly dissimilar to the predicted value based on the particle capacitance.

This chapter is in revision:

B. van Minderhout, J.C.A. van Huijstee, R.M.H. Rompelberg, A. Post, A.T.A. Peijnenburg, P. Blom and J. Beckers, “Charge of clustered microparticles measured in spatial plasma afterglows follows the smallest enclosing sphere model” Journal: *Nature Communications*

6.1 Introduction

The charge and charging of non-spherical or clustered nano- to micrometre-sized particles in partly ionized media is a key parameter in research fields such as complex plasma physics, astrophysics and aerosol science. In this chapter, the term clustered particles refers to aggregates of individual particles. In complex plasma physics, studying the fundamental interaction between particles and plasma, the non-spherical particle charge drives the coagulation and aggregation of particles that are synthesised within the plasma discharge [21, 174]. Therefore, cylindrically-shaped particles [175–181], spheroid-shaped particles [182, 183] and aggregates [184] have attracted special interest. In astrophysics, the charging of clustered particles [141] is studied especially [28–33], since the latter are commonly found in protoplanetary disks where planet formation takes place [31–34]. The clustered particle charge seems heavily dependent on its morphology, which in turn impacts the particles' accretion process [31]. In aerosol science, extensive experimental and computational research is reported on the charging of non-spherical particles at atmospheric pressures [35–40], since particle charge is of vital importance in determining particle size in differential mobility analyzers.

From an application point of view, understanding the collection of charges by non-spherical particles from their environment has major implications. Plasma-assisted contamination control strategies [13] may have high potential to tackle the challenge of particle contamination, both with regard to ultra-clean systems in the semiconductor industry [50] as well as to lowering worldwide air pollution produced by combustion engines [185, 186]. The principle of these plasma-assisted control techniques stems from the ability of plasma to charge the non-spherical particles and to affect their trajectories by either plasma-induced [51] or externally applied electric fields. Since the latter would be shielded in the plasma bulk, particle charging in the plasma afterglow (with pure diffusion charging in the limiting case) is of the utmost importance for the two respective applications.

In medical applications, the charge and morphology of nanoparticles (NPs) used in medications play a vital role in drug delivery [187–189]. Positively charged NPs improve the efficacy of imaging, gene transfer and drug delivery, while they also have higher cytotoxicity [44]. The latter shows that the charge control of these NPs is crucial and can be achieved in the spatial plasma afterglow, as has been recently demonstrated [163].

It thus seems clear that understanding the charging mechanism of non-spherical particles embedded in media where free charges are present is of the utmost importance in relevant fundamental and applied fields. Apart from this importance and its potential impact, one more thing stands out in these examples: the literature provides competing theories for calculating and predicting the charge on non-spherical and clustered particles.

On the one hand, the plasma-induced charge is described by equivalent enclosing models, of which two variants exist. Matthews et al. reported that, as long as the plasma currents to the particle surface dominate, the charge of clustered particles could be described by the charge that the sphere with the orientation-averaged equivalent radius R_σ would obtain [31, 190]. The morphology of the clustered particle determines

the value of R_σ , distinguishing between filigree and compact-shaped particles. Asnaz et al. showed that, in the particular case of the anisotropic plasma sheath, the smallest enclosing sphere correctly predicts the charge for tetrapods [191].

In complex plasma physics, however, the charge on non-spherical particles such as cylinders [175–181] and spheroids [182, 183] is commonly calculated or simulated based on the particle’s capacitance [192]. This approach has provided important insights in the charging of spherical particles in temporal plasma afterglows, where the Debye length can exceed the plasma bulk value [53, 56, 57]. In aerosol science, a uniform theory describing the non-spherical particle charge has equally been lacking [38–40] until Li and Gopalakrishnan recently proposed a unifying experimentally validated theory [162].

Thus far, it has remained unclear which theoretical framework should be used for low-density plasmas, such as the plasma afterglow under investigation here, since experimental data verifying or refuting either of the models have been non-existent. This chapter presents accurate charge measurements of clustered microparticles in a plasma afterglow, thereby proving that the charge on two-particle clusters (doublets) is correctly described by the charge on the smallest enclosing sphere.

The structure of this chapter is as follows: first, the particle charge distributions of single microparticles (singlets) and doublets are presented and discussed in section 6.2, and the measured ratios between the respective distributions are compared with the ratios predicted by the various models in section 6.3. Finally, an overview of the experimental setup is given, followed by the theoretical framework of the applied in situ cluster detection method in section 6.5, where the drag and torque appear to be essential.

6.2 Results

The results of this chapter are divided into two sections: the determined cluster sizes, which are determined in situ, and a presentation and comparison of the measured charge distributions of singlets and doublets.

6.2.1 Cluster sizes

The technique used to differentiate between single and clustered microparticles is based on the difference in neutral drag that the particles experience and on their obtained distinct settling velocities. This section presents measurements and analysis of the vertical settling velocity v_y , from which the particle mass and cluster size are ascertained.

The variation in individual particle mass was obtained from the measured settling velocity v_y using the neutral drag described in section 6.5 (Equation 6.3). Since gravity and drag are the dominant vertical forces, the radius of each singlet was obtained from

$$r_p = \frac{v_s \delta N m_n v_{th,n}}{\rho_p g}, \quad (6.1)$$

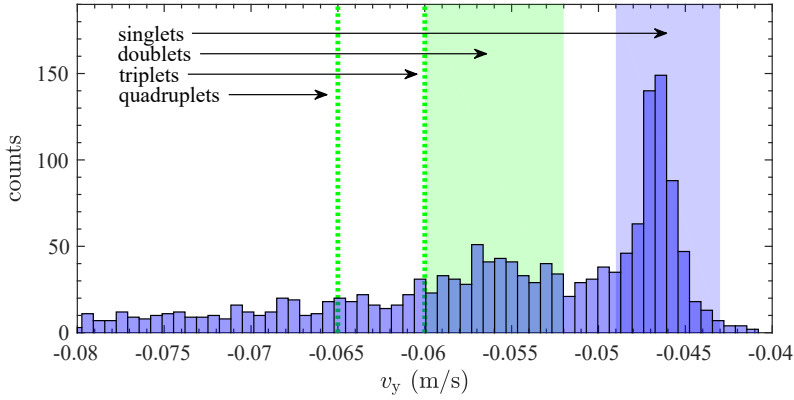


Figure 6.1: Histogram of the measured vertical velocity of all detected particles. The green band indicates the reported literature values of doublet velocities (see Table 6.1), which perfectly match the doublet peak observed in the velocity distribution. The green dotted lines show the predicted average vertical velocities of the triangular triplets and tetrahedral quadruplets. The blue band indicates the selected velocity range of the singlets.

where ρ_p is the average particle density and g the gravitational constant. The peak measured vertical velocity distribution for singlets stood at $4.6 \times 10^{-2} \text{ m s}^{-1}$, as will be shown at the end of this section. In section 6.5, the morphology of the used particles' outer layer is discussed using SEM analysis. Based on the observed surface roughness and the fact that the outermost silveroxide layer is non-conducting for argon atoms [193], $\delta = 1.442$ must hold, which states that the microscopic mechanism of the argon collisions at the particles' surface (see Equation 6.3) is described by diffuse collisions.

Using the supplier-provided radius ($2.5 \pm 0.1 \mu\text{m}$) and assuming the argon gas to equal 293 K, the first peak in Figure 6.1 was fitted using Equation 6.1 rewritten for v_s , resulting in $\rho_p = 1.61 \times 10^3 \text{ kg m}^{-3}$. The fitted particle density stood above the density of pure MF ($\rho_{\text{MF}} = 1.51 \times 10^3 \text{ kg m}^{-3}$) and was considered reasonable given the observed porosity as described in Figure 6.5 of section 6.5. Using Equation 6.1, the individual particle mass could easily be obtained using $m_p = 4/3\pi r_p^3 \rho_p$, assuming average particle density ρ_p to be constant.

In order to evaluate the cluster orientation with respect to the flow, the torque acting on a cylinder was estimated (Equation 6.6). From classical mechanics, it follows that the solution for $\beta = 0$ is stable, whereas the one for $\beta = \pi/2$ is unstable, i.e. the clusters align their long axis with the flow. Moreover, using the moment of inertia of a cylinder I_c , it could be estimated that this alignment takes place in approximately $t_c = I_c/\tau \approx 10 \text{ ms}$.

Knowing the cluster orientation, the ratio of cluster to singlet velocity could be obtained by equating the drag force calculated using Equation 6.3 and Equation 6.4 to the gravitational force on the particles. Hence,

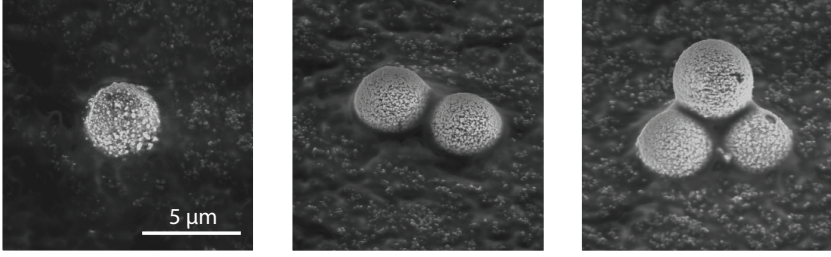


Figure 6.2: Three SEM images of the observed (clustered) microparticles.

$$\frac{v_c}{v_s} = \frac{N_p^{1/3}}{\chi_{\nu,\parallel}}, \quad (6.2)$$

where the subscript \parallel indicates orientation parallel to the flow. In the field of aerosol science, several studies [194–198] reported particle parameters χ_c and ϕ for parallel-oriented clustered microparticles, which are shown in Table 6.1 together with the corresponding v_y for each cluster size (calculated using Equation 6.5 and Equation 6.2).

Table 6.1: Particle parameters and the resulting v_y for doublets, triangular triplets and tetrahedral quadruplets oriented parallel to the flow [194–198].

	$\chi_{c,\parallel}$	ϕ_{\parallel}	$v_y (\cdot 10^{-2} \text{m s}^{-1})$
doublet	(1.02 – 1.025)	(1.21 – 1.384)	(5.2 – 6.0)
triplets	(1.08 – 1.094)	(1.41 – 1.491)	(5.9 – 6.2)
quadruplets	1.12	1.59	6.5

Figure 6.1 shows the measured vertical velocity v_y of all detected particles (singlets and clusters). The distribution shows two distinct peaks. The first, centred around $4.6 \times 10^{-2} \text{m s}^{-1}$, corresponds to the singlets, and the second, centred around $5.6 \times 10^{-2} \text{m s}^{-1}$ to the doublets. The measured doublet peak corresponds to the calculated range (see Table 6.1), which is indicated by the green band. The light blue band indicates the selected velocity range for the singlets. The expected peaks of the triplets and quadruplets are indicated by green dotted lines. Evidently, no distinct peaks are visible at these velocities. Thus, too few triplets and quadruplets were detected for statistical analysis, and these cluster sizes were therefore not considered in the analysis.

Figure 6.2 presents three SEM images of the injected (clustered) microparticles, which were collected after passing the plasma discharge. These images show the presence of singlets, doublets and triplets among the particles injected. A triangular configuration of the triplets was expected, since this configuration proved more stable than a string alignment [141]. To determine the doublet mass from its measured v_y , the average $\chi_{\nu,\parallel}$ from Table 6.1 was used. The following section takes into account the variation in reported literature values for the uncertainties in the measured particle charge distributions.

6.2.2 Charge distributions

Using the method based on the particle settling velocity, as explained in the previous section, the charge distribution of both singlets and doublets was measured independently. In addition to cluster size detection, variations in particle mass were taken into account that were also based on the vertical settling velocity. Figure 6.3 shows the charge distribution of singlets and doublets, together with a Gaussian fit and the corresponding mean charge. The higher positive charges in the singlet distribution were most likely 40 doublets which had a vertical velocity within the singlet boundaries (see Figure 6.1) and were omitted from the analysis.

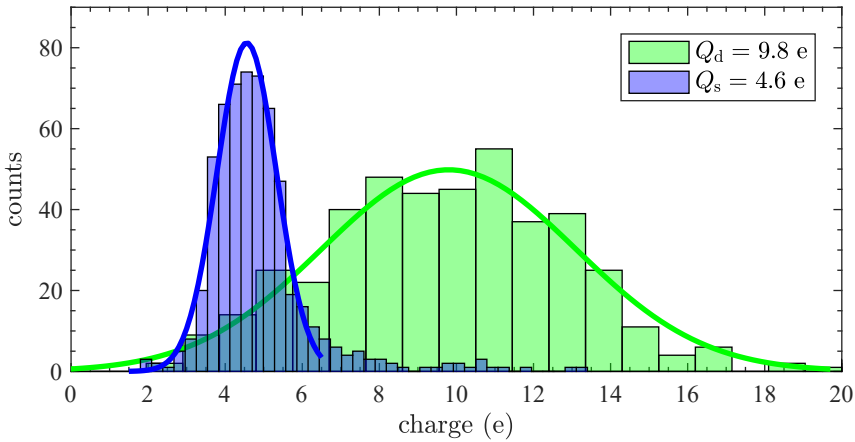


Figure 6.3: Histograms of the measured charge distribution of singlets (blue) and doublets (green) together with their mean positive charge. The singlet and doublet distributions consist of 581 and 434 particles respectively.

6.3 Discussion

The measured singlet and doublet charges were both positive, whereas the particle charge in the plasma bulk is known to be highly negative [123, 148]. With regard to the late spatial afterglow, Couédel et al. have shown that the particle charge can indeed become positive and is determined by the transition from ambipolar to free diffusion [56]. It is likely that in our experiments, the externally applied electric field influenced the latter transition. Positively charged particles in afterglows were also reported in several other studies [53, 59, 168, 199–201]. Since the photon energy of the laser system was below the work function of silver [170], photodetachment was assumed to be negligible. Furthermore, due to the low gas (and particle) temperature combined with the low electric field strength, thermionic emission [202], field emission [203] and secondary electron emission [204] were expected to have had a negligible influence on particle charge.

The uncertainty in the mean singlet charge was obtained by calculating the standard deviation of the mean. Overall, the mean charge obtained for the singlets stood at $Q_s = 4.6 \pm 0.1$ e. The uncertainty in the doublet charge was predominantly determined by the spread in particle parameters reported in the literature (see Table 6.1) and therefore $Q_d = 9.8 \pm 0.9$ e. A possible error in particle mass, which could only have led to variations in the reported absolute charge values rather than in the reported charge ratio, was expected to be significantly smaller than the spread in particle parameters. Summarising, the ratio of the doublet to singlet charge was $R = 2.1 \pm 0.2$.

As stated in the introduction, the charge on clustered particles has been described by two different models in the literature. No experimental proof has yet been provided regarding which of the two models would be correct for spatial plasma afterglows. The capacitive model predicted the doublet to singlet charge ratio R to be 1.39 [205], determined solely by doublet capacitance. The equivalent enclosing sphere model reported by Matthews et al. [190] predicted a charge ratio R of 1.36, since the orientation-averaged equivalent radius was given by $R_\sigma = \sqrt{(PA/\pi)} \approx 1.36$, where PA was the average project area of doublet [162]. On the other hand, the smallest enclosing sphere model reported by Asnaz et al. predicted $R = 2$ [191]. It can therefore undoubtedly be concluded that the charge of doublets in the free spatial afterglow at intermediate pressure is described by the charge on the smallest enclosing sphere.

6.4 Conclusion

This study measured the charge of single microparticles (singlets) and two-particle clusters (doublets) in the free spatial afterglow. The measured ratio of doublet to singlet charge was 2.1 ± 0.2 . We conclude that the doublet charge was correctly described by the charge on the smallest enclosing sphere, whereas the prediction based on the doublet capacitance proved incorrect. Our results are of fundamental importance in complex plasmas [175–183, 190, 192], aerosol science [35–40] and astrophysics [28–33], as well as in numerous applications.

6.5 Methods

This section introduces the experimental setup, followed by the theoretical framework that is applied to detect in situ the size, mass and cluster configuration of the particles.

6.5.1 Experimental setup

The experiments were carried out in a vacuum system (the Plasma Particle Charging Investigation (PPCI) setup), which is shown schematically in Figure 6.4. A determining part of this system was a 1 m long square glass tube. The operating pressure was 90 Pa argon, with a background pressure of 10^{-9} Pa. At the top of the tube, particles were injected by a particle dispenser similar to the ones used in previous research [117, 118]. In the dispenser's container, the particles repeatedly collided with each other and with the container's walls triboelectrically charging the particles [141], thereby aiding the

natural conformation of clustered microparticles. Figure 6.5 shows a cross-section of a single microparticle used in the current research. Its core consisted of melamine-formaldehyde (MF) and the outer layer of a porous silver coating with a thickness of ~ 100 nm. The microparticles had a diameter of $d_p = 4.9 \pm 0.2 \mu\text{m}$ as stated by the manufacturer, microParticles GmbH.

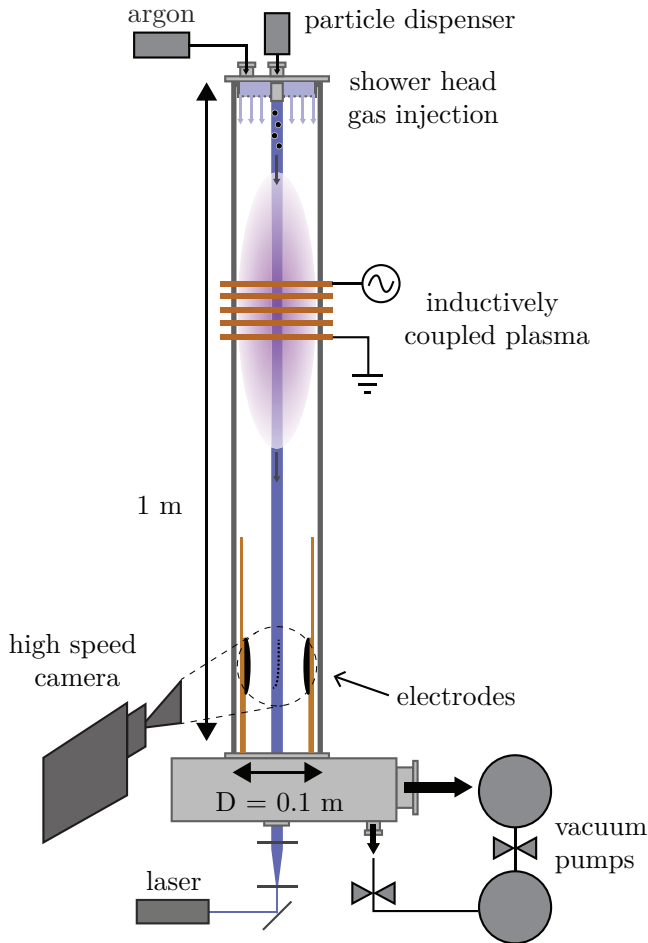


Figure 6.4: Schematic drawing of the PPCI setup. (Clustered) microparticles travelled through a spatially limited region of plasma. The particle charge was measured at the bottom of the tube by accelerating the particles in an externally applied electric field. Figure adapted from [163].

An inductively coupled plasma (ICP) was generated at a frequency of 13.56 MHz using a square coil wound around the tube with a plasma power of approximately 3 W. The discharge was operated in the E-mode. The latter statement was based on the low plasma power applied and the light emission observed [73]. Two parallel and vertically

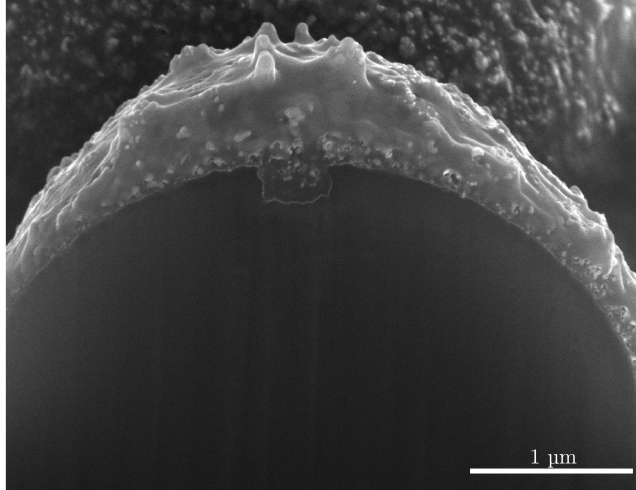


Figure 6.5: SEM image of the cross-section of a single silver coated melamine-formaldehyde microparticle. The cross-section is obtained by cutting the microparticle with a gallium focused ion beam (FIB).

aligned Rogowski electrodes were placed at the bottom of the setup [115, 206]. A voltage difference between these electrodes created an electric field that accelerated the charged particles in a horizontal direction, from which their charge was deduced. A typical plot of the particle trajectories can be found in our previous works [133, 163] (see chapter 3 and chapter 4). The breakdown field between the electrodes, with the plasma discharge switched on, was experimentally measured to be $E_{bd} = 8 \text{ kV m}^{-1}$. The field strength applied in this study (1 kV m^{-1}) was much smaller than E_{bd} . Possible reionisation, therefore, had a negligible effect on both particle charge and plasma shielding. Moreover, the afterglow density did not influence the electric field distribution, as shown in our previous work [133] (see chapter 3).

At the position of particle charge measurement, a lower limit for the plasma density was $n_i = 10^{11} \text{ m}^{-3}$ [163]. Furthermore, the electrons were expected to be close to room temperature based on a simple analytical timescale, as explained in our previous publication [133] (see chapter 3). For clarity, it should be mentioned that there are two types of plasma afterglows: temporal and spatial. The former is created by switching off the plasma discharge, while the latter is the region just outside of the active plasma region, in which the particle charging was studied in this research.

The particles were illuminated by a vertical 3 mm thick laser sheet (central wavelength 447 nm) and their scattered light was imaged by a high-speed camera (as depicted in Figure 6.4). The camera's field of view (FoV) was approximately 40 mm in a horizontal direction and 32 mm vertically. Typically, the particle density was 10^6 m^{-3} ,

such that mutual particle interactions did not occur [163]. To obtain the respective particle charge and cluster size, the position, velocity and acceleration of the particles were ascertained using in-house developed particle tracking software.

In contrast to our previous work [163] (see chapter 4), there were four differences in the setup and the analysis. First, to enable cluster detection, no flow was injected at the top of the tube, as explained in the next section. To achieve vacuum purity, the plasma discharge was switched off after each measurement and pumped down to base pressure. An experiment took on average two minutes to complete.

Second, to detect both single and clustered microparticles, the time delay between the moment of particle injection and the start of camera recording varied between (10 – 21) s.

Third, the analysis required the particle trajectories to be visible in the entire FoV, instead of a minimum trajectory length. This enabled the small changes in particle charge in the FoV region to be averaged in the same way for each particle, resulting in a trajectory-averaged charge.

Fourth, to obtain the particle charge from their acceleration in the region of the applied electric field, the trajectory-averaged electric field was calculated for each particle. To this end, a 2D electrostatic simulation was used to evaluate the electric field between the electrodes at each point of the trajectories (see Figure 2 in [163]). This simulation was performed in a geometry void of any physical obstruction above the electrodes. Using the simulation, small variations in the electric field were taken into account when obtaining the particle charge.

6.5.2 Cluster detection

The technique applied in this chapter to determine in situ the size, mass and cluster configuration of the particles was based on several relations which are discussed and experimentally verified below.

The drag force on a single microparticle was described by the Epstein formula when the mean free path of the atom-atom collisions λ_n is much larger than the radius of the particle r_p (i.e. the free molecular flow regime), and when the particle speed v_s is small compared with the thermal velocity of the gas particles $v_{th,n}$ [98]

$$F_{d,s} = \frac{4\pi}{3} \delta r_p^2 \rho_n v_{th,n} v_s, \quad (6.3)$$

where ρ_n represents the argon gas density. The coefficient δ accounts for the microscopic mechanism of the collisions between the particles and the gas atoms. For perfect specular reflections $\delta = 1$, whereas for diffuse reflections $\delta = 1.442$ for a thermal non-conducting particle [98].

The drag force on a cluster consisting of N_p particles in the free molecular regime can be quantified using the dynamic shape factor χ_ν as

$$F_{d,c} = \chi_\nu F_{d,s}(d_{ve}) \quad (6.4)$$

where d_{ve} is the volume equivalent diameter defined as $d_{ve} = 2N_p^{1/3}r_p$. In the literature, numerous experiments reported on the dynamical shape factor in the

continuum regime χ_c [194–198]. In order to calculate χ_ν from χ_c , the adjusted diameter was used, defined as $d_a = (\chi_\nu/\chi_c) d_{ve}$ [207]. Using the definition $\phi = d_a/(2r_p)$, χ_ν can be expressed by

$$\chi_\nu = \frac{\phi\chi_c}{N_p^{1/3}} \quad (6.5)$$

The drag force acting on clusters depends on their orientation with respect to the flow. To analyse the clusters' orientation, the torque acting on a cylinder in the free molecular flow regime is given [208]

$$\tau = \frac{\pi}{4} a^2 l \rho_n v_c^2 \sigma_t \sin(2\beta). \quad (6.6)$$

Here, a and l are the radius and length of the cylinder, v_c the velocity relative to the flow, β the angle between the long axis of the cylinder and the flow direction, and σ_t the tangential momentum accommodation factor.

The relations above are valid in the free molecular flow regime, which is the case for the current experiments. Figure 6.6 presents the measured vertical velocity of singlets as a function of the gas pressure in the absence of plasma. The other experimental conditions are identical to the ones described at the beginning of the methods section. The error bars in v_y are determined by calculating the standard deviation of the mean, and in p by experimental limitations. Furthermore, Figure 6.6 shows that the relation that could be obtained for v_s using Equation 6.1 perfectly matched the experiments using $\delta = 1.442$ and $\rho_p = 1.61 \times 10^3 \text{ kg m}^{-3}$. Therefore, it can be concluded that the drag force was indeed described by the free molecular flow relation given in Equation 6.3.

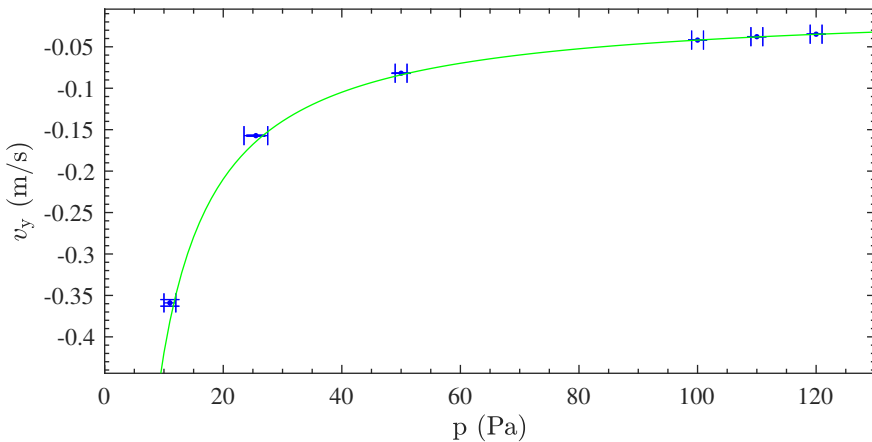


Figure 6.6: Measured vertical velocity of single microparticles as a function of the pressure together with the expected vertical velocity based on Equation 6.1 in the free molecular flow regime for $\delta = 1.442$ and $\rho_p = 1.61 \times 10^3 \text{ kg m}^{-3}$ (green line).

Overall conclusions

Abstract

In this research, an experimental setup was designed, developed and realised, which enabled the control and precise measurement of the microparticle charge. The charge of particles was controlled ranging from small negative charges ($-40e$) to even small positive charges ($10e$), including neutral particles with single electron precision. The achieved control gave insight into the complex interplay of plasma processes that determine the particle (de)charging and the final particle charge. In this chapter, the overall conclusions related to this research are presented.

In this chapter, the overall conclusions drawn from the research described in chapters 3-6 are presented and reflected on. As stated in the introduction:

This research aims to obtain a fundamental understanding of the charge and (de)charging of microparticles in low-pressure spatial plasma afterglows.

To accomplish this research goal, an experimental setup was designed, developed and realised. This setup enabled the control and precise measurement of the microparticle charge, ranging from small negative charges ($-40e$) to even small positive charges ($10e$), including neutral particles with single electron precision. The achieved control gave insight into the complex interplay of plasma processes that determine the particle (de)charging and the final particle charge. As demonstrated in this thesis, not only is the particle charge determined by the plasma species arriving at the particle's surface in the plasma bulk, but the plasma afterglow, in particular, dictates the final particle charge. Therefore, the whole system through which the particles travelled is of importance, including the plasma bulk and the afterglow which, in turn, is influenced by the externally applied electric field created to measure the particle charge.

As described in the introduction (chapter 1), two research lines were defined in the framework of this thesis (see Figure 7.1). In the sections below, the author conveys the conclusions for both research lines.

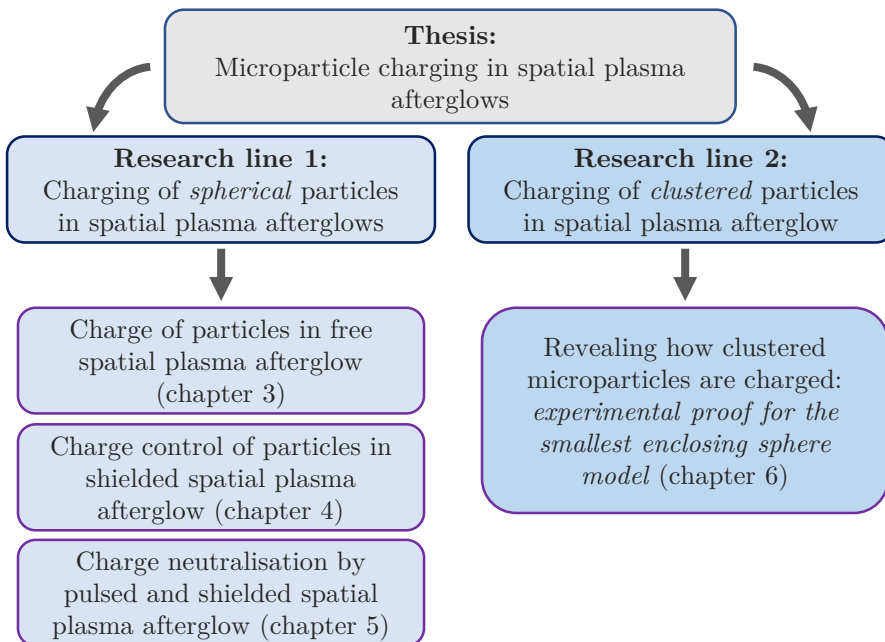


Figure 7.1: Overview of the research framework of this thesis. The research is divided in two research lines of which the results have been discussed in chapters 3-6.

Conclusions research line 1: charging of spherical particles in spatial plasma afterglows

In the (free) spatial plasma afterglow, the particle charge is three orders of magnitude lower than the particle charge expected in the plasma bulk. In the experiments presented in chapter 3, the particle charge was precisely measured in the free spatial plasma afterglow, i.e. without physical obstruction between the active plasma region and its spatial plasma afterglow. The measured charge on silver-coated melamine-formaldehyde particles with a diameter of $4.9 \pm 0.2 \mu\text{m}$ was $-30 \pm 7 e$.

In the plasma bulk, the specified microparticles typically obtained a negative charge of around $-10^4 e$. To analyse the difference in particle charge between the bulk and the plasma afterglow, the measured charge was compared to a relatively simple timescale model. This model suggested that the distinction in the electron temperature between the bulk and the afterglow region mainly determines the vast difference in particle charge.

These results have been published as “The charge of micro-particles in a low pressure spatial plasma afterglow” by B. van Minderhout, A.T.A. Peijnenburg, P. Blom, J.M. Vogels, G.M.W. Kroesen and J. Beckers (2019), *Journal of Physics D: Applied Physics* **52** 32LT03.

In the shielded spatial plasma afterglow, the particle charge could be precisely controlled from small negative ($-40 e$) to even small positive charges ($+10 e$) by changing the strength of an externally applied electric field. In the experiments presented in chapter 4, the plasma afterglow was shielded from the active plasma region by the application of a mesh grid. The particle charge control was achieved by variation of the externally applied electric field below this mesh grid, which in turn altered the local ion space charge distribution in this region. In the shielded spatial plasma afterglow, the vertical electric field component inherently arising from the geometry of the setup was dominant and, therefore, influenced the ion space charge. In contrast, this vertical electric field component was much less dominant in the free spatial plasma afterglow.

For this setup geometry, the electric field-induced variations in ion densities have been substantiated by measurements of the separate currents received by the electrodes, which were used to create the externally applied electric field.

These results have been published as “Charge control of micro-particles in a shielded plasma afterglow” by B. van Minderhout, J.C.A. van Huijstee, B. Platier, A.T.A. Peijnenburg, P. Blom, G.M.W. Kroesen and J. Beckers (2020), *Plasma Sources Science and Technology* **29** 065005.

By pulsing the shielded spatial plasma afterglow, all microparticles were effectively neutralised. In the experiments presented in chapter 5, the discharge was switched off once all particles had passed the mesh grid (which shielded the plasma afterglow from the plasma bulk). Afterwards, spatially resolved measurements of the particle charge revealed its full neutralisation. The pulsing of the plasma discharge resulted in almost zero space charge at the moment of charge measurement. In contrast, in the continuous shielded plasma afterglow and free spatial plasma afterglow, as discussed above, the non-zero local space charge of plasma species determined the final charge.

The charge measurements in the pulsed shielded plasma afterglow show that all particles were entirely neutralised independently of the externally applied electric field strength. This observation is in accordance with expectations, since there were hardly any plasma species at the position of the charge measurement that could be influenced by the electric field. The measured initial particle charge before neutralisation follows the previously described charge control conclusions. The observed neutralisation of the particles could - in ascending order of certainty - be caused by photo-detachment, neutralisation by (trapped) ions and resonant charge exchange reaction.

These results are accepted for publication “Charge neutralisation of microparticles by pulsing a low-pressure shielded spatial plasma afterglow”, by B. van Minderhout, J.C.A. van Huijstee, A.T.A. Peijnenburg, P. Blom, G.M.W. Kroesen and J. Beckers (2021), *Plasma Sources Science and Technology* <https://doi.org/10.1088/1361-6595/abd81f>.

Conclusions research line 2: charging of clustered particles in spatial plasma afterglow

By direct measurements of the charge ratio of two-particle clusters (doublets) to single microparticles (singlets), first experimental proof is presented that the doublet charge is correctly described by the charge on the smallest enclosing sphere and not by its capacitance. Relevant literature described the plasma-induced particle charge by means of two contradicting models. Neither of the two models had been refuted or verified until now. In chapter 6, the charge of doublets ($9.8 \pm 0.9 e$) and singlets ($4.6 \pm 0.1 e$) was precisely measured in the free spatial plasma afterglow. Compared to the previously discussed free plasma afterglow results, in which a negative particle charge was measured in chapter 3, these experiments have been performed with a five times lower plasma power. This most probably constituted the dominant reason for the measured difference in particle charge and sign. The obtained charge ratio ($R_e = 2.1 \pm 0.2$) shows a perfect agreement with the charge ratio predicted using the smallest enclosing sphere model ($R = 2$), whereas the ratio based on the particle capacitance is far off ($R = 1.39$).

These results are in revision “Charge of clustered microparticles measured in spatial plasma afterglows follows the smallest enclosing sphere model”, by B. van Minderhout, J.C.A. van Huijstee, R.M.H. Rompelberg, A. Post, A.T.A. Peijnenburg, P. Blom and J. Beckers, journal: *Nature Communications*.

Conclusions for applications

Abstract

This thesis developed a fundamental understanding of the particle charging in spatial plasma afterglows. These findings are of vital importance for several applications. This chapter discusses the relevance of this research for plasma-assisted particle contamination control strategies by presenting guidelines for further developments. Moreover, the potential relevance for other applications, such as those in colourimetric sensing and medicine, is also briefly demonstrated.

Not only does this research increase the fundamental understanding of particle charging in spatial plasma afterglows (the conclusions of which are presented in chapter 7), but several applications could also benefit from the obtained knowledge. This research is primarily driven by the urge to further develop plasma-assisted contamination control strategies. In this chapter, conclusions for these plasma-assisted contamination control strategies will be presented, followed by a brief demonstration of the relevance of this research for several other applications.

Plasma-assisted contamination control

The principle of plasma-assisted techniques to remove airborne particles out of gas flows in high-tech systems is based on two (plasma) properties. First, particles injected into plasma and its afterglow become electrically charged. Second, the positions and trajectories of these charged particles can be controlled by electric fields that are, for example, induced at the boundaries of the plasma discharge or created externally. The obtained insights concerning both of these (plasma) properties are presented in this section.

Particle charging in spatial plasma afterglows

Plasma-assisted particle removal techniques rely heavily on the control of the plasma-induced charge of these particles. In the experiments described in this thesis, this charge control of microparticles was achieved, ranging from small negative to even small positive charges. For particle removal applications in low-pressure systems, charging particles negatively seems to be most effective since higher absolute values of the particle charge can be obtained when compared to positively charged particles.

The key in obtaining only these highly negatively charged particles in spatial plasma afterglows lies in having a fundamental understanding of the charging processes in this region. In chapter 3 and chapter 6, measurements of the particle charge in the same plasma afterglow configuration void of any physical obstruction were presented, showing that by only changing the plasma power, the sign of the particle charge could be reversed. Chapter 3 conveyed a negative particle charge of $-30 \pm 7 e$, whereas chapter 6 reported on a particle charge of $+4.5 \pm 0.1 e$. The measurements that resulted in a positive particle charge were obtained with an approximately five times smaller plasma power. In a low-density plasma, as the case for a plasma generated at low power, the diffusion of plasma species will transition from ambipolar to free diffusion (ions and electrons are no longer Coulomb-coupled) at a shorter distance from the plasma bulk as compared to high-density plasmas. It is believed that the transition from ambipolar to free diffusion is the governing mechanism for the measured positive particle charge in chapter 6.

The author therefore concludes that the particle charging dynamics in the late spatial plasma afterglow is, besides the electron temperature, also determined by the local plasma density. When a high negative particle charge is desired, the particles must be removed in the region upstream of the location at which the transition from ambipolar to free diffusion takes place. Therefore, if an externally applied electric field

is chosen to control the position and the trajectories of the particles, it is advised to generate this field relatively close to the plasma bulk.

Charging of irregularly shaped particles

In virtually all applications, the contaminating particles to be removed from the systems were irregularly shaped or clustered, which stood in sharp contrast to the mono-disperse particles used in most studies. Therefore, it was crucial to understand the charging of non-spherical particles, which differs significantly from the charging of spherical particles. In chapter 6, first experimental proof has been presented showing that the charge of two-particle clusters (doublets) is described by the charge the smallest enclosing sphere obtains and not by its capacitance. The reported measurements answer an outstanding question in the literature and suggest that the charge of other non-spherical particles could also be described by the smallest enclosing sphere model. In particular for applications where non-spherical particles are expected, these results can help define design requirements.

Electric fields in spatial plasma afterglows

The second important requirement for plasma-assisted particle removal applications is the ability of electric fields to influence the position and trajectories of charged particles. In the experiments described in this thesis, the charged particles were affected by an externally applied electric field. Chapter 4 has shown that this externally applied electric field can change the properties of the spatial plasma afterglow if vertical components are generated, i.e. electric fields generated in the direction from the plasma bulk to the afterglow. In the relevant experiments, a mesh grid was placed in the cross-section of the tube separating the plasma bulk from its afterglow. Precise measurements of the plasma current in the afterglow revealed that the ion concentration and symmetry were altered by variation of the externally applied electric field strength. The author therefore concludes that a mesh grid can be used to limit the plasma volume. Yet, it also alters the plasma charge carrier densities, which in turn alters the particle charge. It is therefore advised to carefully consider the use of mesh grids and to avoid the creation of high electric fields in the direction from the plasma bulk to its afterglow if negatively charged particles are desired.

Other applications

Apart from the described relevance for plasma-assisted particle removal applications, the findings presented in this thesis can also be of importance for other applications. Chapter 5 has reported on the full neutralisation of microparticles in the pulsed and shielded spatial plasma afterglow. This shielded spatial plasma afterglow was created by the application of a mesh grid. Neutral particles are highly useful for colourimetric sensing applications. Compared to conventional techniques based on charge screening of the particles by the addition of salt, neutral particles improve the detection time, signal stability and sensitivity of the colourimetric sensing method.

Moreover, nanoparticles are intensively tested for the use in medical products, especially for drug delivery and imaging. The charge of these nanoparticles is crucial for the properties of medical products. For example, positively charged particles are reported to have higher cytotoxicity, whereas they improve the imaging, gene transfer and drug delivery. Therefore, carefully controlling the charge of these particles is crucial. Chapter 4 has shown that the charge of microparticles can be precisely controlled, ranging from small negative to even small positive charges in the spatial plasma afterglow. Also, particles can be fully neutralised in the spatial plasma afterglow, which is described in chapter 5.

A fundamental understanding of particle charging in spatial plasma afterglows has been developed in this thesis, which allows controlling the charge of microparticles carefully. These findings are not only beneficial for the further development of plasma-assisted contamination control strategies, but also for a variety of other applications.

Bibliography

- [1] Benschop J, Banine V, Lok S and Loopstra E “Extreme ultraviolet lithography: Status and prospects” 2008 *J. Vac. Sci. Technol. B Microelectron. Nanom. Struct.* **26**, 2204–2207
- [2] Moshhammer H and Neuberger M “Lung cancer and dust exposure: Results of a prospective cohort study following 3260 workers for 50 years” 2004 *Occup. Environ. Med.* **61**, 157–162
- [3] Crookes W “On radiant matter; a lecture delivered to the British Association for the Advancement of Science, at Sheffield, Friday, August 22, 1879” 1879 *Am. J. Sci.* **s3-18**, 241–262
- [4] Langmuir I “Oscillations in Ionized Gases” 1928 *Proc. Natl. Acad. Sci. U. S. A.* **14**, 627–637
- [5] von Keudell A and Schulz-von der Gathen V “Foundations of low-temperature plasma physics—an introduction” 2017 *Plasma Sources Sci. Technol.* **26**, 113001
- [6] Martinu L and Poitras D “Plasma deposition of optical films and coatings: A review” 2000 *J. Vac. Sci. Technol. A Vacuum, Surfaces, Film.* **18**, 2619–2645
- [7] Johnson R W, Hultqvist A and Bent S F “A brief review of atomic layer deposition: From fundamentals to applications” 2014 *Mater. Today* **17**, 236–246
- [8] Donnelly V M and Kornblit A “Plasma etching: Yesterday, today, and tomorrow” 2013 *J. Vac. Sci. Technol. A Vacuum, Surfaces, Film.* **31**, 050825
- [9] Kong M G, Kroesen G, Morfill G, Nosenko T, Shimizu T, van Dijk J and Zimmermann J L “Plasma medicine: an introductory review” 2009 *New J. Phys.* **11**, 115012

- [10] Komori H, Soumagne G, Abe T, Suganuma T, Imai Y, Someya H, Takabayashi Y, Endo A and Toyoda K “Laser-produced plasma light source development for extreme ultraviolet lithography” 2004 *Japanese J. Appl. Physics, Part 1 Regul. Pap. Short Notes Rev. Pap.* **43**, 3707–3712
- [11] Fabry F, Rehmet C, Rohani V and Fulcheri L “Waste Gasification by Thermal Plasma: A Review” 2013 *Waste and Biomass Valorization* **4**, 421–439
- [12] Hoentsch M, Bussiahn R, Rebl H, Bergemann C, Eggert M, Frank M, von Woedtke T and Nebe B “Persistent Effectivity of Gas Plasma-Treated, Long Time-Stored Liquid on Epithelial Cell Adhesion Capacity and Membrane Morphology” 2014 *PLoS One* **9**, e104559
- [13] Beckers J, van Minderhout B, Blom P, Kroesen G and Peijnenburg T “Particle contamination control by application of plasma” 2020 *Proc. SPIE Extrem. Ultrav. Lithogr. XI* **11323**, 113232L
- [14] Vollath D “Plasma synthesis of nanopowders” 2008 *J. Nanoparticle Res.* **10**, 39–57
- [15] Girshick S L “Particle nucleation and growth in dusty plasmas: On the importance of charged-neutral interactions” 2020 *J. Vac. Sci. Technol. A* **38**, 011001
- [16] Khrapak S and Morfill G “Basic processes in complex (dusty) plasmas: Charging, interactions, and ion drag force” 2009 *Contrib. to Plasma Phys.* **49**, 148–168
- [17] Beckers J, Trienekens D J M and Kroesen G M W “Absolute measurement of the total ion-drag force on a single plasma-confined microparticle at the void edge under microgravity conditions” 2013 *Phys. Rev. E* **88**, 055101
- [18] Chaudhuri M, Khrapak S A, Kompaneets R and Morfill G E “Shielding of a small charged particle in weakly ionized plasmas” 2010 *IEEE Trans. Plasma Sci.* **38**, 818–825
- [19] Morfill G E, Annaratone B M, Bryant P, Ivlev A V, Thomas H M, Zuzic M and Fortov V E “A review of liquid and crystalline plasmas — new physical states of matter ?” 2002 *Plasma Phys. Control. Fusion* **44**, 263–277
- [20] Sharma S K, Kalita R, Nakamura Y and Bailung H “Dust charge measurement in a strongly coupled dusty plasma produced by an rf discharge” 2012 *Plasma Sources Sci. Technol.* **21**, 045002
- [21] Boufendi L and Bouchoule A “Particle nucleation and growth in a low-pressure argon-silane discharge” 1994 *Plasma Sources Sci. Technol.* **3**, 262–267
- [22] Mikikian M, Cavarroc M, Couédel L, Tessier Y and Boufendi L “Dust particles in low-pressure plasmas: Formation and induced phenomena” 2010 *Pure Appl. Chem.* **82**, 1273–1282

-
- [23] Levchenko I, Keidar M, Xu S, Kersten H and Ostrikov K K “Low-temperature plasmas in carbon nanostructure synthesis” 2013 *J. Vac. Sci. Technol. B, Nanotechnol. Microelectron. Mater. Process. Meas. Phenom.* **31**, 050801
- [24] Marvi Z, von Wahl E, Trottenberg T and Kersten H “Spatiotemporal sampling of growing nanoparticles in an acetylene plasma” 2020 *J. Appl. Phys.* **127**, 173301
- [25] Stoffels W W, Sorokin M and Remy J “Charge and charging of nanoparticles in a SiH₄ rf-plasma” 2008 *Faraday Discuss.* **137**, 115–126
- [26] Van De Wetering F M, Brooimans R J, Nijdam S, Beckers J and Kroesen G M “Fast and interrupted expansion in cyclic void growth in dusty plasma” 2015 *J. Phys. D: Appl. Phys.* **48**, 35204
- [27] Beckers J, Stoffels W W and Kroesen G M “Temperature dependence of nucleation and growth of nanoparticles in low pressure Ar/CH₄ RF discharges” 2009 *J. Phys. D: Appl. Phys.* **42**, 155206
- [28] Ma Q, Matthews L S, Land V and Hyde T W “Charging of aggregate grains in astrophysical environments” 2013 *Astrophys. J.* **763**, 77 (Preprint 1210.0459)
- [29] Richterova I, Nemecek Z, Pavlu J, Safrankova J and Vaverka J “Secondary Emission From Clusters Composed of Spherical Grains” 2016 *IEEE Trans. Plasma Sci.* **44**, 505–511
- [30] Okuzumi S “Electric charging of dust aggregates and its effect on dust coagulation in protoplanetary disks” 2009 *Astrophys. J.* **698**, 1122–1135 (Preprint 0901.2886)
- [31] Matthews L S, Land V and Hyde T W “Charging and coagulation of dust in protoplanetary plasma environments” 2012 *Astrophys. J.* **744**, 8
- [32] Marshall R S, Chai K B and Bellan P M “Identification of Accretion as Grain Growth Mechanism in Astrophysically Relevant Water–Ice Dusty Plasma Experiment” 2017 *Astrophys. J.* **837**, 56
- [33] Chai K B and Bellan P M “Formation and alignment of elongated, fractal-like water-ice grains in extremely cold, weakly ionized plasma” 2015 *Astrophys. J.* **802**, 112
- [34] Akimkin V V “A possible mechanism for overcoming the electrostatic barrier against dust growth in protoplanetary disks” 2015 *Astron. Reports* **59**, 747–761
- [35] Shahravan A, Lucas C and Matsoukas T “Nanowire charging in collisionless plasma” 2010 *J. Appl. Phys.* **108**, 083303
- [36] Shin W G, Wang J, Mertler M, Sachweh B, Fissan H and Pui D Y “The effect of particle morphology on unipolar diffusion charging of nanoparticle agglomerates in the transition regime” 2010 *J. Aerosol Sci.* **41**, 975–986

- [37] Park M, Park K, Moon H J, Ko S H and Shin W G “The effect of particle morphology on unipolar diffusion charging of silver nanowires” 2015 *Aerosol Sci. Technol.* **49**, 290–298
- [38] Chang J S “Theory of diffusion charging of arbitrarily shaped conductive aerosol particles by unipolar ions” 1981 *J. Aerosol Sci.* **12**, 19–26
- [39] Ku B K, Deye G J, Kulkarni P and Baron P A “Bipolar diffusion charging of high-aspect ratio aerosols” 2011 *J. Electrostat.* **69**, 641–647
- [40] Gopalakrishnan R, McMurry P H and Hogan C J “The bipolar diffusion charging of nanoparticles: A review and development of approaches for non-spherical particles” 2015 *Aerosol Sci. Technol.* **49**, 1181–1194
- [41] Wolfram J, Zhu M, Yang Y, Shen J, Gentile E, Paolino D, Fresta M, Nie G, Chen C, Shen H *et al.* “Safety of Nanoparticles in Medicine” 2015 *Curr. Drug Targets* **16**, 1671–1681 (Preprint [15334406](#))
- [42] Bhaskar S, Tian F, Stoeger T, Kreyling W, de la Fuente J M, Grazú V, Borm P, Estrada G, Ntziachristos V and Razansky D “Multifunctional Nanocarriers for diagnostics, drug delivery and targeted treatment across blood-brain barrier: perspectives on tracking and neuroimaging” 2010 *Part. Fibre Toxicol.* **7**, 3
- [43] Corbo C, Molinaro R, Parodi A, Toledano Furman N E, Salvatore F and Tasciotti E “The impact of nanoparticle protein corona on cytotoxicity, immunotoxicity and target drug delivery” 2016 *Nanomedicine* **11**, 81–100
- [44] Fröhlich E “The role of surface charge in cellular uptake and cytotoxicity of medical nanoparticles” 2012 *Int. J. Nanomedicine* **7**, 5577–5591
- [45] Jazayeri M H, Aghaie T, Avan A, Vatankhah A and Ghaffari M R S “Colorimetric detection based on gold nano particles (GNPs): An easy, fast, inexpensive, low-cost and short time method in detection of analytes (protein, DNA, and ion)” 2018 *Sens. Bio-Sensing Res.* **20**, 1–8
- [46] Lin C Y, Yu C J, Lin Y H and Tseng W L “Colorimetric Sensing of Silver(I) and Mercury(II) Ions Based on an Assembly of Tween 20-Stabilized Gold Nanoparticles” 2010 *Anal. Chem.* **82**, 6830–6837
- [47] Liu G, Lu M, Huang X, Li T and Xu D “Application of gold-nanoparticle colorimetric sensing to rapid food safety screening” 2018 *Sensors (Switzerland)* **18**, 1–16
- [48] Lerdsri J, Chananchana W, Upan J, Sridara T and Jakmune J “Label-free colorimetric aptasensor for rapid detection of aflatoxin B1 by utilizing cationic perylene probe and localized surface plasmon resonance of gold nanoparticles” 2020 *Sensors Actuators, B Chem.* **320**, 128356
- [49] Zhang X, Fan X, Wang Y, Lei F, Li L, Liu J and Wu P “Highly Stable Colorimetric Sensing by Assembly of Gold Nanoparticles with SYBR Green I: From Charge Screening to Charge Neutralization” 2020 *Anal. Chem.* **92**, 1455–1462

-
- [50] Martin Knotter D and Wali F *Particles in Semiconductor Processing* first edition 2010 (Elsevier Inc.) ISBN 9781437778304
- [51] Beckers J, Ockenga T, Wolter M, Stoffels W W, Van Dijk J, Kersten H and Kroesen G M “Microparticles in a collisional rf plasma sheath under hypergravity conditions as probes for the electric field strength and the particle charge” 2011 *Phys. Rev. Lett.* **106**, 115002
- [52] Ivlev A V, Kretschmer M, Zuzic M, Morfill G E, Rothermel H, Thomas H M, Fortov V E, Molotkov V I, Nefedov A P, Lipaev A M *et al.* “Decharging of Complex Plasmas: First Kinetic Observations” 2003 *Phys. Rev. Lett.* **90**, 55003
- [53] Couédel L, Mikikian M, Boufendi L and Samarian A “Residual dust charges in discharge afterglow” 2006 *Phys. Rev. E* **74**, 026403
- [54] Couédel L, Mezeghrane A, James B, Mikikian M, Samarian A, Cavarroc M, Tessier Y and Boufendi L “Plasma decays in dusty afterglow” 2007 *ECA* **31F**, P2.068
- [55] Couédel L, Samarian A A, Mikikian M and Boufendi L “Dust charge distribution in complex plasma afterglow” 2008 *Europhys. Lett.* **84**, 35002
- [56] Couédel L, Samarian A A, Mikikian M and Boufendi L “Influence of the ambipolar-to-free diffusion transition on dust particle charge in a complex plasma afterglow” 2008 *Phys. Plasmas* **15**, 063705
- [57] Couédel L, Mezeghrane A, Samarian A A, Mikikian M, Tessier Y, Cavarroc M and Boufendi L “Complex Plasma Afterglow” 2009 *Contrib. to Plasma Phys.* **49**, 235–259
- [58] Filatova I I, Trukhachev F M and Chubrik N I “Study of the process of dust grain discharging in the afterglow of an RF discharge” 2011 *Plasma Phys. Reports* **37**, 1042–1045
- [59] Layden B, Couédel L, Samarian A A and Boufendi L “Residual Dust Charges in a Complex Plasma afterglow” 2011 *IEEE Trans. plasma Sci.* **39**, 2764 – 2765
- [60] Stoffels W 1994 *Electrons, ions and dust in a radion-frequency discharge* Ph.D. thesis Eindhoven University of Technology
- [61] Swinkels G 1999 *Optical studies of micron-sized particles immersed in a plasma* Ph.D. thesis Eindhoven University of Technology
- [62] Paeva G V 2005 *Sheath phenomena in dusty plasmas* Ph.D. thesis Eindhoven University of Technology
- [63] Sorokin M 2005 *Dust particle formation in silane plasmas* Ph.D. thesis Eindhoven University of Technology
- [64] Beckers J 2011 *Dust particle(s) (as) diagnostics in plasmas* Ph.D. thesis Eindhoven University of technology

- [65] Van de Wetering F M J H 2016 *Formation and dynamics of nanoparticles in plasmas* Ph.D. thesis
- [66] Heijmans L C J 2016 *Quantifying Plasma Particle Lofting* Ph.D. thesis Eindhoven University of Technology
- [67] Schepers L P T 2018 *Illuminating the plasma - particle interaction* Ph.D. thesis Eindhoven University of Technology
- [68] Franklin R N “The plasma–sheath boundary region” 2003 *J. Phys. D. Appl. Phys.* **36**, R309–R320
- [69] Lieberman M A and Lichtenberg A J *Principles of Plasma Discharges and Materials Processing* 2005 (John Wiley & Sons, Inc.) ISBN 0471720011
- [70] Zaplotnik R, Vesel A and Mozetic M “Transition from E to H mode in inductively coupled oxygen plasma: Hysteresis and the behaviour of oxygen atom density” 2011 *Europhys. Lett.* **95**, 55001
- [71] Zhang X, Zhang Z K, Cao J X, Liu Y and Yu P C “The influence of gas pressure on E-H mode transition in argon inductively coupled plasmas” 2018 *AIP Adv.* **8**, 035121
- [72] Lieberman M A and Lichtenberg A J *Principles of Plasma Discharges and Materials Processing: Second Edition* 2nd ed 2005 (Wiley interscience) ISBN 0471720011
- [73] Kempkes P, Singh S V, Pargmann C and Soltwisch H “Temporal behaviour of the e to H mode transition in an inductively coupled argon discharge” 2006 *Plasma Sources Sci. Technol.* **15**, 378–383
- [74] Raizer Y P *Gas Discharge Physics* 1991 (Berlin: Springer) ISBN 9783642647604
- [75] Biondi M A “Diffusion cooling of electrons in ionized gases” 1954 *Phys. Rev.* **93**, 1136–1140
- [76] Celik Y, Tsankov T V, Aramaki M, Yoshimura S, Luggenhölscher D and Czarnecki U “Recombination and enhanced metastable repopulation in the argon afterglow” 2012 *Phys. Rev. E - Stat. Nonlinear, Soft Matter Phys.* **85**, 1–12
- [77] Nefedov A P, Morfill G E, Fortov V E, Thomas H M, Rothermel H, Hagl T, Ivlev A V, Zuzic M, Klumov B A, Lipaev A M *et al.* “PKE-Nefedov*: plasma crystal experiments on the International Space Station” 2003 *New J. Phys.* **5**, 33–33
- [78] Mott-Smith H M and Langmuir I “The Theory of Collectors in Gaseous Discharges” 1926 *Phys. Rev.* **28**, 727–763
- [79] Whipple E C “Potentials of surfaces in space” 1981 *Reports Prog. Phys.* **44**, 1197–1250

-
- [80] Khrapak S A, Morfill G E, Khrapak A G and D'Yachkov L G “Charging properties of a dust grain in collisional plasmas” 2006 *Phys. Plasmas* **13**, 052114
- [81] Gatti M and Kortshagen U “Analytical model of particle charging in plasmas over a wide range of collisionality” 2008 *Phys. Rev. E* **78**, 046402
- [82] Goree J “Charging of particles in a plasma” 1994 *Plasma Sources Sci. Technol.* **3**, 400–406
- [83] Ban L, Yoder B L and Signorell R “Photoemission from free particles and droplets” 2020 *Annu. Rev. Phys. Chem.* **71**, 315–334
- [84] Fabel G, Cox S and Lichtman D “Photodesorption from 304 stainless steel” 1973 *Surf. Sci.* **40**, 571–582
- [85] Green J C and Decleva P “Photoionization cross-sections: A guide to electronic structure” 2005 *Coord. Chem. Rev.* **249**, 209–228
- [86] Gomer R “Field emission, field ionization, and field desorption” 1994 *Surf. Sci.* **299-300**, 129–152
- [87] Le Picard R and Girshick S L “The effect of single-particle charge limits on charge distributions in dusty plasmas” 2016 *J. Phys. D: Appl. Phys.* **49**, 095201
- [88] Los J and Geerlings J “Charge exchange in atom-surface collisions” 1990 *Phys. Rep.* **190**, 133–190
- [89] Gauyacq J P and Borisov A G “Charge transfer in atom-surface collisions: Effect of the presence of adsorbates on the surface” 1998 *J. Phys. Condens. Matter* **10**, 6585–6619
- [90] Matsusaka S, Maruyama H, Matsuyama T and Ghadiri M “Triboelectric charging of powders: A review” 2010 *Chem. Eng. Sci.* **65**, 5781–5807
- [91] Pächtz T, Herrmann H J and Shinbrot T “Why do particle clouds generate electric charges?” 2010 *Nat. Phys.* **6**, 364–368
- [92] Lacks D J “The Unpredictability of Electrostatic Charging” 2012 *Angew. Chemie Int. Ed.* **51**, 6822–6823
- [93] Archimedes “ON FLOATING BODIES, BOOK I” *Work. Arch.* ed Heath T L (Cambridge: Cambridge University Press) pp 253–262
- [94] Daugherty J E, Porteous R K and Graves D B “Electrostatic forces on small particles in low-pressure discharges” 1993 *J. Appl. Phys.* **73**, 1617–1620
- [95] Stokes G G “On the effect of internal friction of fluids on the motion of pendulums” 1851 *Trans. Cambridge Philos. Soc.* **9**, 8–106
- [96] Knudsen M and Weber S “Luftwiderstand gegen die langsame Bewegung kleiner Kugeln” 1911 *Ann. Phys.* **341**, 981–994

- [97] Li Z and Wang H “Drag force, diffusion coefficient, and electric mobility of small particles. I. Theory applicable to the free-molecule regime.” 2003 *Phys. Rev. E. Stat. Nonlin. Soft Matter Phys.* **68**, 061206
- [98] Epstein P S “On the Resistance Experienced by Spheres in their Motion through Gases” 1924 *Phys. Rev.* **23**, 710–733
- [99] Khrapak S A, Ivlev A V, Morfill G E and Thomas H M “Ion drag force in complex plasmas” 2002 *Phys. Rev. E - Stat. Nonlinear, Soft Matter Phys.* **66**, 046414
- [100] Khrapak S A, Ivlev A V, Morfill G E and Zhdanov S K “Scattering in the Attractive Yukawa Potential in the Limit of Strong Interaction” 2003 *Phys. Rev. Lett.* **90**, 4
- [101] Khrapak S A, Ivlev A V, Morfill G E, Zhdanov S K and Thomas H M “Scattering in the attractive Yukawa potential: Application to the ion-drag force in complex plasmas” 2004 *IEEE Trans. Plasma Sci.* **32**, 555–560
- [102] Ivlev A V, Khrapak S A, Zhdanov S K, Morfill G E and Joyce G “Force on a Charged Test Particle in a Collisional Flowing Plasma” 2004 *Phys. Rev. Lett.* **92**, 205007
- [103] Khrapak S A, Chaudhuri M and Morfill G E “Ion Drag Force in Collisional Plasmas” 2009 *IEEE Trans. Plasma Sci.* **37**, 487–493
- [104] Nikolaev V S and Timofeev A V “Screening length in dusty plasma crystals” 2016 *J. Phys. Conf. Ser.* **774**, 012172
- [105] Barnes M S, Keller J H, Forster J C, O’Neill J A and Coultas D K “Transport of dust particles in glow-discharge plasmas” 1992 *Phys. Rev. Lett.* **68**, 313–316
- [106] Epstein P S “Zur Theorie des Radiometers” 1929 *Zeitschrift fur Phys.* **54**, 537–563
- [107] Talbot L, Cheng R K, Schefer R W and Willis D R “Thermophoresis of particles in a heated boundary layer” 1980 *J. Fluid Mech.* **101**, 737–758
- [108] Brock J R “On the theory of thermal forces acting on aerosol particles” 1962 *J. Colloid Sci.* **17**, 768–780
- [109] Li Z and Wang H “Thermophoretic force and velocity of nanoparticles in the free molecule regime” 2004 *Phys. Rev. E* **70**, 021205
- [110] Young J B “Thermophoresis of a Spherical Particle: Reassessment, Clarification, and New Analysis” 2011 *Aerosol Sci. Technol.* **45**, 927–948
- [111] Liu B, Goree J, Nosenko V and Boufendi L “Radiation pressure and gas drag forces on a melamine-formaldehyde microsphere in a dusty plasma” 2003 *Phys. Plasmas* **10**, 9–20

-
- [112] Shah R and London A *Laminar flow forced convection in ducts : a source book for compact heat exchanger analytical data* 1978 (London: Academic Press) ISBN 0120200511
- [113] White F M *Viscous Fluid Flow* 2nd ed 1991 (McGraw-Hill, Inc.) ISBN 0070697124
- [114] Aarne A and Thompson S *The types of the Folktale: A classification and bibliography: Annti Aarne's Verzeichnis der Märchentypen* 2nd ed 1964 (Helsinki: Academia Scientiarum Fennica) ISBN 9780833744890
- [115] Rogowski W “Die elektrische Festigkeit am Rande des Plattenkondensators” 1923 *Arch. für Elektrotechnik* **12**, 1–15
- [116] Matikainen A, Nuutinen T, Itkonen T, Heinilehto S, Puustinen J, Hiltunen J, Lappalainen J, Karioja P and Vahimaa P “Atmospheric oxidation and carbon contamination of silver and its effect on surface-enhanced Raman spectroscopy (SERS)” 2016 *Sci. Rep.* **6**, 37192
- [117] Schepers L P T, IJzerman W L and Beckers J “Oxygen content dependent etch rate of single polymer microparticles confined in the sheath region of a low pressure radiofrequency argon/oxygen plasma” 2018 *J. Phys. D. Appl. Phys.* **51**, 375203
- [118] Heijmans L C J and Nijdam S “Triboelectric and plasma charging of microparticles” 2016 *Europhys. Lett.* **114**, 64004
- [119] Wescott E M, Sentman D D, Heavner M J, Hallinan T J, Hampton D L and Osborne D L “The optical spectrum of aircraft St. Elmo’s fire” 1996 *Geophys. Res. Lett.* **23**, 3687–3690
- [120] *COMSOL Multiphysics® v 5.4. COMSOL AB, Stockholm Sweden* www.comsol.com
- [121] Kuhn H W “The Hungarian method for the assignment problem” 1955 *Nav. Res. Logist. Q.* **2**, 83–97
- [122] Bekkers E J, Chen D and Portegies J M “Nilpotent Approximations of Sub-Riemannian Distances for Fast Perceptual Grouping of Blood Vessels in 2D and 3D” 2018 *J. Math. Imaging Vis.* **60**, 882–899 (Preprint 1707.02811)
- [123] Tang X and Delzanno G “Orbital-motion-limited theory of dust charging and plasma response” 2014 *Phys. Plasmas* **21**, 123708 (Preprint arXiv:1503.07820v1)
- [124] Khrapak S A, Nefedov A P, Petrov O F and Vaulina O S “Dynamical properties of random charge fluctuations in a dusty plasma with different charging mechanisms” 1999 *Phys. Rev. E - Stat. Physics, Plasmas, Fluids, Relat. Interdiscip. Top.* **59**, 6017–6022
- [125] Bouchoule A *Dusty Plasmas: Physics, Chemistry and Technological Impacts in Plasma Processing* 1999 (John Wiley & Sons Inc. New York) ISBN 9780471973867

- [126] Denysenko I, Stefanović I, Sikimić B, Winter J, Azarenkov N A and Sadeghi N “A global model for the afterglow of pure argon and of argon with negatively charged dust particles” 2011 *J. Phys. D. Appl. Phys.* **44**, 205204
- [127] Luikov A *Analytical heat diffusion theory* 2nd ed 1968 (Academic press, inc. New York) ISBN 9780124597563
- [128] Makabe T and Petrovic Z L *Plasma electronics: Applications in Microelectronic Device Fabrication* 2nd ed 2015 (CRC press, Taylor & Francis group) ISBN 9781138034150
- [129] Itikawa Y “Cross sections for electron collisions with oxygen molecules” 2009 *J. Phys. Chem. Ref. Data* **38**, 1–20
- [130] Haxton D J, McCurdy C W and Rescigno T N “Dissociative electron attachment to the H₂ O molecule I. Complex-valued potential-energy surfaces for the B1₂, A1₂, and B2₂ metastable states of the water anion” 2007 *Phys. Rev. A - At. Mol. Opt. Phys.* **75**, 012710 (*Preprint* 0710.0008)
- [131] Branscomb L M “The Electron Affinity of Atomic Oxygen” 1958 *Nat. Phys.* **182**, 248–249
- [132] Harrison A H *Chemical Ionization Mass Spectrometry* 2nd ed 1992 (CRC press LCC) ISBN 0849342546
- [133] Van Minderhout B, Peijnenburg T, Blom P, Vogels J M, Kroesen G M and Beckers J “The charge of micro-particles in a low pressure spatial plasma afterglow” 2019 *J. Phys. D. Appl. Phys.* **52**, 32LT03
- [134] Wörner L, Ivlev A V, Couëdel L, Huber P, Schwabe M, Hagl T, Mikikian M, Boufendi L, Skvortsov A, Lipaev A M *et al.* “The effect of a direct current field on the microparticle charge in the plasma afterglow” 2013 *Phys. Plasmas* **20**, 10–17
- [135] Land V and Goedheer W J “Manipulating Dust Charge Using Ultraviolet Light in a Complex Plasma” 2007 *IEEE Trans. plasma Sci.* **35**, 280–285
- [136] Bagheri B, Teunissen J, Ebert U, Becker M M, Chen S, Ducasse O, Eichwald O, Loffhagen D, Luque A, Mihailova D *et al.* “Comparison of six simulation codes for positive streamers in air” 2018 *Plasma Sources Sci. Technol.* **27**, 15–18
- [137] Hoppel W A “Ion-aerosol attachment coefficients, ion depletion, and the charge distribution on aerosols” 1985 *J. Geophys. Res.* **90**, 5917–5923
- [138] Romay F J and Pui D Y “Free electron charging of ultrafine aerosol particles” 1992 *J. Aerosol Sci.* **23**, 679–692
- [139] Stefanović I, Berndt J, Marić D, Šamara V, Radmilović-Radjenović M, Petrović Z L, Kovačević E and Winter J “Secondary electron emission of carbonaceous dust particles” 2006 *Phys. Rev. E - Stat. Nonlinear, Soft Matter Phys.* **74**, 1–11

-
- [140] Boufendi L, Jouanny M C, Kovacevic E, Berndt J and Mikikian M “Dusty plasma for nanotechnology” 2011 *J. Phys. D. Appl. Phys.* **44**, 174035
- [141] Lee V, Waitukaitis S R, Miskin M Z and Jaeger H M “Direct observation of particle interactions and clustering in charged granular streams” 2015 *Nat. Phys.* **11**, 733–737
- [142] Bennet E D, Mahony C M, Potts H E, Everest P, Rutherford D, Askari S, McDowell D A, Mariotti D, Kelsey C, Perez-Martin F *et al.* “Precision charging of microparticles in plasma via the Rayleigh instability for evaporating charged liquid droplets” 2016 *J. Aerosol Sci.* **100**, 53–60
- [143] Thoma M H, Fink M A, Höfner H H, Kretschmer M, Khrapak S A, Ratynskaia S V, Yaroshenko V V, Morfill G E, Petrov O F, Usachev A D *et al.* “PK-4: Complex plasmas in space - The next generation” 2007 *IEEE Trans. Plasma Sci.* **35**, 255–259
- [144] Antonova T, Khrapak S A, Pustylnik M Y, Rubin-Zuzic M, Thomas H M, Lipaev A M, Usachev A D, Molotkov V I and Thoma M H “Particle charge in PK-4 dc discharge from ground-based and microgravity experiments” 2019 *Phys. Plasmas* **26**, 113703 (*Preprint* 1911.05591)
- [145] Kennedy R V and Allen J E “The floating potential of spherical probes and dust grains . II : Orbital motion theory” 2003 *J. Plasma Phys.* **69**, 485–506
- [146] Sikimić B, Stefanović I, Denysenko I B, Winter J and Sadeghi N “Dynamics of pulsed reactive RF discharges in response to thin film deposition” 2014 *Plasma Sources Sci. Technol.* **23**, 025010
- [147] Sikimić B, Stefanović I, Denysenko I B and Winter J “A non-invasive technique to determine ion fluxes and ion densities in reactive and non-reactive pulsed plasmas” 2013 *Plasma Sources Sci. Technol.* **22**, 045009
- [148] Bacharis M, Coppins M and Allen J E “Dust grain charging in RF discharges” 2010 *Plasma Sources Sci. Technol.* **19**, 025002
- [149] Godyak V A, Piejak R B and Alexandrovich B M “Electron energy distribution function measurements and plasma parameters in inductively coupled argon plasma” 2002 *Plasma Sources Sci. Technol.* **11**, 525–543
- [150] Samarian A A and Vladimirov S V “Charge of a macroscopic particle in a plasma sheath” 2003 *Phys. Rev. E - Stat. Physics, Plasmas, Fluids, Relat. Interdiscip. Top.* **67**, 5
- [151] Poirier J S, Bérubé P M, Margot J, Chaker M and Stafford L “Neutral gas temperature measurements in inductively coupled argon plasmas” 2009 *29th ICPIG* pp 10–13
- [152] Aston G and Wilbur P J “Ion extraction from a plasma” 1981 *J. Appl. Phys.* **52**, 2614–2626

- [153] Loeb H W “Plasma-based ion beam sources” 2005 *Plasma Phys. Control. Fusion* **47**, B565
- [154] Gerber R A and Gerardo J B “Ambipolar-to-free diffusion: The temporal behavior of the electrons and ions” 1973 *Phys. Rev. A* **7**, 781–790
- [155] Platier B, Limpens R, Lassise A C, Staps T J, Van Nindhuijs M A, Daamen K A, Luiten O J, Ijzerman W L and Beckers J “Transition from ambipolar to free diffusion in an EUV-induced argon plasma” 2020 *Appl. Phys. Lett.* **116**, 103703
- [156] Ibarra I, Rodríguez-Maroto J and Alonso M “Bipolar charging and neutralization of particles below 10 nm, the conditions to reach the stationary charge distribution, and the effect of a non-stationary charge distribution on particle sizing” 2020 *J. Aerosol Sci.* **140**, 105479
- [157] Adachi M, Pui D Y H and Liu B Y H “Aerosol Charge Neutralization by a Corona Ionizer” 1993 *Aerosol Sci. Technol.* **18**, 48–58
- [158] Liu B Y H, Pui D Y H and Lin B Y “Aerosol Charge Neutralization by a Radioactive Alpha Source” 1986 *Part. Part. Syst. Charact.* **3**, 111–116
- [159] Leppä J, Mui W, Grantz A M and Flagan R C “Charge distribution uncertainty in differential mobility analysis of aerosols” 2017 *Aerosol Sci. Technol.* **51**, 1168–1189
- [160] Johnson T J, Nishida R T, Irwin M, Symonds J P, Olfert J S and Boies A M “Measuring the bipolar charge distribution of nanoparticles: Review of methodologies and development using the Aerodynamic Aerosol Classifier” 2020 *J. Aerosol Sci.* **143**, 105526
- [161] Li L, Chahl H S and Gopalakrishnan R “Comparison of the predictions of Langevin Dynamics-based diffusion charging collision kernel models with canonical experiments” 2020 *J. Aerosol Sci.* **140**
- [162] Li L and Gopalakrishnan R “An experimentally validated model of diffusion charging of arbitrary shaped aerosol particles” 2021 *J. Aerosol Sci.* **151**, 105678
- [163] van Minderhout B, van Huijstee J C A, Platier B, Peijnenburg T, Blom P, Kroesen G M W and Beckers J “Charge control of micro-particles in a shielded plasma afterglow” 2020 *Plasma Sources Sci. Technol.* **29**, 065005
- [164] Tsyтович V N “Dust plasma crystals, drops, and clouds” 1997 *Physics-Uspekhi* **40**, 53–94
- [165] Gerber R A, Gusinow M A and Gerardo J B “Transition from Ambipolar to Free Diffusion of Ions” 1971 *Phys. Rev. A* **3**, 1703–1707
- [166] Gusinow M A and Gerber R A “Space-Charge-Controlled Diffusion in an Afterglow” 1972 *Phys. Rev. A* **5**, 1802–1806

-
- [167] Chen X, Seto T, Kortshagen U R and Hogan C J “Determination of nanoparticle collision cross section distribution functions in low pressure plasma synthesis reactors via ion mobility spectrometry” 2019 *Nano Futur.* **3**, 015002
- [168] Chen X, Seto T, Kortshagen U R and Hogan C J “Size and structural characterization of Si nanocrystal aggregates from a low pressure nonthermal plasma reactor” 2020 *Powder Technol.* **373**, 164–173
- [169] Goree J “Ion trapping by a charged dust grain in a plasma” 1992 *Phys. Rev. Lett.* **69**, 277–280
- [170] Mitchell E W J M and Wesley J “The work functions of copper, silver and aluminium” 1951 *Proc. R. Soc. London. Ser. A. Math. Phys. Sci.* **210**, 70–84
- [171] Sansonetti J E and Martin W C “Handbook of Basic Atomic Spectroscopic Data” 2005 *J. Phys. Chem. Ref. Data* **34**, 1559–2259
- [172] Shimanouchi T 2020 “Molecular Vibrational Frequencies” *NIST Chem. WebBook, NIST Stand. Ref. Database Number 69* ed Mallard E P L and WG (National Institute of Standards and Technology, Gaithersburg MD, 20899)
- [173] Surplice N A and D’Arcy R J “Reduction in the work function of stainless steel by electric fields” 1972 *J. Phys. F Met. Phys.* **2**, 8–11
- [174] Huang F, Peng R D, Liu Y H, Chen Z Y, Ye M F and Wang L “Fractal dust grains in plasma” 2012 *Phys. Plasmas* **19**, 093708
- [175] Ivlev A V, Khrapak A G, Khrapak S A, Annaratone B M, Morfill G and Yoshino K “Rodlike particles in gas discharge plasmas: Theoretical model” 2003 *Phys. Rev. E - Stat. Physics, Plasmas, Fluids, Relat. Interdiscip. Top.* **68**, 10
- [176] Banu N and Ticoş C M “Precession of cylindrical dust particles in the plasma sheath” 2015 *Phys. Plasmas* **22**
- [177] Molotkov V I, Nefedov A P, Pustyl’nik M Y, Torchinsky V M, Fortov V E, Khrapak A G and Yoshino K “Liquid plasma crystal: Coulomb crystallization of cylindrical macroscopic grains in a gas-discharge plasma” 2000 *JETP Lett.* **71**, 102–105
- [178] Annaratone B M, Khrapak A G, Ivlev A V, Söllner G, Bryant P, Sütterlin R, Konopka U, Yoshino K, Zuzic M, Thomas H M *et al.* “Levitation of cylindrical particles in the sheath of an rf plasma” 2001 *Phys. Rev. E - Stat. Nonlinear, Soft Matter Phys.* **63**, 364061–364066
- [179] Maiorov S A “Charging of a rodlike grain in a plasma flow” 2004 *Plasma Phys. Reports* **30**, 766–771
- [180] Miloch W J, Vladimirov S V, Pécseli H L and Trulsen J “Numerical simulations of potential distribution for elongated insulating dust being charged by drifting plasmas” 2008 *Phys. Rev. E - Stat. Nonlinear, Soft Matter Phys.* **78**, 1–7

- [181] Miloch W J, Vladimirov S V, Pécseli H L and Trulsen J “Interaction of two elongated dust grains in flowing plasmas studied by numerical simulations” 2009 *Phys. Plasmas* **16**, 023703
- [182] Holgate J T and Coppins M “Charging of nonspherical macroparticles in a plasma” 2016 *Phys. Rev. E* **93**, 1–5
- [183] Zahed H, Mahmoodi J and Sobhanian S “Analytical study of spheroidal dust grains in plasma” 2006 *Phys. Plasmas* **13**, 053505
- [184] Yousefi R, Davis A B, Carmona-Reyes J, Matthews L S and Hyde T W “Measurement of net electric charge and dipole moment of dust aggregates in a complex plasma” 2014 *Phys. Rev. E* **90**, 033101 (*Preprint* 1406.3114)
- [185] Jander H and Wagner H G “Formation of flame ions, clusters, nanotubes, and soot in hydrocarbon flames” 2006 *Combust. Explos. Shock Waves* **42**, 696–701
- [186] Sorokin A and Arnold F “Electrically charged small soot particles in the exhaust of an aircraft gas-turbine engine combustor: Comparison of model and experiment” 2004 *Atmos. Environ.* **38**, 2611–2618
- [187] Bartneck M, Keul H A, Gabriele Z K and Groll J “Phagocytosis independent extracellular nanoparticle clearance by human immune cells” 2010 *Nano Lett.* **10**, 59–64
- [188] Fish M B, Thompson A J, Fromen C A and Eniola-Adefeso O “Emergence and Utility of Nonspherical Particles in Biomedicine” 2015 *Ind. Eng. Chem. Res.* **54**, 4043–4059
- [189] Chen J, Clay N, Kong H and Korea S “Non-Spherical Particles for Targeted Drug Delivery Jinrong” 2016 *Chem Eng Sci* **125**, 20–24
- [190] Matthews L S, Shotorban B and Hyde T W “Discrete stochastic charging of aggregate grains” 2018 *Phys. Rev. E* **97**, 1–11
- [191] Asnaz O H, Jung H, Greiner F and Piel A “Charging of an irregularly shaped particle in the sheath of an rf plasma” 2018 *Phys. Plasmas* **25**, 073702
- [192] Sukhinin G, Fedoseev A and Salnikov M “The influence of dust particle geometry on its charge and plasma potential” 2019 *Contrib. to Plasma Phys.* **59**, e201800153
- [193] Fortin E and Weichman F L “Photoconductivity in Ag₂O” 1964 *Phys. status solidi* **5**, 515–519
- [194] Cheng Y S, Allen M D, Gallegos D P, Yeh H C and Peterson K “Drag force and slip correction of aggregate aerosols” 1988 *Aerosol Sci. Technol.* **8**, 199–214
- [195] Kousaka Y, Endo Y, Ichitsubo H and Alonso M “Orientation-specific dynamic shape factors for doublets and triplets of spheres in the transition regime” 1996 *Aerosol Sci. Technol.* **24**, 36–44

-
- [196] Cheng Y S, Chen B T, Yeh H C, Marshall I A, Mitchell J P and Griffiths W D “Behavior of compact nonspherical particles in the tsi aerodynamic particle sizer model APS33B: Ultra-stokesian drag forces” 1993 *Aerosol Sci. Technol.* **19**, 255–267
- [197] Allen M D and Raabe O G “Slip correction measurements for aerosol particles of doublet and triangular triplet aggregates of spheres” 1985 *J. Aerosol Sci.* **16**, 57–67
- [198] Horvath H “The Sedimentation Behavior of Non-Spherical Particles” 1974 *Staub Reinhaltung Reinhaltung der Luft (in English)* **34**, 197–202
- [199] Wörner L, Ivlev A V, Couëdel L, Huber P, Schwabe M, Hagl T, Mikikian M, Boufendi L, Skvortsov A, Lipaev A M *et al.* “The effect of a direct current field on the microparticle charge in the plasma afterglow” 2013 *Phys. Plasmas* **20**, 123702
- [200] Sharma G, Abuyazid N, Dhawan S, Kshirsagar S, Sankaran R M and Biswas P “Characterization of particle charging in low-temperature, atmospheric-pressure, flow-through plasmas” 2020 *J. Phys. D. Appl. Phys.* **53**, 245204
- [201] Dhawan S, Vidwans A, Sharma G, Abuyazid N H, Mohan Sankaran R and Biswas P “Enhancing charging and capture efficiency of aerosol nanoparticles using an atmospheric-pressure, flow-through RF plasma with a downstream DC bias” 2020 *Aerosol Sci. Technol.* **54**, 1249–1254
- [202] Delzanno G L, Lapenta G and Rosenberg M “Attractive Potential around a Thermionically Emitting Microparticle” 2004 *Phys. Rev. Lett.* **92**, 4
- [203] Latham R 1995 “Diagnostic Studies of Prebreakdown Electron “Pin-Holes”” *High Volt. Vac. Insul.* (Elsevier) pp 61–113
- [204] Gonzalez L A, Angelucci M, Larciprete R and Cimino R “The secondary electron yield of noble metal surfaces” 2017 *AIP Adv.* **7**, 1–7
- [205] Lekner J “Capacitance coefficients of two spheres” 2011 *J. Electrostat.* **69**, 11–14
- [206] Trinh N “Electrode Design for Testing in Uniform Field Gaps” 1980 *IEEE Trans. Power Appar. Syst.* **PAS-99**, 1235–1242
- [207] Zelenyuk A, Cai Y and Imre D “From Agglomerates of Spheres to Irregularly Shaped Particles: Determination of Dynamic Shape Factors from Measurements of Mobility and Vacuum Aerodynamic Diameters” 2006 *Aerosol Sci. Technol.* **40**, 197–217
- [208] Storch J A 2004 “Aerodynamic Disturbances on Rapidly Rotating Spacecraft in Free-Molecular Flow” *Eng. Constr. Oper. Challenging Environ.* vol 2003 (Reston, VA: American Society of Civil Engineers) pp 429–436 ISBN 9780784407226

List of publications

Peer-reviewed journal articles

- **The charge of micro-particles in a low pressure spatial plasma afterglow**
B. van Minderhout, A.T.A. Peijnenburg, P. Blom, J.M. Vogels, G.M.W. Kroesen and J. Beckers
Journal of Physics D: Applied Physics **52** 32LT03 (2019)
doi: <https://doi.org/10.1088/1361-6463/ab2525>
- **Charge control of micro-particles in a shielded plasma afterglow**
B. van Minderhout, J.C.A. van Huijstee, B. Platier, A.T.A. Peijnenburg, P. Blom, G.M.W. Kroesen and J. Beckers
Plasma Sources Science and Technology **29** 065005 (2020)
doi: <https://doi.org/10.1088/1361-6595/ab8e4f>
- **Charge neutralisation of microparticles by pulsing a low-pressure shielded spatial plasma afterglow**
B. van Minderhout, J.C.A. van Huijstee, A.T.A. Peijnenburg, P. Blom, G.M.W. Kroesen and J. Beckers
Accepted for publication in: *Plasma Sources Science and Technology* (2021)
doi: <https://doi.org/10.1088/1361-6595/abd81f>

In revision

- **Charge of clustered microparticles measured in spatial plasma afterglows follows the smallest enclosing sphere model**
B. van Minderhout, J.C.A. van Huijstee, R.M.H. Rompelberg, A. Post, A.T.A. Peijnenburg, P. Blom and J. Beckers
Journal: *Nature Communications*

Conference proceedings

- **Particle contamination control by application of plasma**
J. Beckers, B. van Minderhout, P. Blom, G.M.W. Kroesen and A.T.A. Peijnenburg
Proceedings SPIE 11323 **113232L** (2020)
doi: <https://doi.org/10.1117/12.2560192>

Conference contributions

Oral presentations

- *Charge control of airborne micro-particles in a shielded afterglow* 22nd Workshop on the Exploration of Low Temperature Plasma Physics, Kerkrade, The Netherlands (2019)
- *Charge control of micro-particles in a shielded afterglow* 72nd Gaseous Electronics Conference, College Station, Texas, United States of America (2019)
- *Plasma assisted contamination control for ultra-clean vacuum systems* Research Meet High Tech System Center, Eindhoven, the Netherlands (2018)
- *Charging and shielding dynamics of particles in plasma afterglow* 8th International Conference on the Physics of Dusty Plasmas, Prague, Czech Republic (2017)

Poster presentations

- *Particle contamination control by application of plasma* SPIE Advanced Lithography, San Jose, California, United States (2020)
- *Local charge measurements of micro-particles in a remote plasma afterglow* 31st Symposium on Plasma Physics and Radiation Technology, Lunteren, The Netherlands (2019)
- *Clustered micro-particles in remote plasma afterglow* 21st Workshop on the Exploration of Low Temperature Plasma Physics, Kerkrade, The Netherlands (2018)
- *Particles in plasma afterglow: charging and shielding* 30th Symposium on Plasma Physics and Radiation Technology, Lunteren, The Netherlands (2018)
- *Particles in plasma afterglow: charging and shielding* Physics@Veldhoven, Veldhoven, The Netherlands (2018)
- *(De)charging of particles advancing through spatial plasma* 20th Workshop on the Exploration of Low Temperature Plasma Physics, Kerkrade, The Netherlands (2017)
- *Plasma assisted contamination control for ultra-clean vacuum systems* International Advisory Board Meeting High Tech System Center, Eindhoven, The Netherlands (2017)

-
- *Charging and shielding of particles in plasma afterglow* 29th Symposium on Plasma Physics and Radiation Technology, Lunteren, The Netherlands (2017)
 - *Charging and shielding of particles in plasma afterglow: first results* 19th Workshop on the Exploration of Low Temperature Plasma Physics, Kerkrade, The Netherlands (2016)
 - *Plasma assisted particle contamination control* 28th Symposium on Plasma Physics and Radiation Technology, Lunteren, The Netherlands (2016)

Acknowledgements

Vier goede jaren promoveren zijn nu afgerond. Deze jaren waren succesvol, interessant en leuk door de hulp van de mensen die ik hier, in dit laatste hoofdstuk van mijn proefschrift, graag bedank.

Allereerst, een woordje voor **Job**, mijn promotor. Je hebt een gave om mensen te motiveren en te enthousiasmeren, wat me heeft geholpen om wetenschappelijke uitdagingen te relativeren. Ik heb met plezier met je samengewerkt, startend tijdens de externe stage en nu afsluitend met dit PhD project waarin ik veel geleerd heb van je. Dank ook voor het herhaaldelijke “compliment” over mijn computer bril, een mooie start van de vele online vergaderingen die we in het laatste jaar hebben gehad. Ook ben ik mijn tweede promotor **Gerrit** dankbaar. Het was leuk om te ervaren hoe veel plezier je haalde uit onze stevige wetenschappelijke discussies. Dit werkte zeer aanstekelijk. Gelukkig is mijn opstelling niet veranderd in een plasma-orgel, gezien je grote fascinatie voor dit instrument. De discussies die ik met **Paul** heb gevoerd, gaven me altijd een frisse en soms ietwat onorthodoxe blik op het onderzoek. Zo stelde je eens voor om te doen alsof ik een stofdeeltje was en het hele experiment te visualiseren. Deze kijk heeft me geholpen in de analyse van de experimenten. In dit lijstje van begeleiders mag **Ton** niet ontbreken. Ik kon altijd op je rekenen.

Vervolgens bedank ik graag de mensen die hebben bijgedragen aan de inhoud van deze thesis. **Judith**, bedankt voor de vele uren die we samen hebben besteed aan alle details van de opstelling en de analyse. Ik ben trots op onze fijne samenwerking. High five! Je was altijd scherp en gemotiveerd en nooit “frozen”. Zelfs niet als er grote zwarte spinnen in ons donkere lab zaten. **Bart**, we hebben samen in korte tijd mooie metingen gedaan, waarvoor dank. En dan **Robert**, dankzij jouw metingen in het lab hebben we een onderzoekslijn kunnen afronden die ik in het eerste jaar van mijn promotie ben gestart met **Antoine**, die verkennende metingen uitvoerde. Ik dank jullie van harte voor de inzet en het plezier dat we in het lab en daarbuiten hebben gehad. Verder ben ik trots op de projecten die **Thijmen**, **Robert van Gestel** en **Sam** hebben uitgevoerd. De samenwerking met alle genoemde personen waren een fantastisch aspect van mijn promotie.

I would like to thank my committee members **Lorin Matthews**, **Ageeth Bol**, **Holger Kersten** and **Ton Peijnenburg** for their time spent on reading this thesis and for serving on the doctorate committee.

During this project I have been part of the EPG research group, which has been a great pleasure, not only due to the working environment, but also to the many social activities with the staff, fellow PhD candidates and students. Highlights are the PSV match against Utrecht, bowling, curling, an escape room outing, many Borrels, barbecues, Christmas parties in June and so much more. **Anita**, thank you for your vital contribution in keeping EPG connected. These years have been a wonderful time, thank you all!

Ook een woord van dank voor de mensen bij VDL voor de samenwerking tijdens dit onderzoek. **Luuk**, **Dmitri**, **Kaspar** en **Johnny**, onze discussies (met de studenten) hebben dit onderzoek naar grotere hoogte getild. **Rick Baade**, ik kijk met plezier terug naar de periode waarin we samen een opstelling hebben ontworpen en gebouwd, gericht op de vertaling van onze onderzoeken naar toepassingen. We hebben samen veel dagen besteed aan uitzoeken en testen, en heel toevallig was dit vaak op een vrijdag zodat we daarna een biertje konden pakken. Later deelden ook **Rick Jongen** en **Ilian** mee in de gezelligheid toen zij dit project verder uitwerkten.

Mijn bijzondere dank gaat uit naar de technici voor hun waardevolle ondersteuning bij het uitvoeren van experimenten. **Eddie**, dankzij jouw onschatbare kennis en rustige manier van werken verliep het bouwen van mijn opstelling op rolletjes. Ondanks je vervroegd pensioen bleef je betrokken bij de groep en was je altijd bereikbaar om vragen te beantwoorden. **Ab**, heel veel dank voor de simpele oplossingen die ik zelf niet had bedacht, en voor de hulp bij de verhuizing van mijn opstelling. Het waren gezellige middagen in het lab, mede door je verrassende Twentse muzieksmaak. En dan **Pieter**, bedankt dat je altijd klaar stond om mee te helpen. Dankzij jouw elektro-technische expertise heb ik veilig en efficiënt kunnen werken in het lab. **Jürgen**, ook jouw bijdrage aan de verhuizing waardeer ik zeer. **Caspar**, ik ben dankbaar voor je enthousiaste bereidheid om mee te denken en voor alle onderdelen die ik heb mogen lenen. De gezellige koffiemomenten waren niet alleen motiverend, maar ook lekker door de zelf gemaakte bonbons die je meebracht. Ook denk ik met plezier terug aan de pizza avond. **Cristian** en **Janneke**, dank voor het meedenken bij de verhuizing. In dit lijstje van technici mag ook **Ad Holten** niet ontbreken. Je hebt me geholpen met het opzetten en ontwikkelen van de software voor deeltjestracking. **Beatriz**, dank voor je hulp bij de SEM metingen die hebben bijgedragen aan de interpretatie van dit onderzoek, en me hebben laten zien hoe fascinerend de wereld van hele kleine dingen kan zijn. Ook een woord van dank voor de mensen van het EPC (Equipment and Prototype Center). Speciaal bedank ik **Harrie**, **Dave**, **Gerrit**, **Joris**, **Bram**, **Paul Aendenrooier**, **Paul Beijer**, **Bart** en **Ad** voor hun hulp bij de realisatie en verbeteringen aan de meetopstellingen. **Ginny** en **Henk**, deze dank geldt zeker ook voor jullie. Ook wil ik mijn dank uitspreken aan **Roeland de Smet** omdat hij samen met zijn collega's midden in de zomervakantie binnen enkele dagen een nieuwe glazen buis heeft gebouwd.

Furthermore, I would like to thank **all fellow PhD candidates and post-docs**. You made the breaks and Borrels a lot of fun! There are some people I want to thank personally. First of all my officemates **Shahriar, Zahra, Dmitri, Saman, Tim, Marlous** and **Patrick**, it was marvellous to share an office with you. We had plenty of good conversations, lunch walks around the lake, and occasionally went for a game of table tennis, especially when **Yuan** was visiting us. I enjoyed our dinner nights very much, where each of us prepared a traditional dish, and **Samaneh** also joined us. I will miss our cozy office.

Een welkome onderbreking van de onderzoeksdagen waren de potjes squash samen met **Karsten, Bart Macco, Siebe, Tijn, Patrick, Marlous, Cristian** en **Caspar**. In een klein uur wisten we elkaar fanatiek uit te dagen wat mij de energie gaf om weer verder te werken. Ook dank ik **Luuk, Leroy, Ferdi, Peter, Tijn** en **Jesper** voor de vurige lunch discussies, de fijne gesprekken en de biertjes op de Borrel. **Tijn**, jou wil ik speciaal bedanken voor het fotograferen van de meetopstelling. Het resultaat is te zien op de omslag van de thesis. Graag bedank ik **Tim Donders** en **Thijs** voor de gezellige koffiegesprekken. **Siebe**, bedankt voor onze enthousiaste gesprekken over natuurkunde en alles daarbuiten. Ik zal de legendarische barbecue in het hart van de stad niet snel vergeten. **Tim Staps**, ik heb met veel plezier samen met je gebrainstormd en gespard over mooie vraagstukken: zowel binnen als de buiten de natuurkunde. Je lijkt onvermoeibaar en hebt altijd oog voor de juiste schoenkeuze. **Marlous**, je zorgde voor een frisse wind op kantoor als je terug kwam uit Parijs. Ik vond het fijn om samen te kletsen en te overleggen en heb genoten van je lekkere taarten. En dan **Patrick**, ik ben je niet alleen dankbaar voor de wetenschappelijke en technische adviezen, maar ook voor de goede gesprekken die we hebben gehad tijdens wandelingen, conferenties of gewoon op kantoor. Ook kijk ik met plezier terug op de avonden bij de scouting rond het kampvuur samen met **Tim Staps** en **Marlous**.

Mijn oprechte dank gaat uit naar **Johan** voor het redigeren van dit proefschrift en naar **Kim** voor het ontwerpen van de omslag van mijn proefschrift. Je mag trots zijn op je eerste ontwerp!

Graag bedank ik **Steven, Martijn, Cally, Anke, Mike, Jeanine, Machiel, Marloes, Berit, Victor, Marit, Marvin** en **Linda** voor het aanhoren van te uitgebreide technische verhalen, en voor de gezellige ontmoetingen die me nieuwe energie gaven. **Steven**, bedankt voor je ondersteuning in de laatste maanden van het schrijven door het beantwoorden van kleine en grote vragen of door een motiverend gesprek.

Hier, tegen het einde van dit dankwoord, wil ik mijn lieve schoonfamilie bedanken voor de interesse en steun. **Otto, Roman, Edith, Michael, Opa** und **Oma**, ich bin sehr dankbar, dass ihr meine Schwiegerfamilie seid.

En natuurlijk wil ik ook mijn familie bedanken. Alle ooms en tantes, neven en nichten, dank jullie wel voor de lieve kaarten en berichten om me succes te wensen in de laatste maanden van het schrijven. **Ma, Pa** en **Claudia**, heel veel dank voor jullie onvoorwaardelijke steun en interesse. Ik ben zo blij met jullie als ouders.

Last but not least wil ik **Anna** bedanken, mijn lieve vriendin. Heel vaak tijdens het avondeten ging het over dit promotieonderzoek. Iedere keer weer luisterde je en dacht je mee. Lieve **Anna**, dank je wel voor alle ondersteuning en je hulp.

Het zijn vier mooie jaren geweest samen met jullie allemaal. Jihoe!

Curriculum vitae

Boy van Minderhout

Born on the 23rd of September 1992 in Roosendaal, the Netherlands

2005-2011

Pre-university education (Gymnasium), Norbertus College Roosendaal

- Awarded CERN visit by the Utrecht University for Chaos Theory project

2011-2014

Bachelor's degree in physics at the TU/e

- Erasmus semester Uppsala university, Sweden. Specialisation in energy physics and sustainable development
- Internship at the TU/e Fusion research group: radiation produced by a Farnsworth–Hirsch fusor

2014-2016

Master's degree in physics at the TU/e

- Specialisation in plasma physics and radiation technology
- Research internship ASML: Flow enhanced decay of EUV-induced plasma
- Research graduation project VDL ETG: Plasma-assisted particle contamination control

2016-present

PhD candidate in the research group Elementary Processes in Gas discharges at the TU/e

- Best propaedeutic practical supervisor 2017-2018
- Member of the PhD council 2017-2019
- Collaboration with VDL ETG

*Joy in looking and
comprehending is nature's
most beautiful gift.*

Albert Einstein